Flight Dynamics and Control of Highly Flexible Flying-Wings

Brijesh Raghavan

Dissertation submitted to the Faculty of the
Virginia Polytechnic Institute and State University
in partial fulfillment of the requirements for the degree of

Doctor of Philosophy
in
Aerospace Engineering

Mayuresh J. Patil, Chair
Craig A. Woolsey
Rakesh K. Kapania
Leigh S. McCue

March 30, 2009
Blacksburg, Virginia

Keywords: Flexible high aspect-ratio flying-wings, flight dynamics, flight control

Flight Dynamics and Control of Highly Flexible Flying-Wings

Brijesh Raghavan

(ABSTRACT)

High aspect-ratio flying wing configurations designed for high altitude, long endurance missions are characterized by high flexibility, leading to significant static aeroelastic deformation in flight, and coupling between aeroelasticity and flight dynamics. As a result of this coupling, an integrated model of the aeroelasticity and flight dynamics has to be used to accurately model the dynamics of the flexible flying wing. Such an integrated model of the flight dynamics and the aeroelasticity developed by Patil and Hodges is reviewed in this dissertation and is used for studying the unique flight dynamics of high aspect-ratio flexible flying wings. It was found that a rigid body configuration that accounted for the static aeroelastic deformation at trim captured the predominant flight dynamic characteristics shown by the flexible flying wing. Moreover, this rigid body configuration was found to predict the onset of dynamic instability in the flight dynamics seen in the integrated model. Using the concept of the mean axis, a six degree-of-freedom reduced order model of the flight dynamics is constructed that minimizes the coupling between rigid body modes and structural dynamics while accounting for the nonlinear static aeroelastic deformation of the flying wing. Multi-step nonlinear dynamic inversion applied to this reduced order model is coupled with a nonlinear guidance law to design a flight controller for path following. The controls computed by this flight controller are used as inputs to a time-marching simulation of the integrated model of aeroelasticity and flight dynamics. Simulation results presented in this dissertation show that the controller is able to successfully follow both straight line and curved ground paths while maintaining the desired altitude. The controller is also shown to be able to handle an abrupt change in payload mass while path-following. Finally, the equations of motion of the integrated model were non-dimensionalized to identify aeroelastic parameters for optimization and design of high aspect-ratio flying wings.

Dedicated

to

my mother and the memory of my father

Acknowledgments

I would like to thank my adviser, Prof. Mayuresh Patil, for all his help and guidance over the last four years. To say that this dissertation would not be possible without him is an understatement. He has encouraged me when I felt that my dissertation topic was too multi-disciplinary for me to solve, and has set high standards for us to meet. He has always kept an open door for his graduate students and has always found the time to explain things repeatedly till I was capable of understanding them. He has been very considerate during some very difficult personal situations that I have been through, and has let me take time off to take care of things back home.

I would like to thank Prof. Craig Woolsey, Prof. Rakesh Kapania and Prof. Leigh McCue for serving on my PhD committee. Their input and feedback over the last three years has been invaluable in helping me frame my problem statement, and in ensuring that the quality of my work meets the standards of a dissertation. I would like to thank Prof. Michael Philen for serving as the examiner for my defense in Prof. Kapania's absence. I would like to thank Prof. Christopher Shearer of AFIT for flying in all the way from Ohio for my defense. His PhD dissertation at the University of Michigan was the first one that addressed flight control of HALE airplanes, which made his feedback all the more valuable. I would also like to thank Prof. Woolsey and Chris Cotting for helping me understand the basics of nonlinear dynamic inversion.

Over the last three and a half years, I have probably spent more time in my office than I have in any other location in Blacksburg. This has taken its toll on the mental

well-being of my labmates and other people on the floor. Over the years, Rana, Jason, Will, Chris, Jeff, Johannes, Thomas, Avani, Pankaj, Karen, Wes and Sameer have helped me maintain my sanity in the face of seemingly unsurmountable MATLAB error codes. They have put up with my pathetic sense of humor, loud and obnoxious laughter and have helped me see the world from the perspective of different cultures (American and European). I leave Femoyer 209 with pleasant memories, and I leave them all with some of my bad habits to remember me by.

I met Lisa and Kenneth Granlund, Hamid Khameneh and Riley on my first hike to McAfee's Knob in the fall of 2005. Over the next two years, I spent many weekends with them hiking the hills around Blacksburg and talking about things outside of work. I would like to thank them for those wonderful trips, and I hope that they do visit me in India someday ! I would like to thank my roommates over the years and my friends in Blacksburg for some of the better days that I have spent here. One of my friends, Minal Panchal, was murdered in the shooting in Norris Hall on April 16^{th} 2007. In the brief time that I knew her, she has left me with memories full of laughter and for that I will always be grateful.

My stay here would not have been possible without my extended family back home. In particular, I owe much to my relatives Elema and Balappapan and our neighbours in Bombay, Daisy aunty and Joy uncle. They, along with other friends and family in Bombay, were the people who talked to my father's doctors and looked after him during his final years, all duties that were mine to bear. I would like to thank my friends, Girish, Shivangi, Gaurang, Kunal, Nag, Subbu, Praveena, Bharati, Payal, Girisha and Rana for helping me out through some very difficult days.

My father passed away on 4^{th} May 2006, less than nine months after I started graduate studies here, and a week before I was due to arrive in India to see him. My mother has been through exceptionally trying times over the last few years, but not once have I heard her complain about the situations that she has had to face. My success has been built on

their sacrifices. Both my father and my maternal grandfather had to drop out of school after 10^{th} grade due to adverse financial circumstances. In many ways, this PhD meant much more to them than it ever will for me. I hope that I have been able to give them some measure of happiness from my academic success.

Last but not the least, I would like to thank the Aerospace and Ocean Engineering Department for funding me for the first three years and for the Pratt Fellowship in 2009 and DARPA/Aero Institute for funding the final two semesters of my graduate studies.

Contents

List of Figures

List of Tables

Nomenclature

A	beam cross-sectional area
a	computed acceleration
b	wing span
$\mathcal{C}$	rotation matrix
$\mathcal{C}_a$	rotation matrix from aerodynamic frame to local beam frame
C_D	Coefficient of drag
C_L	Coefficient of lift
C_m	Coefficient of moment
c	local chord
dl	structural element length
E	Young's Modulus
$\mathbf{e}_1, \mathbf{e}_2, \mathbf{e}_3$	unit vector along x,y and z axis respectively
$\mathbf{F}$	internal force
$\mathbf{f}$	external force
G	Shear Modulus
$\mathbf{g}$	gravity vector
g_0	magnitude of gravity vector
$\mathbf{H}$	angular momentum
h	altitude
$\mathcal{I}$	moment of inertia
J	torsion constant

$\mathbf{k}$	initial curvature of wing
k_2,k_3	Shear correction factor
K	gain value
L	reference length
l	semi-span of wing
$\mathbf{M}$	internal moment
M	Mass
$\mathbf{m}$	external moment
N	total number of elements
$\mathbf{P}$	linear momentum
$\overline{q}$	dynamic pressure
$\mathcal{R}, \mathcal{S}, \mathcal{T}$	cross-sectional flexibility coefficient
r_i	turn rate in inertial frame
$\mathbf{r}$,$\mathbf{R}$	position vector
T	thrust value
$\mathbf{u}$	displacement of a point on the beam axis
$\mathbf{V}$	linear velocity
x, y, z	elements of position vector in inertial frame
$\mathbf{X}$	state-vector
γ	flight path angle
ψ, θ, ϕ	yaw, pitch and roll angles respectively
χ	yaw angle of velocity vector in inertial frame
$\mathbb{I}$	3×3 identity matrix
δ	control surface deflection
ϵ	stain of beam axis under loading
κ	curvature of beam axis under loading
μ	mass of element
ξ	center of mass offset

$\mathbf{\Omega}$	angular velocity
λ	inflow vector
λ_0	inflow coefficient
ρ	density of air
Subscript	
$aero$	aerodynamic in nature
B	local beam axis
c	value commanded by dynamic inversion
cg	center of gravity
g	gravitational in nature
i	inertial reference frame
l	lateral, value to the left of node
M	mean reference frame
mr	root to mean transformation
mi	inertial to mean transformation
T	propulsive in nature
R	root reference frame
ri	inertial to root transformation
r	value to the right of the node
∞	free-stream condition
Superscripts	
B	local beam axis in the deformed frame
b	local beam axis in the undeformed frame
d	demanded rate
n	n^{th} node/element
n_g	reference node for computing gravity vector components in beam axis
I	inertial reference frame
M	mean reference frame

R	root reference frame
$\hat{}$	nodal value
$\bar{}$	mean value over the beam element
$\tilde{}$	cross product matrix
$'$	derivative along beam X co-ordinate
$\dot{}$	derivative with respect to time

Chapter 1

Introduction

1.1 Motivation

High Altitude, Long Endurance (HALE) Unmanned Aerial Vehicles (UAVs) are designed to cruise above 60,000 ft and fly missions ranging from a few days to a few years [1]. This unique flight profile makes it possible to use these aircraft as platforms for scientific research, aerial photography and telecommunication relay. The demand for these capabilities in both the civilian and the military sectors has been the motivation for the development of HALE UAVs over the past two decades.

The Environmental Research Aircraft and Sensor Technology (ERAST) program was conducted by NASA from 1994 to 2003 with the primary objective of developing HALE UAVs [1]. As part of this program, Aerovironment developed a series of solar-powered flying wing configurations, whose aspect-ratio increased progressively from 12 to 30.9 along with a corresponding increase in payload capability. The final airplane in this series, Helios, encountered atmospheric turbulence and crashed during a flight test off the island of Kauai, Hawaii on 26th June 2003 [2]. The atmospheric turbulence encountered during the flight test caused the flying wing to deform to an unstable, high-dihedral configuration. This in turn led to divergent pitch oscillations during which the airplane exceeded its

design airspeed and led to the failure of its wing panels. The mishap investigation report concluded that the decision to test fly the crashed configuration was a flawed one, but it has been made because available analysis tools were unable to predict the sensitivity of the configuration to disturbances. The report further suggested the development of "*more advanced, multidisciplinary (structures, aeroelastic, aerodynamics, atmospheric, materials, propulsion, controls, etc) 'time-domain' analysis methods appropriate to highly flexible, 'morphing' vehicles*".

In 2007, DARPA initiated the Vulture program to develop technology for an aircraft capable of uninterrupted flight for atleast five years [3]. Two of the three concepts currently being studied involve high-aspect ratio wings [4, 5, 6].

1.2 Objectives

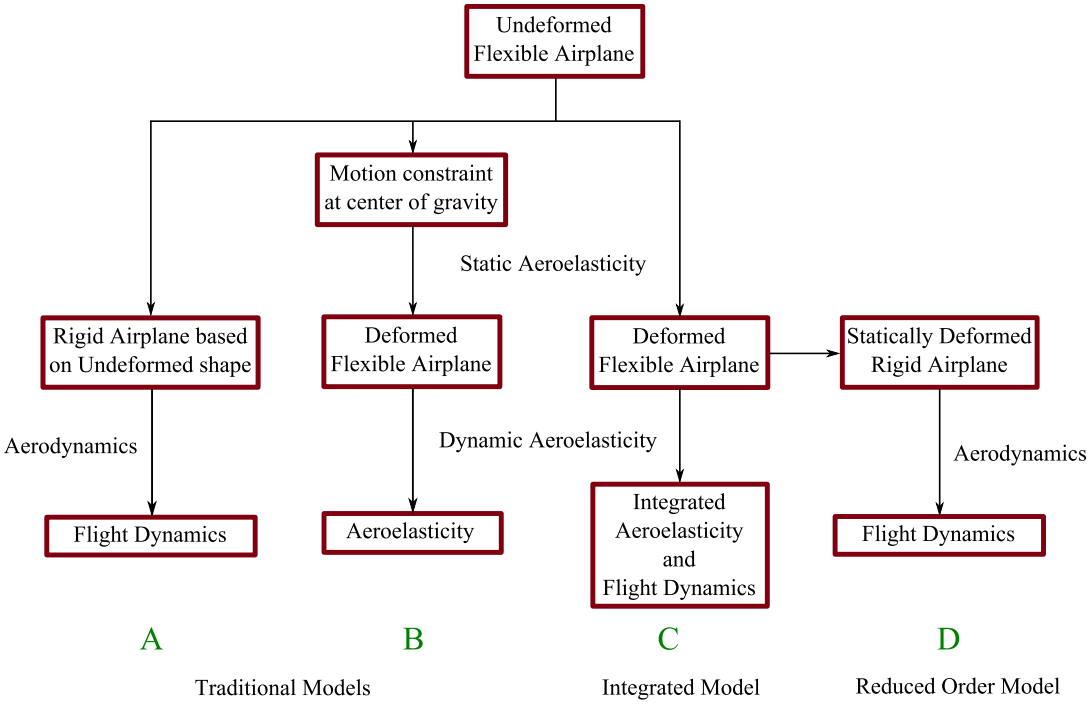

Figure 1.1: Methodology Followed

For conventional airplane configurations, the structural deformation under flight loads (i.e. the static aeroelastic deformation) is not significant enough to influence the flight dynamics and no significant interaction is observed between the rigid body modes and aeroelastic modes. Therefore, the modeling for flight dynamics and aeroelastic analysis for such configurations can be decoupled and can be carried out separately. Analysis of flight dynamics is carried out by assuming a perfectly rigid structure based on the undeformed shape as shown in sequence A in Fig. 1.1. These models are used as the basis for flight control design. Aeroelastic analysis, on the other hand, is carried out on a flexible model of the airplane structure with no rigid body degrees of freedom as shown in sequence B in Fig. 1.1.

However, a low weight, high aspect-ratio wing design exhibits high flexibility and undergoes significant deformation in flight. Moreover, the aeroelastic and flight dynamics frequencies overlap and the flight dynamics and aeroelastic modes are coupled. The influence of both static and dynamic aeroelastic effects on the flight dynamics becomes significant, and has to be accounted for in the flight dynamics model. The analysis of the flight dynamics and aeroelasticity has to be carried out in an integrated manner as shown in the sequence C in Fig. 1.1. Such an integrated model was developed by Patil and Hodges in 2003 [7] and has been reviewed in the third chapter of this dissertation.

Due to this coupling between aeroelasticity and flight dynamics, flight control design has to be carried out on an integrated model of the total dynamics of the system. However, a reduced order model can be used for flight control design if the coupling between aeroelasticity and flight dynamics is minimized. This is accomplished by writing the equations of motion in the mean axis system as shown in the fourth chapter. These equations in the mean axis system capture the rigid body modes and static aeroelastic deformation of the flying wing, and minimize the interaction between structural dynamics and the rigid body modes.

In order to analyse the accuracy of this reduced order model, this dissertation studies

the unique flight dynamics of a flexible, high aspect-ratio flying-wing, with an emphasis on the influence of static aeroelasticity on the flight dynamics. The dynamic characteristics of the fully flexible configuration are compared with those of an equivalent rigid-body model based on the deformed shape under static aeroelastic loading (henceforth referred to as the statically deformed configuration). The flight dynamics of the statically deformed configuration is analyzed as depicted in sequence D of Fig. 1.1. A modified criteria for the onset of static flight dynamic instability in the presence of static aeroelastic deformation is also presented.

The second objective is the design of a flight control system for path-following for a flexible, high aspect-ratio flying wing. This is accomplished by a combination of a nonlinear guidance law and a nonlinear dynamic inversion controller applied to a six degree-of-freedom reduced-order model of the dynamics written in the mean axis system as shown in the fourth chapter. The control inputs and the closed-loop response for the flexible flying wing for path-following for a straight-line ground path and for a curved ground path are presented. The controller is also shown to be able to handle an abrupt change in payload mass while path-following.

Finally, the dissertation identifies non-dimensional aeroelastic parameters that can be used for design and optimization of flexible, high aspect-ratio flying wings, and presents expressions for estimating the state variables required by the controller from measured flight data.

The work presented in this dissertation is *directly* applicable to unswept, high aspect-ratio, highly flexible flying wings whose structure can be accurately modeled using non-linear beam theory and whose aerodynamics is captured by two-dimensional, unsteady, incompressible, potential flow models. The applicability of the flight dynamic analysis and the flight control design presented here will have to be *reviewed* for a flying wing which does not satisfy any of the assumptions mentioned above.

Chapter 2

Literature Survey

The literature review is divided into four sections. The first two sections review literature on flight dynamics and controls of generic flexible configurations. The third section presents literature on the aeroelasticity of high aspect-ratio wings. The final section reviews research specific to the flight dynamics and control of flexible, high aspect-ratio configurations.

2.1 Flight Dynamics of Flexible Airplanes

In one of the earliest works on flight dynamics of flexible airplanes, Skoog studied the effect of aeroelasticity on the longitudinal static stability of airplanes [8]. Flexibility was found to change the spanwise aerodynamic loading distribution and shift the aerodynamic center forward, leading to a reduction in longitudinal static stability. This effect was found to be more pronounced at higher sweepback angles and aspect ratios. The lift-curve slope of the wing was also reduced, leading to an increase in the angle of attack required for trim. This in turn increased the stability contribution of a rigid horizontal tail, leading to an effective increase in static stability. A conventional airplane configuration with a

swept wing was analyzed and it was found that torsional deflections had a stabilizing effect while bending deflections had a destabilizing effect. However, the net effect of these two factors was dependent on the ratio of bending to torsional rigidities, location of elastic axis and the sweep angle. In a two part paper, Milne introduced the concept of the mean axis, which decouples the equations of motion for flight dynamics from the equations for structural dynamics for small deformations [9]. The paper developed the equations of motion for a flexible airplane, and studied the equilibrium and stability of the airplane for small perturbations. The concept of the mean axis, which is central to the control design presented in this dissertation, was further elaborated upon in another paper by the same author [10]. Wykes and Lawrence studied the effect of aerothermoelasticity on the longitudinal stability and control of a supersonic transport configuration with a canard and delta wings [11]. New stability derivatives were introduced to account for the effect of flexibility on the flight dynamics of the airplane. Fuselage flexibility was found to cause elevon reversal, and the coupling of the short period mode with the first symmetric fuselage bending mode was seen to result in a dynamic instability.

Rodden's analysis of experimental data showed that the the lateral stability derivative for rolling moment with respect to sideslip (C_{l_β}) changes significantly with a change in dihedral angle under high load factors [12]. An analytical correction factor for the stability derivative was introduced and a new method for predicting the correction in terms of structural and aerodynamic influence coefficients was presented. Swaim and co-workers modeled the longitudinal and lateral dynamics of elastic airplanes in a series of two papers [13, 14]. Aerodynamic forces and moments induced by elastic modes were modeled as functions of rigid-body stability derivatives, while neglecting flexibility corrections to rigid-body stability derivatives themselves. Most of the terms in the new state space model showed good agreement with experimental data for the B1 bomber. In a two-part series Weisshaar and Ashley studied the static aeroelasticity of flying wing configurations [15, 16]. Rigid body degrees of freedom were found to significantly alter the divergence speed as compared to those for a cantilevered wing. An unswept flying wing trimmed in

roll using elevons was found to exhibit antisymmetric torsional divergence due to control ineffectiveness [16]. The speed at which this instability occurs was found be dependent on aerodynamic and geometric parameters of the wing [15]. The unswept flying wing trimmed in level flight was found to exhibit symmetric divergence at twice the speed as a cantilevered wing.

In their derivation of the equations of motion of flexible airplanes, Rodden and Love modeled static aeroelastic deformation of the structure and numerically showed the error in predictions when the correct axis system in not used for modeling the dynamics of the airplane [17]. However, an error was found in the derivation of the equations of motion presented in this paper and it was corrected in a paper by Dykman and Rodden [18]. It was shown that the equations for dynamics of structural modes cannot be augmented to the equations for the dynamics of statically deformed airplane without adding a correction factor. This paper also compared the accuracy of a solution with truncated high frequency dynamic modes, a solution with some dynamic modes residualized and a solution with all dynamic modes residualized with the complete dynamic solution. The solution with all dynamic modes residualized was found to have good accuracy except when the airplane is subject to abrupt control inputs, as this excites the structural modes. The solution with dynamic modes truncated without residualization was found to have limited accuracy. In similar work, Karpel formulated a dynamic residual model for a flexible airplane that accounted for aerodynamic effects dependent on the velocity of the modes [19]. For the example considered in the paper, this formulation was found to substantially decrease the error as compared to a model that uses modal truncation. The increase in computation time was found to be reasonable considering the improvement in accuracy and the subsequent time savings obtained from reduced order models.

Waszak and Schmidt derived the equations of the motion for a flexible airplane in the mean axis system using Lagrange's equation and the principle of virtual work [20]. The derivation assumed small deformation, pre-computed modes of vibration, aerodynamic strip theory and a constant inertia matrix. The equations for flight dynamics and

structural dynamics were coupled through the dependence of generalized forces on the generalized displacement co-ordinates. Three configurations with varying degrees of flexibility were numerically analyzed in the paper. The results showed that a model where structural modes are residualized is more accurate as compared to a model where the structural modes are truncated. However, even the residualized model showed significant inaccuracies as compared to results from the full flexible model as the flexibility of the airplane increases. This modeling of equations of motion for a longitudinal airplane was later reviewed in a paper by Schmidt and Raney [21], where visual-motion simulator studies found that decreasing the lowest structural frequency has an adverse effect on the handling quality of the airplane. Aeroelastic coupling was found to degrade ride quality and vibrations felt at the cockpit influenced the precision of control inputs, resulting in involuntary control inputs. The latter effect, known as biodynamic feedback, was especially pronounced in the case of lateral vibrations of the airplane structure. Newman and Schmidt presented three numerical techniques for model reduction [22]. These methods were applied to the model for longitudinal dynamics of a flexible airplane developed in Ref. [20]. Of the three numerical reduction techniques presented, the frequency-weighted balanced technique was found to give superior results to both the residualization and truncation techniques. A method for obtaining literal approximations was also presented that captures the pole-zero structure and numerical values of the coefficients of the reduced-order models obtained using numerical model-reduction techniques. The procedure for obtaining literal approximations was automated, and literal approximations were presented for a subsonic flexible configuration, a supersonic missile and a hypersonic configuration in a paper by Livneh and Schmidt [23]. The set of unified literal approximations presented in the paper was found to be more accurate than approximations of longitudinal modes obtained by decoupling the rigid body and aeroelastic modes.

Siepenkotter and Alles studied the nonlinear stability characteristics of a flexible airplane configuration by defining eigenvalues and eigenvectors as functions of perturbation from the equilibrium point [24]. The integrated flexible aircraft model was based on

previous work [9, 20, 25], and three bending and one torsion mode were used to model wing flexibility. Linear stability analysis carried out at straight and level trim showed the spiral mode to be unstable. Nonlinear stability analysis presented in the paper detected the presence of a stable equilibrium corresponding to a non-zero roll angle, which was confirmed by an open-loop simulation. Drela modeled the dynamics of a flexible aircraft using nonlinear beams for the structure and an unsteady lifting line model with compressibility correction for the aerodynamics [26]. The trim point for the nonlinear system was computed using a Newton-Raphson solver, and time marching was carried out using a backward-difference formulation. The model was used to generate a root-locus plot for a sailplane with flight speed as the parameter. Winther *et al.* derived reduced order equations for a flexible airplane by eliminating the auxiliary state variables required to model unsteady aerodynamics [27]. The equations were transformed from the body axis to the mean axis and equations for structural dynamics were integrated with the quasi-steady nonlinear equations of motion.

Equations of motion for a flexible airplane configuration were rederived by Burtill *et al.* while retaining inertial coupling terms between angular motion and flexibility [25]. A scalar parameter introduced in the paper can be used to determine if the coupling is significant for the case considered. Reschke derived the nonlinear equations of motion for flexible aircraft with a special focus on the inertial coupling between maneuvering flight and structural dynamics of the airframe [28]. The force summation method, used for calculation of aerodynamic and inertial loads acting on the airplane for a given trajectory, was extended to account for inertial coupling. The residualized model approach used for integrating the aerodynamic models with the equations of motion was extended to work with the force summation method and quasi-flexible aerodynamic loads. The influence of inertia coupling was found to be significant for high angular-rate/acceleration maneuvers. Nguyen derived equations for the flight dynamics of a flexible airplane that accounts for aeroelastic, propulsive and inertial coupling [29]. The structural dynamics of the wing was modeled using an equivalent beam model and solved using finite element analysis to

obtain generalized co-ordinates corresponding to symmetric and anti-symmetric structural modes. These generalized co-ordinates were used to couple the flight dynamic equations with the structural dynamics of the wing though the force and moment expressions in the flight dynamic equations.

2.2 Flight Control of Flexible Airplanes

Freymann studied the change in aircraft dynamic behavior resulting from the presence of an active control system [30]. The paper presented examples of the four types of coupling arising from the interaction of the control system designed for a flexible or rigid body mode with another flexible or rigid body mode. In some cases, this coupling was found to result in a decrease in the flutter speed or an instability in a rigid bode mode. Kubica *et al.* introduced a new control synthesis technique for aircraft with significant coupling between flight mechanics and structural dynamics modes [31]. By combining optimal control and eigenstructure assignment through optimization, this technique can be used to stabilize flight dynamic and structural modes and increase parameter robustness. Becker *et al.* presented an integrated design of the flight control system and notch filters on the basis of a coupled flight dynamic and structural dynamic model [32]. The new design was found to reduce degradation in rigid body stability margins and improve elastic mode stability. Etten *et al.* presented an integrated flight and structural modal control design for a flexible aircraft using linear parameter varying methods, and compared it with another controller in which the flight control and structural modal control were designed sequentially [33]. The handling and ride qualities of the closed loop systems were compared using μ analysis. The integrated controller was found to be more robust to uncertainties in air density, and also gave higher aeroelastic damping with lower control input.

Miyazawa extended the multiple-delay-model and multiple-design-point approach to make it applicable to airplane configurations that show coupling of the control system

with the flexible structure [34]. A new criteria for structural-control coupling stability was introduced. Alazard designed a robust lateral controller for a flexible airplane configuration using H2 synthesis [35]. The control synthesis described in the paper is a multi-step process that involves sequential tuning of gains. The paper also looked at the robustness of the closed-loop system with respect to sensor location and selection. Goman *et al.* compared an integrated flight and aeroelastic controller designed using μ synthesis to a conventional controller designed using rigid body mode feedback and notch and lag filters [36]. The step-response of both controllers were found to be quite similar as the configuration presented in the paper does not exhibit coupling between the control system and the structure. However, the closed-loop system with the integrated controller exhibited more robustness than the one with the conventional controller. Silvestre and Paglione derived the equations for dynamics of a flexible airplane in the mean axis system using a modal superposition approach for the structural dynamics and a quasi-steady aerodynamic model [37]. A controller was designed for disturbance rejection using the H_∞ static output-feedback approach.

Over a series of three papers, Gregory addressed the problem of applying a dynamic inversion to control a large flexible aircraft [38, 39, 40]. The modified dynamic inversion controller presented in the first paper was designed to follow control inputs while minimizing elastic deflections at the front end of the fuselage. The controller was designed on a longitudinal model with eight elastic modes and applied on a longitudinal model with twenty elastic modes. The dependence of longitudinal and elastic modal states on actuator rates and accelerations was also modeled. These effects may not be insignificant for an elastic airplane due to unsteady aerodynamic and mass coupling effects. It was found that the stability augmentation system and structural modal system had to be designed in an integrated fashion, as the stand-alone stability augmentation system used for comparison drove the fuselage structural modes unstable and drove one of the control surfaces to its rate limit [38]. The next paper in the series dealt with the modification introduced in the dynamic inversion control law to make it applicable to the flexible

configuration [39]. It was shown that the time constant of a first-order filter introduced in the dynamic inversion loop changed the damping of a flexible mode in a stand-alone second-order flexible model. This influence of the first-order filter on the damping of the flexible mode was also found in the complete elastic model of the airplane. It was also found that individual dynamics can be controlled by changing the corresponding filter time constant while leaving the other filter time constants unchanged. The final paper in the series presented stability results for the dynamic inversion controller as applied to the flexible aircraft problem [40]. Results were presented for a simplified model. Only one flexible mode was modeled along with longitudinal dynamics, and the control law was designed only for flight control. The analysis considered only the dynamic inversion part of the controller and the part specifying the desired dynamics was not analyzed.

Meirovitch and Tuzcu derived a unified formulation for dynamics of a flexible aircraft using a Lagrangian approach [41]. The fuselage, wings and empennage structure were modeled as beams undergoing bending and torsion, and aerodynamics was modeled using two-dimensional strip theory. The equations were written in state-space form and separated into a zero-order form for aircraft maneuvering and a first-order form consisting of small perturbations in the rigid body states and elastic deformations. These perturbation equations were used for control design using both the LQR and LQG approach for straight and level flight and a steady, level turn. Stability was analyzed by computing eigenvalues of both the closed and open loop system and simulations were presented by numerically integrating the closed loop equations. Improved results were presented in a follow-up paper which replaced component shape functions used for structural modeling with global aircraft shape functions, and introduced new controller and observer designs [42]. These global aircraft shape functions, which were derived by solving the eigenvalue problem of a free-free aircraft at unstrained equilibrium in the absence of aerodynamic forces, allow the structural deformation to be modeled with fewer states. The third paper in the series studied the coupling between aeroelastic and flight dynamic modes for straight and level flight and for a steady level turn [43]. The restrained airplane configuration with no rigid

body modes of freedom was found to be asymptotically stable. However in both cases, an LQR controller that ensures closed-loop stability for the corresponding rigid body configuration was found to destabilize the flexible unrestrained airplane. This instability was attributed to the coupling between rigid body and flexible modes. The final paper presented simulation results for a flexible airplane that flies a time-varying pitch maneuver [44]. A new controller consisting of a combination of LQR and direct feedback controls method was introduced and the controls are computed in discrete time. Point actuators are used to suppress vibrations on the wind and empennage.

2.3 Aeroelasticity of High Aspect-Ratio Wings

Patil *et al.* studied the effects of geometric non-linearities arising from large deformation on the aeroelasticity of high aspect-ratio wings [45]. Dynamic aeroelastic characteristics were found to be significantly altered due to wing deformation and were found to be dependent on the relative values of the structural frequencies. The deflection of the wing under loading was found to result in a coupling between the bending and torsion modes. The increase in deflection was also found to result in a significant decrease in the flutter speed. The predominant cause of this decrease in flutter speed was shown to be steady-state wing curvature under loading, which was also found to decrease the effective lift generated by the wing in the vertical direction. It was found that this effect could be canceled out by pre-curving the wing to give an effectively straight wing under nominal flight loads. Similar results were obtained by Frulla who improved flutter characteristics by increasing the bending stiffness [46]. A follow-up paper by Patil and Hodges looked at the effects of aerodynamic and structural non-linearities on aeroelastic behavior [47]. Aerodynamics was modeled using a non-planar fixed wake vortex lattice method for the quasi-steady part and a doublet-lattice method for the unsteady part. The effect of the nonplanarity on both steady and unsteady loads calculation was found to be negligible, and three dimensional effects were found to be significant only at the

wing tip. However, the nonplanar shape of the wing was found to have a significant effect on the local angle of attack at any wing section and the component of the airloads in the vertical direction. Static structural deflection was captured accurately by linear structural models, though the effect of the deflection on the dynamics was not modeled accurately by linear models. A model that accounts for the steady state structural deformation and uses a two-dimensional unsteady loads model, as opposed to a nonplanar three-dimensional model, was found to accurately predict the aeroelastic behavior of the high aspect-ratio wing.

Patil *et al.* developed a model for studying nonlinear aeroelasticity and Limit Cycle Oscillations (LCOs) and applied it to the Goland wing [48]. The wing structure was modeled using a geometrically exact nonlinear beam theory, and the aerodynamics was modeled using an unsteady state space model augmented for compressibility and dynamic stall effects. Flutter speed was found to increase due to geometric stiffening effects and decrease due to coupling between low frequency stall dynamics and structural dynamics. LCOs were generated due to stall and geometric stiffening effects above speeds where linearized stability analysis predicted instabilities, and for finite perturbations from stable equilibrium points. Similar investigations on LCOs were carried out on a high-aspect ratio configuration [49]. The dependence of post-flutter LCOs on tip displacement and pre-flutter LCOs on large perturbations were investigated. The first torsion and edge-wise bending mode were found to couple with increasing flat-wise bending deformation. The characteristics of LCOs were seen to be dependent on speed and not dependent on tip-displacement. Results obtained by Tang and Dowell showed a similar dependence of flutter speed and nonlinear aeroelastic response on static aeroelastic deformation [50]. LCOs were observed due to aerodynamic effects even in the absence of structural nonlinearities.

Tang and Dowell presented results from experimental and theoretical studies on the aeroelasticity of high aspect-ratio wings [51, 52]. Structural equations modeled using nonlinear beam theory were combined with the ONERA stall model to generate theoretical results [51]. Experimental and theoretical results showed good agreement on the

static aeroelastic response, flutter onset velocity and LCO frequency and mode shape. For the model used in the experiments, aerodynamic nonlinearities were found to be the cause of LCOs and the hysteresis observed in the LCO amplitude vs flow velocity graph. Results presented in the second paper using the harmonic balance method also showed good agreement with experimental data on the static aeroelastic response, flutter onset velocity and LCO frequency [52]. Romeo *et al.* modeled the nonlinear aeroelastic characteristics of a high aspect ratio wing using a second-order geometrically-exact nonlinear beam formulation and an unsteady aerodynamic model based on Wagner's indicial functions [53]. Computational results were found to be similar as those presented in Ref. [47] and [49]. Wind tunnel experiments found LCOs to exhibit hysteresis and remain stable even when the wind speed was decreased below critical speed. The flutter speed measured in the wind tunnel showed good co-relation with computational results obtained for the statically deformed beam.

Optimal static output-feedback controllers based on linear quadratic optimization theory were designed by Patil and Hodges for flutter suppression and gust-load alleviation for high aspect-ratio wings [54]. A static-output feedback based controller with a low pass filter was shown to have equivalent performance, high-frequency roll-off and stability margins as an LQG controller for flutter suppression. The same controller architecture was also seen to be effective for gust-load alleviation with proper choice of sensors. Cesnik and Brown studied the use of wing warping for roll control using piezo-electric actuators in flexible high aspect-ratio wings [55]. The wing structure was modeled using nonlinear beam theory capable of handling large deformations. Results showed that wing warping produces a higher maximum roll rate than conventional ailerons. Cesnik and Su modeled the nonlinear aeroelasticity of two highly flexible configurations [56]. The difference between steady roll-rates predicted by the fully non-linear model for a single wing configuration and a statically deformed rigid configuration was not found to be significant. Tail and fuselage flexibility were not found to be significant in determining roll rate. However, neither of these conclusions hold true for the joined-wing configuration. Fuselage

flexibility was not found to be significant in determining dynamic stability of the single wing configuration, and no interaction is found between the flutter modes of the wing and the tail structure. The flutter modes for the joined wing configuration were found to involve wing, tail and fuselage flexibility. The aft wing was found to encounter a buckling instability at particular operating points.

Smith *et al.* studied the static aeroelasticity of high-aspect ratio wings with a loosely-coupled nonlinear beam and Euler-based CFD formulation [57]. Load transfer to the structural model was found to be sensitive to beam curvature. Linear, panel-based aerodynamic models were found to give conservative results as compared to those from models using CFD. The static aeroelasticity of two high aspect-ratio configurations were studied by Palacios and Cesnik using a closely-coupled nonlinear beam and Euler-based CFD formulation [58]. The structural model was separated into a nonlinear beam model and a linear camber-bending model and a relaxation parameter was introduced to facilitate convergence of the solution. Cross-sectional deformation was seen to have a significant effect on transonic flow fields. Garcia studied the static aeroelasticity of swept and unswept high aspect-ratio wings with a closely-coupled twelve-degree-of-freedom nonlinear beam finite element and Reynolds-averaged Navier-Stokes model [59]. Static aeroelastic results generated by a linear structural model showed a nose-down twist due to the pitching moment of the airfoil section. This trend was reversed when a nonlinear structural modes was used as the large bending displacements couple with the transonic drag to give a pitch-up moment on the wing. Nonlinear aeroelastic twist effects were observed on the swept wing due to the interaction of kinematics, nonlinear bending-torsion coupling, aerodynamic loads and twist generated by the bending of a swept wing.

Vartio *et al.* devised a structural modal control for the half-span wind-tunnel model of the Sensorcraft configuration [60, 61]. This swept flying wing configuration has one leading edge and four trailing edge control surfaces. The model had accelerators mounted on the spar, strain gauges on the root and mid-spar, a rate gyro at the wing tip and a gust sensor in front. The aeroservoelastic model was built using commercial software. An LQG

controller was designed to control the angle of attack while minimizing the loads at the intersection of the outer wing with the body and damping the first bending mode. Robustness was checked by computing singular values of the controller designs. The controllers designed for gust load alleviation were shown to reduce the loads acting on the model in the presence of gusts, thereby reducing the deviation in vertical velocity, and suppress body-freedom flutter at higher dynamic pressures. An alternate controller was designed for a Sensorcraft model with pitch and plunge degrees of freedom for gust load alleviation and body-freedom-flutter suppression [62]. The dynamic model of the system used for control design was generated using system identification. Controllers were designed using an LQR approach and an LQG approach. Both controllers successfully demonstrated reduction in bending moment due to gusts and increase in the body-freedom-flutter velocity for the test cases. Structural dynamic coupling was observed between the first vertical bending mode and a harmonic of the first fore-aft bending mode. Gregory *et al.* designed an L1 adaptive controller for pitch control and altitude hold for a Sensorcraft wind tunnel model [63]. A robust linear controller was designed at one of the test points and was augmented by the adaptive controller, which maintained controller performance in the presence of uncertainties or unknown variation in the plant dynamics. Results indicated that the adaptive controller was able to compensate for an arbitrary variation in the dynamic pressure and ensure a stable response.

2.4 Flight Dynamics and Control for Flexible High-Aspect Ratio Configurations

In a series of papers, Banerjee and co-authors compared the aeroelastic and flight dynamic characteristics of a high aspect-ratio tailless sailplane with those of a sailplane with a conventional tail structure [64, 65, 66]. A study of flutter characteristics revealed that the instability of the tailless airplane resulted from the coupling of the short pe-

riod flight dynamic mode with the first bending mode of the wing, whereas the sailplane with the conventional tail structure exhibited classic bending-torsion flutter [64]. The flutter speed of the tailless sailplane showed very little dependence on the mass, center of gravity position and wing sweep angle and had a linear relationship with the pitching moment of inertia. A detailed study of the flutter modes carried out in a follow-up paper highlighted the coupling between the short-period modes and the first bending mode for the high-aspect ratio tailless configuration at the point of instability [65]. Banerjee and Cal investigated the effect of flexibility and unsteady aerodynamics on the short-period mode for two speeds before the onset of flutter [66]. The analysis used Theodorsen's unsteady aerodynamic model, and extended its applicability to non-oscillatory motion by using complex reduced frequencies. As seen in previous papers, coupling between the first bending and short-period mode was observed with no contribution from higher structural modes. The inclusion of flexibility in the analysis was found to increase the frequency of the short-period mode below flutter speeds. As the flight speed as increased, the damping in the mode was found to decrease until it becomes zero at the onset of flutter.

As part of the *Daedalus* project in the late 1980s', researchers at MIT designed, built and flew human-powered airplanes. These airplanes were characterized by very flexible structures, high aspect-ratio wings and low wing loadings. The research carried out on the *Michelob Light Eagle* model as part of this project was recorded in a series of two papers on flight testing [67] and aeroelastic characteristics of the complete airplane [68]. It was found during flight tests that the airplane showed significant static aeroelastic deformation. These deformations and unsteady aerodynamic effects have to be accounted for in analytical models used for flight dynamic predictions. The flexibility of the tail boom structure was found to significantly affect lateral control. Ailerons proved to be ineffective, resulting in significant adverse yaw and very small roll rates. Inputs to controls surfaces at high frequencies were found to excite structural modes while having little effect on the overall airplane motion. In the second paper, van Schoor and von Flotow studied the coupled aeroelasticity and flight dynamics of the *Michelob Light Eagle* [68]. The structure

was modeled using beam finite elements. Generalized modal forces were computed using a two-dimensional strip aerodynamic model that accounted for unsteady drag and leading-edge suction forces. It was found that lateral and longitudinal modes could be decoupled. Stability results were found to be significantly altered by the inclusion of flexible modes in the analysis, which pointed to a significant coupling between rigid body modes and structural modes. Use of complex reduced frequencies in Theodorsen's model was found to be necessary and modeling of unsteady drag terms was found to be not necessary for accurate analysis.

Patil *et al.* studied the aeroelastic and flight dynamic characteristics of a representative HALE configuration with a high aspect-ratio wing and a tail structure [69]. The wing was modeled using a geometrically-exact, intrinsic beam formulation and aerodynamic loads were calculated using an unsteady finite-state airloads model. Linear flutter analysis was shown to be inaccurate as the flutter speed was found to decrease as a result of static structural deformation. Spanwise structural deformation rotates the lift vector away from the vertical direction. This resulted in a higher angle of attack at trim as compared to predictions from a linear model. Flight dynamic modes and low frequency aeroelastic modes were significantly altered due to coupling. However, higher frequency aeroelastic modes did not show coupling with flight dynamics, though they do have a dependence on the trim state. They also studied the interaction between flight dynamics and wing limit cycle oscillations (LCOs) in flexible, high aspect-ratio configurations [70]. LCO characteristics of three cases were studied; a cantilevered wing-only model, a complete aircraft model including rigid body modes before trim, and the complete aircraft model at trim. Stall effects were found to limit the amplitude of unstable oscillations for all three cases. In the cantilevered wing case, the wing was found to oscillate about a deformed shape caused by aerodynamic loading under periodic motion. LCOs were found to be of a lower amplitude if rigid body modes were included in the model. The flight dynamic modes and the LCO response at trim were found to be coupled. These results indicated that it was necessary to use the complete airplane model at trim rather than a

cantilevered wing to characterize LCOs.

Patil and Hodges studied the flight dynamics of a flexible flying wing HALE configuration and compared it to a rigid body flight dynamics of the same configuration [7] using a similar aeroelastic model as the one used in Ref. [69]. The flying wing was modeled with multiple engines and control surfaces. Longitudinal trim and stability were analysed, and results from a time marching scheme were presented. Trim and stability results were computed by varying the payload at the center of the flying wing. The flap deflection required for trim computed using a flexible model was found to differ from the flap deflection computed using a rigid airplane model. The thrust required for trim was not found to vary significantly as drag in these airplane is mainly generated by skin friction. Strong coupling was seen between the structural and flight dynamic modes. The short-period mode was replaced by two real roots and the phugoid mode was found to go unstable as the payload was increased in the flexible model. Su and Cesnik analysed a similar configuration and included a stall model for non-linear time-marching simulation [71]. Their paper also studied the effect of gust on airplane trajectory and dynamics, and the effect of skin wrinkling on airplane dynamics. Gust was seen to excite unstable flight dynamic modes and cause a deviation in the airplane trajectory. It was found that the effect of stall on the dynamics and trajectory of the airplane is significant and should not be ignored. Skin wrinkling was seen to affect lateral dynamics of the airplane. Chang *et al.* extended the model in Ref. [7] to include a flexible fuselage and tail structure [72]. Stability was found to vary monotonically with curvature, with a wing deformed in a U-shape being most stable and the inverted U-shaped wing being least stable. As fuselage length is increased, the increased pitch inertia destabilizes the first longitudinal mode while the horizontal tail structure stabilizes the same mode.

Shearer and Cesnik studied the open-loop response of a wing-body HALE configuration in the time domain to control inputs in the longitudinal and lateral-directional planes [73]. A time marching algorithm was implemented on a full non-linear model, a linearized model and a reduced-order model. For the representative configuration considered in the

paper, they found that a linearized model was necessary for analyzing maneuvers in the plane of symmetry and the full non-linear model was necessary for analyzing asymmetric maneuvers. This work was extended by the authors to control system design for a wing-body HALE configuration [74]. A flight controller was designed to be effective in the absence of divergence, flutter or LCOs. The controller utilized a two loop process with a fast inner-loop control for the dynamics of the airplane and a slow outer-loop control using a PID design for controlling flight path angle, Euler roll angle and the corresponding rates. Unsteady aerodynamic effects were neglected during the design of the controller. Longitudinal and lateral modes were decoupled, and it was assumed that longitudinal modes were not affected by elastic states. An LQR controller was designed for lateral dynamics and a non-linear dynamic inversion controller was designed for longitudinal dynamics. For the design of the controller for lateral dynamics, full state feedback including elastic states was assumed. The non-linear dynamic inversion controller for longitudinal dynamics was designed only over rigid-body states. A third-order low-pass Butterworth filter was used to eliminate high-frequency numerical error generated during simulations. Simulation results were presented for turning flight with altitude change in full fuel and empty fuel conditions.

Love *et al.* carried out aeroelastic analysis for a swept, flying wing configuration designed for the Sensorcraft program [75]. The configuration was found to be susceptible to body-freedom-flutter typically seen in flexible flying wing configurations. This instability results from the coupling between rigid body short period mode and the bending mode. Consequently, their work focused on design studies to ensure sufficient margin from body-freedom-flutter in the flight envelope. Active flutter control was recommended to resolve this problem, as design modifications within the scope of the configuration were found to be inadequate. Tuzcu *et al.* modeled the dynamics of a Blended Wing Body configuration using a linear elastic beam and non-linear aerodynamics, and the tail as a rigid structure [76]. Aeroelastic analysis carried out on the configuration showed coupling between rigid body and elastic modes. Predictions from the flexible airplane model were compared to

those from a rigid body model and a flexible model with no rigid body degrees of freedom. Once again, it was found that the flexible model with no rigid body degrees of freedom generated incorrect results. Use of the complete flexible airplane model was found to be necessary to accurately predict flutter speeds and for control design.

As seen in the literature review, extensive research has been carried out over the years on modeling the coupled flight dynamics and aeroelasticity of conventional airplane configurations and for flight control design in the presence of this coupling. However, this dissertation focuses on understanding the flight dynamic characteristics unique to highly flexible, high aspect-ratio flying wings in the presence of coupling between aeroelasticity and flight dynamics, and on flight control design for path following.

Chapter 3

Integrated Model of Aeroelasticity and Flight Dynamics

3.1 Overview

The aeroelastic model used in this dissertation was presented in a paper by Patil and Hodges [7] and is reviewed in this chapter. The modeling consists of two sections: a structural model that accounts for both rigid-body motion and elastic deformation and a loads model for externally applied loads on the HALE configuration. The loads model can itself be subdivided into aerodynamic, gravitational and propulsive models based on the source of the applied loads.

Patil and Hodges have shown that the dominant nonlinearities in a very high-aspect ratio flying wing are the dependence of structural dynamic characteristics on wing deformation, and interface nonlinearities associated with the calculation of local angle of attack on a wing section and transfer of airloads from the local to the global frame [47]. The effect of structural nonplanarities on the aerodynamic loads is found to be negligible, and three dimensional effects are found to be quite small due to the very high aspect-ratio of the

configuration. It was found that linear structural models captured the static deformation, but did not accurately predict the structural dynamics of the deformed wing. Based on these conclusions, the aeroelasticity of the flying wing is modeled using a combination of geometrically-exact, nonlinear beam theory and two-dimensional unsteady aerodynamics.

The structural model can be broken up into three parts: the equations for the dynamics of the beam, which relate the forces and moments acting on the beam to the rate of change of linear and angular momentum, the equations for kinematics, which relate the variation in velocity and angular velocity along the length of the beam to the rate of change of strain and curvature, and the constitutive relations between the cross-sectional forces and moments and the strain and curvature of the beam.

The dynamics of the flying wing is modeled using a geometrically exact, intrinsic, beam formulation developed by Hodges [77]. The model is called as an intrinsic model as the equations are written in terms of the velocity and angular velocity without use of the rotation and displacement variables. The model is geometrically exact in the sense that it captures exactly the geometry of the beam after deformation. The kinematic equations used in the structural model are also intrinsic, and are derived in Ref. [78]. A linear constitutive law is used to relate the sectional forces and moments to the strains and curvatures. Taken together, the structural model is a large-displacement, small-strain model for a beam.

The aerodynamic model consists of two parts: the airloads model, which computes the sectional forces and moments, and the inflow model, which computes the downwash due to shed vortices on the airfoil. In this dissertation, the airloads model used is the one developed by Peters and Johnson [79] and the inflow model used is developed by Peters, Karunamoorthy and Cao for two-dimensional thin airfoils [80]. The aerodynamic model is augmented to account for the effect of skin friction drag, which was found to be the predominant contributor to the net drag on the airplane [7].

The flying wing configuration used in this dissertation has five engines evenly spaced

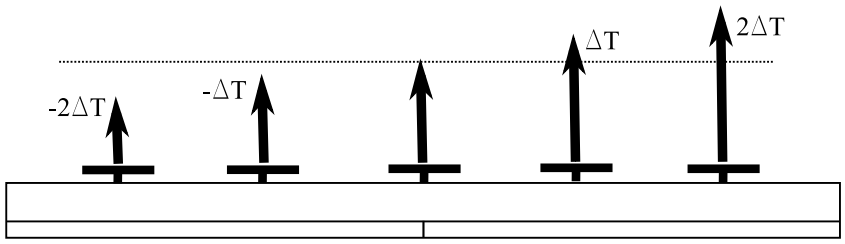

Figure 3.1: Differential Thrust

along the wing span as shown in Fig. 3.1. The entire trailing edge is actuated, and is split into two sections along the span. The two sections deflect in the same direction for pitch control and differentially for roll control. The total control surface deflection for each section is calculated by adding up these two components. As the flying wing does not have a rudder or vertical tail, yaw control is obtained by linearly redistributing thrust across the different engines. The differential thrust ΔT is chosen such that it is zero at the center and changes by integral multiples across the wingspan.

3.2 Structural Model

3.2.1 Geometrically-Exact Beam Equations

Two axis systems are defined for formulating the equations for beam dynamics as shown in Fig. 3.2. The root frame R is defined with the origin at the center of the beam axis. The structural equations are formulated in the deformed beam axis system B which has its origin on the beam axis. The local 'X' axis at any point on the beam is aligned along the span of the wing, and the 'Z' axis is defined to be perpendicular to the surface and points vertically upwards. The local 'Y' axis is defined so as to complete the triad. The geometrically-exact intrinsic equations that are used to model beam dynamics are given

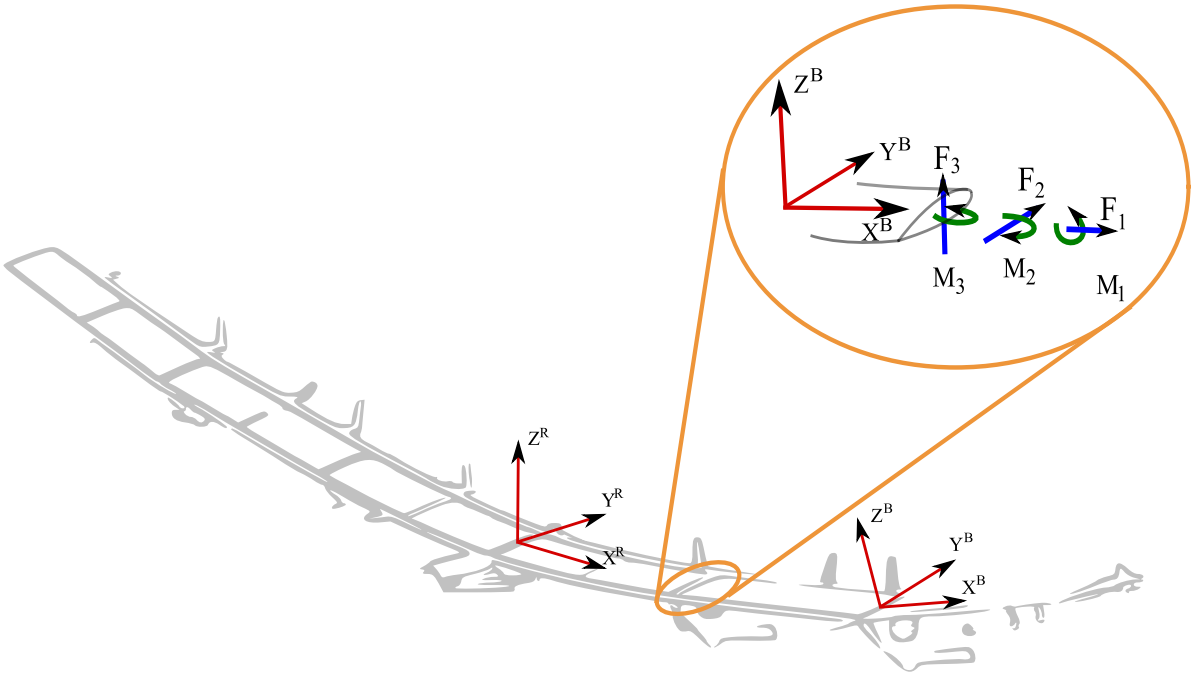

Figure 3.2: Beam Axis system

by [77]:

$$\mathbf{F}' + (\widetilde{\mathbf{k}} + \widetilde{\kappa})\mathbf{F} + \mathbf{f} = \dot{\mathbf{P}} + \widetilde{\mathbf{\Omega}}\mathbf{P} \tag{3.1}$$

$$\mathbf{M}' + (\widetilde{\mathbf{k}} + \widetilde{\kappa})\mathbf{M} + (\widetilde{\mathbf{e_1}} + \widetilde{\epsilon})\mathbf{F} + \mathbf{m} = \dot{\mathbf{H}} + \widetilde{\mathbf{\Omega}}\mathbf{H} + \widetilde{\mathbf{V}}\mathbf{P} \tag{3.2}$$

where at any point on the beam axis, $\mathbf{F}$ and $\mathbf{M}$ represent the forces and moments respectively on the cross-section, $\mathbf{k}$ represents the curvature of the undeformed beam, ϵ and κ represent the generalized strains and curvatures, $\mathbf{f}$ and $\mathbf{m}$ represent the external forces and moments per unit span respectively, $\mathbf{P}$ and $\mathbf{H}$ represent the linear and angular momentum respectively, $\mathbf{V}$ and $\mathbf{\Omega}$ represent the linear and angular velocity respectively, and $\mathbf{e}_1$ represents the unit vector $[1\ \ 0\ \ 0]^T$. The generalized strain ϵ and curvature κ are

defined as [77],

$$\begin{aligned} \epsilon &= \mathcal{C}^{Bb}(\mathbf{e}_1 + {}^b\mathbf{u}' + {}^b\widetilde{\mathbf{k}}{}^b\mathbf{u}) - \mathbf{e}_1 \\ \kappa &= {}^B\mathbf{K} - {}^b\mathbf{k} \end{aligned}$$

where

$${}^B\widetilde{\mathbf{K}} = -\mathcal{C}^{Bb'}\mathcal{C}^{bB} + \mathcal{C}^{Bb}\widetilde{\mathbf{k}}\mathcal{C}^{bB}$$

$\mathcal{C}^{Bb}$ represents the rotation matrix from the undeformed local frame b to the deformed local frame B and ${}^b\mathbf{u}$ represents the measure numbers of the displacement of a point on the beam axis in the undeformed local frame b.

In the above equations, the operator $(\ )'$ represents a derivative along the local X axis, $(\dot{})$ represents a time derivative in the local frame and the $(\tilde{})$ operator is defined for a vector $\mathbf{v}$ as,

$$\widetilde{\mathbf{v}} = \begin{bmatrix} 0 & -v_3 & v_2 \\ v_3 & 0 & -v_1 \\ -v_2 & v_1 & 0 \end{bmatrix}$$

These equations for dynamics of the beam are augmented by the following intrinsic kinematic equations which relate the variation of linear and angular velocity along the wing span to the time-rate of change of strain and curvature [78]:

$$\mathbf{V}' + (\widetilde{\mathbf{k}} + \widetilde{\kappa})\mathbf{V} + (\widetilde{\mathbf{e_1}} + \widetilde{\epsilon})\mathbf{\Omega} = \dot{\epsilon} \tag{3.3}$$

$$\mathbf{\Omega}' + (\widetilde{\mathbf{k}} + \widetilde{\kappa})\mathbf{\Omega} = \dot{\kappa} \tag{3.4}$$

The spatial derivatives in the above equations are of order one, which is the lowest possible order.

The position vector of a point on the deformed beam axis in the root frame ($\mathbf{r}_B$) and the rotation of the local B frame relative to the R frame ($\mathcal{C}^{BR}$) can be obtained using,

$$\mathbf{r}'_B = \mathcal{C}^{RB}(\epsilon + \mathbf{e}_1) \tag{3.5}$$

$$\mathcal{C}^{BR'} = -(\widetilde{\kappa} + \widetilde{\mathbf{k}})\mathcal{C}^{BR} \tag{3.6}$$

Using a small-strain and slender beam assumption, the strains and curvatures are related to the internal forces and moments using the following linear relation [7]:

$$\begin{Bmatrix} \epsilon \\ \kappa \end{Bmatrix} = \begin{bmatrix} \mathcal{R} & \mathcal{S} \\ \mathcal{S}^T & \mathcal{T} \end{bmatrix} \begin{Bmatrix} \mathbf{F} \\ \mathbf{M} \end{Bmatrix} \tag{3.7}$$

For an isotropic beam which has the shear center and tension axis coincident with the reference axis, the constitutive relation is given in the local frame by [78],

$$\begin{Bmatrix} \epsilon_1 \\ \epsilon_2 \\ \epsilon_3 \\ \kappa_1 \\ \kappa_2 \\ \kappa_3 \end{Bmatrix} = \begin{bmatrix} 1/EA & 0 & 0 & 0 & 0 & 0 \\ 0 & 1/k_2GA & 0 & 0 & 0 & 0 \\ 0 & 0 & 1/k_3GA & 0 & 0 & 0 \\ 0 & 0 & 0 & 1/GJ & 0 & 0 \\ 0 & 0 & 0 & 0 & 1/EI_2 & 0 \\ 0 & 0 & 0 & 0 & 0 & 1/EI_3 \end{bmatrix} \begin{Bmatrix} F_1 \\ F_2 \\ F_3 \\ M_1 \\ M_2 \\ M_3 \end{Bmatrix} \tag{3.8}$$

where ϵ_1 represents the extensional strain, and ϵ_2, ϵ_3 represent the transverse shear strain measures of the reference line. $\kappa_1, \kappa_2, \kappa_3$ represent the curvature of the beam under torsional and bending loads. G represents the shear modulus, E represents Young's modulus, J represents the torsional constant, I_2 and I_3 represent the area moment of inertia along the local Y and Z direction, k_2 and k_3 represent the shear correction factor and A represents the cross-sectional area.

The equations relating the linear and angular momentum with the linear and angular

velocities can be written as:

$$\begin{Bmatrix} \mathbf{P} \\ \mathbf{H} \end{Bmatrix} = \begin{bmatrix} \mu\mathbb{I} & -\mu\widetilde{\xi} \\ \mu\widetilde{\xi} & \mathcal{I} \end{bmatrix} \begin{Bmatrix} \mathbf{V} \\ \mathbf{\Omega} \end{Bmatrix} \tag{3.9}$$

where μ represents the sectional mass per unit length, $\mathbb{I}$ represents a 3×3 identity matrix, ξ represents the position vector of the sectional center of gravity and $\mathcal{I}$ represents the sectional moment of inertia matrix.

Equivalence to Equations for Rigid Body Modes

The equations for rigid body modes can be separated and obtained from Eqs. (3.1) and (3.2) as follows. Since both equations are written in the local frame, pre-multiply all terms by $\mathcal{C}^{RB}$ to obtain components in the root frame, and integrate in the root frame along the beam axis.

$$\begin{aligned} \int_0^b \left(\mathcal{C}^{RB}\mathbf{F}' + \mathcal{C}^{RB}(\widetilde{\mathbf{k}} + \widetilde{\kappa})\mathbf{F} + \mathcal{C}^{RB}\mathbf{f} \right) dx &= \int_0^b \mathcal{C}^{RB} \left(\dot{\mathbf{P}} + \widetilde{\mathbf{\Omega}}\mathbf{P} \right) dx \\ \int_0^b \left(\mathcal{C}^{RB}\mathbf{M}' + \mathcal{C}^{RB}(\widetilde{\mathbf{k}} + \widetilde{\kappa})\mathbf{M} + \mathcal{C}^{RB}(\widetilde{\mathbf{e_1}} + \widetilde{\epsilon})\mathbf{F} + \mathcal{C}^{RB}\mathbf{m} \right) dx &= \int_0^b \mathcal{C}^{RB} \left(\dot{\mathbf{H}} + \widetilde{\mathbf{\Omega}}\mathbf{H} \right) dx \\ &\quad + \int_0^b \mathcal{C}^{RB}\widetilde{\mathbf{V}}\mathbf{P} dx \end{aligned} \tag{3.10}$$

Differentiate the matrix identity $\mathcal{C}^{BR}\mathcal{C}^{RB} = \mathbb{I}$ along the beam axis, and re-arranging terms, we obtain,

$$\mathcal{C}^{RB\prime} = -\mathcal{C}^{RB}\mathcal{C}^{BR\prime}\mathcal{C}^{RB}$$

Substituting the expression for $\mathcal{C}^{BR'}$ from Eq. (3.6), $\mathcal{C}^{BR'}$ can be written as,

$$\mathcal{C}^{RB'} = \mathcal{C}^{RB}(\widetilde{\mathbf{k}} + \widetilde{\kappa}) \tag{3.11}$$

Substituting Eq. (3.5) and (3.11) in Eqn. (3.10) and rewriting time derivatives in the inertial frame, the equations can be written as,

$$\int_0^b \left(\left(\mathcal{C}^{RB}\mathbf{F}\right)' + \mathcal{C}^{RB}\mathbf{f} \right) dx = \int_0^b \mathcal{C}^{RB} \frac{d}{dt}\bigg|_I \mathbf{P} dx \tag{3.12}$$

$$\int_0^b \left(\left(\mathcal{C}^{RB}\mathbf{M}\right)' + \mathbf{r}_B' \times \mathcal{C}^{RB}\mathbf{F} + \mathcal{C}^{RB}\mathbf{m} \right) dx = \int_0^b \mathcal{C}^{RB} \frac{d}{dt}\bigg|_I \mathbf{H} dx + \int_0^b \mathcal{C}^{RB}\widetilde{\mathbf{V}}\mathbf{P} dx \tag{3.13}$$

Write the position vector $\mathbf{r}_B$ of any point on the beam from the origin of the root axis in terms of the position of the center-of-gravity of the airplane from the origin ξ_B and the position vector of the point from the center-of-gravity $\mathbf{r}_B^{cg}$. Since the derivative of ξ_B along the beam axis is zero, the following expressions are obtained.

$$\begin{aligned} \mathbf{r}_B &= \xi_B + \mathbf{r}_B^{cg} \\ \mathbf{r}_B' &= \mathbf{r}_B^{cg\prime} \end{aligned}$$

Take the cross-product of each term inside the integral in Eq. (3.12) with $\mathbf{r}_B^{cg}$ and add to Eq. (3.13) to obtain,

$$\int_0^b \left(\left(\mathcal{C}^{RB}\mathbf{F}\right)' + \mathcal{C}^{RB}\mathbf{f} \right) dx = \frac{d}{dt}\bigg|_I \int_0^b \mathcal{C}^{RB}\mathbf{P} dx \tag{3.14}$$

$$\begin{aligned} \int_0^b \left(\left(\mathcal{C}^{RB}\mathbf{M}\right)' + \left(\mathbf{r}_B^{cg} \times \mathcal{C}^{RB}\mathbf{F}\right)' + \mathcal{C}^{RB}\mathbf{m} + \mathbf{r}_B^{cg} \times \mathcal{C}^{RB}\mathbf{f} \right) dx &= \int_0^b \frac{d}{dt}\bigg|_I \mathcal{C}^{RB}\mathbf{H} dx \\ &+ \int_0^b \mathcal{C}^{RB}\widetilde{\mathbf{V}}\mathbf{P} dx + \int_0^b \left(\mathbf{r}_B^{cg} \times \frac{d}{dt}\bigg|_I \mathcal{C}^{RB}\mathbf{P} \right) dx \end{aligned} \tag{3.15}$$

The integral of the total linear momentum along the beam axis can be written in terms of the total mass of the airplane and the velocity of the center of gravity as,

$$\int_0^b \mathcal{C}^{RB}\mathbf{P}dx = M_{total}{}^R\mathbf{V}_{cg} \tag{3.16}$$

The velocity of any point on the beam $\mathbf{V}$ can be broken up into the velocity of the center-of-gravity of the airplane $\mathbf{V}_{cg}$ and the relative velocity of the point with respect to the center-of-gravity $\mathbf{V}_{rel}$. The second term on the right hand side of Eq. (3.15) can now be written as,

$$\int_0^b \mathcal{C}^{RB}\widetilde{\mathbf{V}}\mathbf{P}dx = {}^R\mathbf{V}_{cg} \times \int_0^b \mathcal{C}^{RB}\mathbf{P}dx + \int_0^b {}^R\mathbf{V}_{rel} \times \mathcal{C}^{RB}\mathbf{P}dx = \int_0^b \frac{d}{dt}\bigg|_I \mathbf{r}_B^{cg} \times \mathcal{C}^{RB}\mathbf{P}dx$$

Since the sectional forces $\mathbf{F}$ and moments $\mathbf{M}$ at both free ends of the beam are zero, Eqs. (3.14)-(3.15) can be written as,

$$^R\mathbf{f}_{total} = \frac{d}{dt}\bigg|_I M_{total}{}^R\mathbf{V}_{cg} \tag{3.17}$$

$$^R\mathbf{m}^{cg}_{total} = \frac{d}{dt}\bigg|_I \int_0^b \left({}^R\mathbf{H} + \mathbf{r}_B^{cg} \times {}^R\mathbf{P}\right) dx \tag{3.18}$$

Equivalence to Linear Structural Dynamics Equations

Standard linear equations for structural dynamics of beams in bending and torsion can be obtained from Eqs. (3.1) and (3.2). Neglecting non-linear terms, these equations reduce to,

$$\mathbf{F}' + \mathbf{f} = \mu\dot{\mathbf{V}} \tag{3.19}$$

$$\mathbf{M}' + \widetilde{\mathbf{e_1}}\mathbf{F} + \mathbf{m} = \mathcal{I}\dot{\mathbf{\Omega}} \tag{3.20}$$

Assuming the external bending moment per unit length $[m_2 \;\; m_3]$ and the bending moment of inertia $[I_2 \;\; I_3]$ to be zero, the following six equations are obtained,

$$F_1{}' + f_1 = \mu \dot{V}_1 \tag{3.21}$$

$$F_2{}' + f_2 = \mu \dot{V}_2 \tag{3.22}$$

$$F_3{}' + f_3 = \mu \dot{V}_3 \tag{3.23}$$

$$M_1{}' + m_1 = I_1 \dot{\Omega}_1 \tag{3.24}$$

$$M_2{}' - F_3 = 0 \tag{3.25}$$

$$M_3{}' + F_2 = 0 \tag{3.26}$$

The linearized versions of the kinematic equations given in Eqs. (3.1) and (3.2) are,

$$\mathbf{V}' + \widetilde{\mathbf{e_1}}\mathbf{\Omega} = \dot{\epsilon} \tag{3.27}$$

$$\mathbf{\Omega}' = \dot{\kappa} \tag{3.28}$$

Ignoring shear deformation, the above equations can be combined with the constitutive relations given in Eq. (3.8) to give,

$$EAV_1{}' = \dot{F}_1 \tag{3.29}$$

$$V_2{}' - \Omega_3 = 0 \tag{3.30}$$

$$V_3{}' + \Omega_2 = 0 \tag{3.31}$$

$$GJ\Omega_1{}' = \dot{M}_1 \tag{3.32}$$

$$EI_2\Omega_2{}' = \dot{M}_2 \tag{3.33}$$

$$EI_3\Omega_3{}' = \dot{M}_3 \tag{3.34}$$

Eqs. (3.22)-(3.23) and (3.25)-(3.26) together give linear equations for structural dy-

namics in bending, and are identical to the equations derived by Meirovitch [81],

$$-\frac{\partial^2 M_3}{\partial x^2} + f_2 = \mu \frac{\partial V_2}{\partial t} \tag{3.35}$$

$$\frac{\partial^2 M_2}{\partial x^2} + f_3 = \mu \frac{\partial V_3}{\partial t} \tag{3.36}$$

The above equations can be differentiated with respect to time, and combined with Eqs. (3.30)-(3.31) and Eqs. (3.33)-(3.34) to give,

$$-\frac{\partial^2}{\partial x^2}\left(EI_3 \frac{\partial^2 V_2}{\partial x^2}\right) + \dot{f}_2 = \mu \frac{\partial^2 V_2}{\partial t^2} \tag{3.37}$$

$$-\frac{\partial^2}{\partial x^2}\left(EI_2 \frac{\partial^2 V_3}{\partial x^2}\right) + \dot{f}_3 = \mu \frac{\partial^2 V_3}{\partial t^2} \tag{3.38}$$

Eq. (3.21) and (3.24) correspond to the equations for structural dynamics in the axial and torsional mode respectively. These equations can be combined with Eqs.(3.29) and (3.32) to give,

$$\frac{\partial}{\partial x}\left(EA \frac{\partial V_1}{\partial x}\right) + \dot{f}_1 = \mu \frac{\partial^2 V_1}{\partial t^2} \tag{3.39}$$

$$\frac{\partial}{\partial x}\left(GJ \frac{\partial \Omega_1}{\partial x}\right) + \dot{m}_1 = I_1 \frac{\partial^2 \Omega_1}{\partial t^2} \tag{3.40}$$

Finite difference discretization

Consider a vector $\mathbf{X}$. Denote the nodal values of the vector by $\widehat{\mathbf{X}}_l^n$ and $\widehat{\mathbf{X}}_r^n$, where the superscript denotes the node number, the subscript denotes the left or right side of the node, and the hat denotes that it is nodal value. For the n^{th} element,the spatial derivative and the mean value over the element are given by,

$$\mathbf{X}' = \frac{\widehat{\mathbf{X}}_l^{n+1} - \widehat{\mathbf{X}}_r^n}{dl} \tag{3.41}$$

$$\mathbf{X} = \overline{\mathbf{X}}^n = \frac{\widehat{\mathbf{X}}_l^{n+1} + \widehat{\mathbf{X}}_r^n}{2} \tag{3.42}$$

Eqs.(3.1)-(3.4) are re-written in discretized form as,

$$\frac{\widehat{\mathbf{F}}_l^{n+1} - \widehat{\mathbf{F}}_r^n}{dl} + (\widetilde{\overline{\kappa}^n} + \widetilde{\mathbf{k}^n})\overline{\mathbf{F}}^n + \overline{\mathbf{f}}^n - \dot{\overline{\mathbf{P}}}^n - \widetilde{\overline{\mathbf{\Omega}}^n}\overline{\mathbf{P}}^n = 0 \tag{3.43}$$

$$\frac{\widehat{\mathbf{M}}_l^{n+1} - \widehat{\mathbf{M}}_r^n}{dl} + (\widetilde{\overline{\kappa}^n} + \widetilde{\mathbf{k}^n})\overline{\mathbf{M}}^n + (\widetilde{\mathbf{e}_1} + \widetilde{\overline{\epsilon}^n})\overline{\mathbf{F}}^n + \overline{\mathbf{m}}^n - \dot{\overline{\mathbf{H}}}^n - \widetilde{\overline{\mathbf{\Omega}}^n}\overline{\mathbf{H}}^n - \widetilde{\overline{\mathbf{V}}^n}\overline{\mathbf{P}}^n = 0 \tag{3.44}$$

$$\frac{\widehat{\mathbf{V}}_l^{n+1} - \widehat{\mathbf{V}}_r^n}{dl} + (\widetilde{\overline{\kappa}^n} + \widetilde{\mathbf{k}^n})\overline{\mathbf{V}}^n + (\widetilde{\mathbf{e}_1} + \widetilde{\overline{\epsilon}^n})\overline{\mathbf{\Omega}}^n - \dot{\overline{\epsilon}}^n = 0 \tag{3.45}$$

$$\frac{\widehat{\mathbf{\Omega}}_l^{n+1} - \widehat{\mathbf{\Omega}}_r^n}{dl} + (\widetilde{\overline{\kappa}^n} + \widetilde{\mathbf{k}^n})\overline{\mathbf{\Omega}}^n - \dot{\overline{\kappa}}^n = 0 \tag{3.46}$$

This discretization scheme was found to be second-order accurate along the length of the beam [78]. In addition, it satisfies both conservation integrals presented in the paper relating to the change in generalized momentum and change in total mechanical energy.

3.2.2 Gravitational Model

The force and moment due to gravitational effects are modeled as

$$\mathbf{f}_g = \mu\mathbf{g} \tag{3.47}$$

$$\mathbf{m}_g = \mu\widetilde{\xi}\mathbf{g} \tag{3.48}$$

where $\mathbf{g}$ is the gravity vector. The components of $\mathbf{g}$ are known in the inertial frame. The components of the gravity vector $\mathbf{g}$ in the deformed frame at all the nodes can be calculated using the following equations:

$$\mathbf{g}' + (\widetilde{\kappa} + \widetilde{\mathbf{k}})\mathbf{g} = 0 \tag{3.49}$$

$$\dot{\mathbf{g}} + \widetilde{\mathbf{\Omega}}\mathbf{g} = 0 \tag{3.50}$$

which in the discretized form can be written as

$$\frac{\widehat{\mathbf{g}}_l^{n+1} - \widehat{\mathbf{g}}_r^n}{dl} + (\widetilde{\overline{\kappa}^n} + \widetilde{\mathbf{k}^n})\overline{\mathbf{g}}^n = 0 \tag{3.51}$$

$$\dot{\widehat{\mathbf{g}}} + \widetilde{\widehat{\mathbf{\Omega}}}\widehat{\mathbf{g}} = 0 \tag{3.52}$$

In the above set of equations, the time-differentiated one is satisfied at one reference node; following which the spatially-differentiated equation can be used to obtain components of the $\mathbf{g}$ vector at other nodes. Each equation represents a set of three scalar equations. Since the magnitude of the $\mathbf{g}$ vector is a constant (represented by g_0), one of the three dynamic equations is replaced by this magnitude constraint. The dynamic equation at the reference node n_g is re-written as

$$(\mathbf{e}_1\mathbf{e}_1^T + \mathbf{e}_2\mathbf{e}_2^T)\dot{\widehat{\mathbf{g}}}^{n_g} + (\mathbf{e}_1\mathbf{e}_1^T + \mathbf{e}_2\mathbf{e}_2^T)\widetilde{\widehat{\mathbf{\Omega}}}^{n_g}\widehat{\mathbf{g}}^{n_g} + \mathbf{e}_3|\widehat{\mathbf{g}}^{n_g}| = \mathbf{e}_3 g_0 \tag{3.53}$$

3.2.3 Propulsive Model, nodal masses, and slope discontinuities

To account for the presence of nodal mass, nodal force (thrust) and slope discontinuities the internal force on one side of the node is modeled as being different from the internal force on the other side of the node. Thus the nodal equations are,

$$\widehat{\mathbf{F}}_r^n - \widehat{\mathcal{C}}_{lr}^{n^T}\widehat{\mathbf{F}}_l^n + \widehat{\mathbf{f}}_T^n + \widehat{\mu}^n\widehat{\mathbf{g}}_r^n - \dot{\widehat{\mathbf{P}}}_r^n - \widetilde{\widehat{\mathbf{\Omega}}}_r^n\widehat{\mathbf{P}}_r^n = 0 \tag{3.54}$$

$$\widehat{\mathbf{M}}_r^n - \widehat{\mathcal{C}}_{lr}^{n^T}\widehat{\mathbf{M}}_l^n + \widehat{\mathbf{m}}_T^n + \widehat{\mu}^n\widetilde{\widehat{\xi}^n}\widehat{\mathbf{g}}_r^n - \dot{\widehat{\mathbf{H}}}_r^n - \widetilde{\widehat{\mathbf{\Omega}}}_r^n\widehat{\mathbf{H}}_r^n - \widetilde{\widehat{\mathbf{V}}}_r^n\widehat{\mathbf{P}}_r^n = 0 \tag{3.55}$$

where $\widehat{\mathbf{f}}_T^n$ is the discrete nodal thrust force defined in the reference frame corresponding to the right side of the node, $\widehat{\mathbf{m}}_T^n$ is the corresponding nodal moment, $\widehat{\mu}^n$ is the concentrated nodal mass, and $\widehat{\xi}^n$ is the corresponding mass offset. $\widehat{\mathbf{P}}_r^n$ and $\widehat{\mathbf{H}}_r^n$ are the linear and angular

momenta of the concentrated modal mass, given by

$$\begin{Bmatrix} \widehat{\mathbf{P}}_r^n \\ \widehat{\mathbf{H}}_r^n \end{Bmatrix} = \begin{bmatrix} \widehat{\mu}^n \mathbb{I} & -\widehat{\mu}^n \widetilde{\widehat{\xi}^n} \\ \widehat{\mu}^n \widetilde{\widehat{\xi}^n} & \widehat{\mathcal{I}}^n \end{bmatrix} \begin{Bmatrix} \widehat{\mathbf{V}}_r^n \\ \widehat{\mathbf{\Omega}}_r^n \end{Bmatrix} + \begin{Bmatrix} 0 \\ \widehat{\mathbf{H}}_{\text{engine}}^n \end{Bmatrix} \tag{3.56}$$

where $\widehat{\mathcal{I}}^n$ is the mass moment of inertia matrix of the nodal mass and $\widehat{\mathbf{H}}_{\text{engine}}^n$ is the angular momentum of the engine.

A discontinuity in the slope of the beam at the node is accounted for using the following expressions,

$$\widehat{\mathbf{V}}_l^n = \widehat{\mathcal{C}}_{lr}^n \widehat{\mathbf{V}}_r^n \tag{3.57}$$

$$\widehat{\mathbf{\Omega}}_l^n = \widehat{\mathcal{C}}_{lr}^n \widehat{\mathbf{\Omega}}_r^n \tag{3.58}$$

$$\widehat{\mathbf{g}}_l^n = \widehat{\mathcal{C}}_{lr}^n \widehat{\mathbf{g}}_r^n \tag{3.59}$$

The vectors $\widehat{\mathbf{V}}_l^n$, $\widehat{\mathbf{\Omega}}_l^n$ and $\widehat{\mathbf{g}}_l^n$ can now be replaced by $\widehat{\mathbf{V}}_r^n$, $\widehat{\mathbf{\Omega}}_r^n$ and $\widehat{\mathbf{g}}_r^n$, thus reducing the number of variables.

3.3 Aerodynamic Model

The aerodynamic forces and moments acting on the wing are computed using Peters and Johnson's two dimensional unsteady airloads model [79]. The sectional forces and moments are written as,

$$\mathbf{f}_{aero}^n = \frac{\rho c^n}{2} \begin{Bmatrix} 0 \\ f_2 \\ f_3 \end{Bmatrix} \qquad \mathbf{m}_{aero}^n = \frac{\rho {c^n}^2}{2} \begin{Bmatrix} m_1 \\ 0 \\ 0 \end{Bmatrix}$$

where,

$$\begin{aligned} f_2 &= -(C^n_{L_0} + C^n_{L_\delta}\delta^n)V^n_T V^n_{a_3} + C^n_{L_\alpha}(V^n_{a_3} + \lambda^n_0)^2 - C^n_{D_0} V^n_T V^n_{a_2} \\ f_3 &= (C^n_{L_0} + C^n_{L_\delta}\delta^n)V^n_T V^n_{a_2} - C^n_{L_\alpha}\dot{V}^n_{a_3}\frac{c^n}{4} - C^n_{L_\alpha} V^n_{a_2}(V^n_{a_3} + \lambda^n_0 - \Omega^n_{a_1}\frac{c^n}{4}) - C^n_{D_0} V^n_T V^n_{a_3} \\ m_1 &= (C^n_{m_0} + C^n_{m_\delta}\delta^n)V^{n2}_T - C^n_{m_\alpha} V^n_T V^n_{a_3} - \frac{c^n}{2}\left(\frac{C^n_{L_\alpha}}{8} + \frac{C^n_{pitch}}{2}\right) V^n_{a2}\Omega^n_{a_1} - c^{n2} C^n_{L_\alpha}\frac{\dot{\Omega}^n_{a_1}}{128} \\ &\quad + c^n C^n_{L_\alpha}\frac{\dot{V}^n_{a_3}}{32} \end{aligned} \tag{3.60}$$

$\mathbf{V}^n_a$ represents the velocity components at the mid-chord of the n^{th} element. λ^n_0 represents the downwash due to free vorticity for the n^{th} element and is computed using an inflow model. The velocity components at the mid-chord are computed as,

$$\begin{aligned} \mathbf{V}^n_a &= \mathcal{C}^{n^T}_a \overline{\mathbf{V}}^n - \mathbf{y}_{mc} \times \mathcal{C}^{n^T}_a \overline{\mathbf{\Omega}}^n \\ \mathbf{\Omega}^n_a &= \mathcal{C}^{n^T}_a \overline{\mathbf{\Omega}}^n \\ V^n_T &= \sqrt{V^2_{a_2} + V^2_{a_3}} \end{aligned} \tag{3.61}$$

where $\mathcal{C}^n_a$ represents the rotation matrix from the local aerodynamic to the local structural axis system. These forces and moments are re-written in the beam reference axes as,

$$\begin{aligned} \overline{\mathbf{f}}^n_{\text{aero}} &= \mathcal{C}^n_a \mathbf{f}^n_{\text{aero}} \\ \overline{\mathbf{m}}^n_{\text{aero}} &= \mathcal{C}^n_a \mathbf{m}^n_{\text{aero}} + \mathcal{C}^n_a \widetilde{\mathbf{y}}^n_{ac} \mathbf{f}^n_{\text{aero}} \end{aligned} \tag{3.62}$$

The inflow λ^n_0 in Eq. (3.60) is computed using Peters 2D inflow model [80]:

$$[\mathcal{A}_{inflow}]\{\dot{\lambda}^n\} + \left(\frac{2V^n_T}{c^n}\right)\{\lambda^n\} = \left(-\dot{V}^n_{a_3} + \frac{c^n}{4}\dot{\Omega}^n_{a_1}\right)\{\mathbf{c}_{inflow}\} \tag{3.63}$$

$$\lambda^n_0 = \frac{1}{2}\{\mathbf{b}_{inflow}\}^T\{\lambda^n\} \tag{3.64}$$

where the coefficients are constant matrices derived in Ref. [80]. Six states are used in the vector λ^n for the n^{th} element, and the vector $\mathbf{b}_{inflow}$ is computed using an augmented least-squares expansion.

3.4 Aeroelastic Equations

The final equations in discretized form are a collection of equations presented above. These consist of the primary equations for each element Eqs. (3.43)-(3.46) and Eq. (3.51), the equations at each node Eqs. (3.54)-(3.55) and the equations for unsteady aerodynamics Eq. (3.63).

The following boundary conditions complete the set of equations required to analyze the free-flying aircraft problem as formulated above:

$$\widehat{\mathbf{F}}_l^1 = 0 \tag{3.65}$$

$$\widehat{\mathbf{M}}_l^1 = 0 \tag{3.66}$$

$$\widehat{\mathbf{F}}_r^{N+1} = 0 \tag{3.67}$$

$$\widehat{\mathbf{M}}_r^{N+1} = 0 \tag{3.68}$$

$$(\mathbf{e}_1\mathbf{e}_1^T + \mathbf{e}_2\mathbf{e}_2^T)\dot{\widehat{\mathbf{g}}}^{n_g} + (\mathbf{e}_1\mathbf{e}_1^T + \mathbf{e}_2\mathbf{e}_2^T)\widetilde{\widehat{\boldsymbol{\Omega}}^{n_g}}\widehat{\mathbf{g}}^{n_g} + e_3(|\widehat{\mathbf{g}}^{n_g}| - g_0) = 0 \tag{3.69}$$

N denotes the total number of elements and n_g denotes the reference node for gravity.

3.5 Open-loop Trim Computation and Linear Stability Analysis

The trim state of the system is specified in terms of the flight speed, the flight path angle, and the rate of turn in the inertial frame. Sideslip is constrained to be zero. The

corresponding equations for specifying these quantities are given by,

$$V_1^{n_g 2} + V_2^{n_g 2} + V_3^{n_g 2} - V_\infty^2 = 0 \tag{3.70}$$

$$\mathbf{\Omega}_r^{n_g}.(\mathbf{g}_r^{n_g}/g_0) - r_i = 0 \tag{3.71}$$

$$V_1^{n_g} g_1^{n_g} + V_2^{n_g} g_2^{n_g} + V_3^{n_g} g_3^{n_g} + V_\infty g_0 \sin\gamma = 0 \tag{3.72}$$

$$V_1^{n_g} = 0 \tag{3.73}$$

The set of equations presented in Section (3.4) along with the four constraint equations present above constitute a set of non-linear equations in the state variables ($\widehat{\mathbf{V}}_r^n$, $\widehat{\mathbf{\Omega}}_r^n$, $\widehat{\mathbf{F}}_l^n$, $\widehat{\mathbf{F}}_r^n$, $\widehat{\mathbf{M}}_l^n$, $\widehat{\mathbf{M}}_r^n$, $\widehat{\mathbf{g}}_r^n$, $n = 1 \ldots N+1$) from the structural model, (λ^n, $n = 1 \ldots N$) from the unsteady aerodynamic model, and thrust, flap, aileron deflection and differential thrust corresponding to the trim point. These non-linear equations are solved using the Newton-Raphson method to compute the trim point, in terms of the thrust T, flap δ_f, aileron deflection δ_a and the differential thrust ΔT. Following trim computation, the equations are linearized at the trim point. Linear stability analysis is carried out by computing the eigenvalues of the system. These eigenvalues indicate the stability of the system for small perturbations about the trim point.

To identify the effect of static aeroelastic deformation on the flight dynamics, the curvature of the flying wing at trim is used to define the shape of an equivalent rigid flying wing. Flight dynamic eigenvalues for the equivalent rigid configuration are computed and compared with those of the complete flight dynamic/aeroelastic system.

3.6 Non-dimensional form and aeroelastic parameters

Eqs. (3.1)-(3.2) are non-dimensionalized to obtain parameters that determine the interaction of aeroelasticity with flight dynamics. The first equation is divided by $\overline{q}c$ and the

second equation is divided by $\overline{q}c^2$ to re-write the equations as

$$\frac{\partial \mathcal{F}}{\partial \zeta}\left(\frac{l}{c}\right) + (\widetilde{k}l + \widetilde{\kappa}l)\mathcal{F}\left(\frac{l}{c}\right) + \mathbf{C}_F + \left(\frac{\mu g}{\overline{q}c}\right) = \frac{\partial \mathcal{P}}{\partial \tau} + \widetilde{\omega}\mathcal{P} \tag{3.74}$$

$$\frac{\partial \mathcal{M}}{\partial \zeta}\left(\frac{l}{c}\right)^2 + (\widetilde{k}l + \widetilde{\kappa}l)\mathcal{M}\left(\frac{l}{c}\right)^2 + (\widetilde{e_1} + \widetilde{\epsilon})\mathcal{F}\left(\frac{l}{c}\right)^2 + \mathbf{C}_M + \left(\frac{\mu\widetilde{\xi}g}{\overline{q}c^2}\right) = \frac{\partial \mathcal{H}}{\partial \tau} + \widetilde{\omega}\mathcal{H} + \widetilde{\mathcal{V}}\mathcal{P} \tag{3.75}$$

where, $\mathcal{F} = \mathbf{F}/\overline{q}l^2$, $\mathcal{M} = \mathbf{M}/\overline{q}l^3$, $\mathcal{P} = \mathbf{P}V_\infty/\overline{q}c^2$, $\mathcal{H} = \mathbf{H}V_\infty/\overline{q}c^3$, $\zeta = x/l$, $\tau = tV_\infty/c$, $\omega = \mathbf{\Omega}c/V_\infty$, $\mathcal{V} = \mathbf{V}/V_\infty$.

The nondimensional forms of Eqs. (3.7)-(3.9) are given by,

$$\begin{Bmatrix} \epsilon \\ \kappa l \end{Bmatrix} = \begin{bmatrix} (\overline{q}l^2)\mathcal{R} & (\overline{q}l^3)\mathcal{S} \\ (\overline{q}l^3)\mathcal{S}^T & (\overline{q}l^4)\mathcal{T} \end{bmatrix} \begin{Bmatrix} \mathcal{F} \\ \mathcal{M} \end{Bmatrix} \tag{3.76}$$

$$\begin{Bmatrix} \mathcal{P} \\ \mathcal{H} \end{Bmatrix} = \begin{bmatrix} 2\mathbb{I}(\mu/\rho c^2) & -2(\mu/\rho c^2)(\widetilde{\xi}/c) \\ 2(\mu/\rho c^2)(\widetilde{\xi}/c) & 2(\mathcal{I}/\rho c^4) \end{bmatrix} \begin{Bmatrix} \mathcal{V} \\ \omega \end{Bmatrix} \tag{3.77}$$

The matrices $\mathcal{R}$ and $\mathcal{S}$ in Eqs. (3.76)-(3.77) are set to zero as the average shear strain across the cross section is negligible and the average normal strain is negligible. If the structural axis system coincides with the beam principal axis, the matrix $\mathcal{T}$ is diagonal with elements $[1/GJ, 1/(EI)_y, 1/(EI)_z]$. When non-dimensionalized as $(\overline{q}l^4)\mathcal{T}$, the diagonal elements consist of the aeroelastic parameters $\{\overline{q}l^4/GJ, \overline{q}l^4/(EI)_y, \overline{q}l^4/(EI)_z\}$. These parameters, along with elements of square matrix in Eq. (3.77), can be used as a metric to quantify static aeroelastic deformation at trim. Similar parameters were defined to ensure aeroelastic similitude while predicting free-flight and flutter characteristics of airplanes from flexible test models [82].

Chapter 4

Control System Design

4.1 Overview

The objective of the control system is to track a pre-defined trajectory on the ground while maintaining a specified flight speed and altitude. This is accomplished by a combination of a non-linear guidance algorithm [83] and a multi-loop dynamic inversion controller [84, 85] applied to the equations of motion of the flexible airplane written in the mean axis system. The use of the mean axis system to write the equations of motion eliminates the coupling between the rigid body modes and the structural dynamics of the deformed airplane [9], resulting in a reduced-order system with only six degrees-of-freedom. The effect of static aeroelastic deformation on the flight dynamics, which will be shown to be significant in the next chapter, is accounted for by recalculating the center-of-gravity and the total moment-of-inertia of the airplane at every time instant. Dynamic inversion applied to this six degree-of-freedom reduced-order model of the statically deformed airplane cancels out the nonlinear flight dynamics and replaces it with prescribed dynamics.

4.2 Mean Axis Model

The concept of the mean axis was used by Milne to study the dynamics of a deformable airplane by assuming small deformation[9]. The mean axis system is defined as a system with respect to which the motion due to deformation has zero linear and angular momentum. If small deformation is assumed, this use of the mean axis system decouples the equations for flight dynamics from the equations for structural dynamics. In the following sections, the equations for flight dynamics are derived in the mean axis for a generic discretized model *without* making a small deformation assumption, and the corresponding mean axes parameters are computed from the aeroelastic state vector for the flying wing.

4.2.1 Equations of Motion

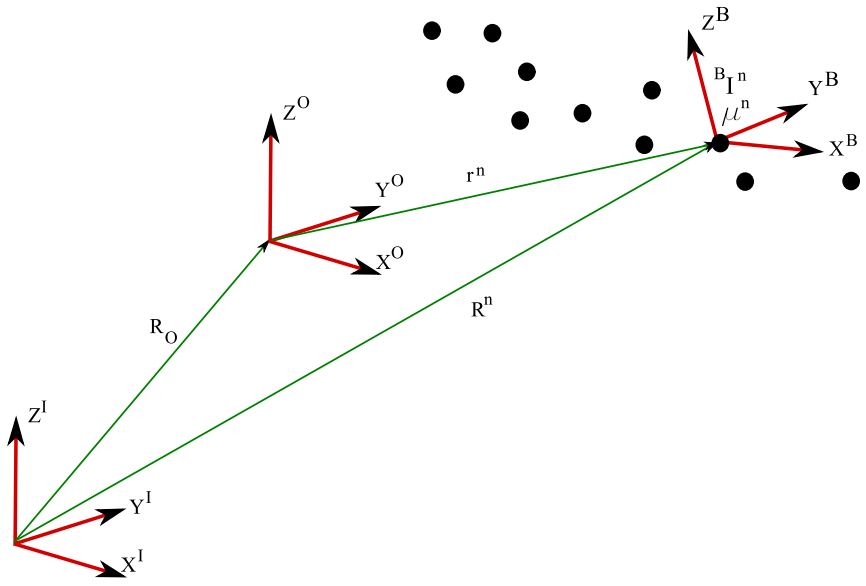

Figure 4.1: Axis system

Consider a set of infinitesimal rigid bodies each with its associated local reference frame B as shown in Fig. 4.1. Represent the mass of the n^{th} body by μ^n and the moment of inertia matrix in the local frame by ${}^B\mathcal{I}^n$. The corresponding velocity vector is represented

in the local frame by ${}^{B}\mathbf{V}^{n}$, and the angular velocity of the rigid body by ${}^{B}\mathbf{\Omega}^{n}$. Represent the forces and moments acting on each rigid body in the local frame by ${}^{B}\mathbf{f}^{n}$ and ${}^{B}\mathbf{m}^{n}$ respectively. Define a non-inertial reference frame O whose origin is at a distance $\mathbf{R}_O$ from the origin of the inertial reference frame I. The position of the the n^{th} body in the O frame is represented by $\mathbf{r}^n$, and in the inertial frame by $\mathbf{R}^n$. These three vectors are now related by,

$$\mathbf{R}^n = \mathbf{R}_O + \mathbf{r}^n$$

The total linear momentum of the set of bodies in the O frame is now given by,

$${}^{O}\mathbf{P} = \sum \mu^n \frac{d}{dt}\bigg|_I {}^{O}\mathbf{R}^n = \sum \mu^n \mathcal{C}^{OB^n} {}^{B}\mathbf{V}^n \tag{4.1}$$

which can also be written as,

$$\begin{aligned} {}^{O}\mathbf{P} &= \sum \mu^n \frac{d}{dt}\bigg|_I ({}^{O}\mathbf{R}_O + {}^{O}\mathbf{r}^n) \\ &= \sum \mu^n \frac{d}{dt}\bigg|_I {}^{O}\mathbf{R}_O + \sum \mu^n \frac{d}{dt}\bigg|_I {}^{O}\mathbf{r}^n \\ &= M_{total}\, {}^{O}\mathbf{V}_O + \sum \mu^n \frac{d}{dt}\bigg|_I {}^{O}\mathbf{r}^n \end{aligned} \tag{4.2}$$

where M_{total} is the total mass of the system and ${}^{O}\mathbf{V}_O$ represents the velocity of the origin of the O frame. Representing the position of the center of gravity of the set of bodies in the O frame by ${}^{O}\xi_O$, the following relation can be obtained.

$$\sum \mu^n \frac{d}{dt}\bigg|_I {}^{O}\mathbf{r}^n = \frac{d}{dt}\bigg|_I \sum \mu^n {}^{O}\mathbf{r}^n = \frac{d}{dt}\bigg|_I M_{total}\, {}^{O}\xi_O$$

Eq. (4.2) can now be written as

$${}^{O}\mathbf{P} = M_{total}\, {}^{O}\mathbf{V}_O + M_{total}\, {}^{O}\dot{\xi}_O + {}^{O}\mathbf{\Omega}_O \times M_{total}\, {}^{O}\xi_O \tag{4.3}$$

The expression for the total angular momentum in the O frame is given by,

$$\begin{aligned} {}^{O}\mathbf{H}_{O} &= \sum {}^{O}\mathbf{r}^{n} \times \mu^{n} \frac{d}{dt}\bigg|_{I} {}^{O}\mathbf{R}^{n} + \sum \mathcal{C}^{OB^{n}B} \mathcal{I}^{nB} \mathbf{\Omega}^{n} \\ &= \sum {}^{O}\mathbf{r}^{n} \times \mu^{n} \mathcal{C}^{OB^{n}B} \mathbf{V}^{n} + \sum \mathcal{C}^{OB^{n}B} \mathcal{I}^{nB} \mathbf{\Omega}^{n} \end{aligned} \tag{4.4}$$

An alternate expression for the angular momentum is given by,

$$\begin{aligned} {}^{O}\mathbf{H}_{O} &= \sum {}^{O}\mathbf{r}^{n} \times \mu^{n} \frac{d}{dt}\bigg|_{I} ({}^{O}\mathbf{R}_{O} + {}^{O}\mathbf{r}^{n}) + \sum \mathcal{C}^{OB^{n}B} \mathcal{I}^{nB} \mathbf{\Omega}^{n} \\ &= \sum \mu^{n} {}^{O}\mathbf{r}^{n} \times \frac{d}{dt}\bigg|_{I} {}^{O}\mathbf{R}_{O} + \sum {}^{O}\mathbf{r}^{n} \times \mu^{n} \frac{d}{dt}\bigg|_{I} {}^{O}\mathbf{r}^{n} + \sum \mathcal{C}^{OB^{n}B} \mathcal{I}^{nB} \mathbf{\Omega}^{n} \\ &= M_{total} {}^{O}\xi_{O} \times {}^{O}\mathbf{V}_{O} + \sum {}^{O}\mathbf{r}^{n} \times \mu^{n} \frac{d}{dt}\bigg|_{O} {}^{O}\mathbf{r}^{n} + \sum {}^{O}\mathbf{r}^{n} \times \mu^{n} ({}^{O}\mathbf{\Omega}_{O} \times {}^{O}\mathbf{r}^{n}) \\ &\quad + \sum \mathcal{C}^{OB^{n}B} \mathcal{I}^{nB} \mathbf{\Omega}^{n} \\ &= M_{total} {}^{O}\xi_{O} \times {}^{O}\mathbf{V}_{O} + \sum {}^{O}\mathbf{r}^{n} \times \mu^{n} \frac{d}{dt}\bigg|_{O} {}^{O}\mathbf{r}^{n} + {}^{O}\mathcal{I}_{O} {}^{O}\mathbf{\Omega}_{O} \\ &\quad + \sum \mathcal{C}^{OB^{n}B} \mathcal{I}^{nB} \mathbf{\Omega}^{n} \end{aligned} \tag{4.5}$$

where the inertia matrix $\mathcal{I}_O$ is given by

$${}^{O}\mathcal{I}_{O} = \sum \mu^{n} \left(({}^{O}\mathbf{r}^{n} \cdot {}^{O}\mathbf{r}^{n}) \mathbb{I} - {}^{O}\mathbf{r}^{n} {}^{O}\mathbf{r}^{n} \right) \tag{4.6}$$

The rate of change of linear momentum is given by,

$$\frac{d}{dt}\bigg|_{I} {}^{O}\mathbf{P} = \sum \mu^{n} \frac{d^{2}}{dt^{2}}\bigg|_{I} {}^{O}\mathbf{R}^{n} = \sum \mathcal{C}^{OB^{n}B} \mathbf{f}^{n} \tag{4.7}$$

An alternate expression is given by,

$$\begin{aligned} \frac{d}{dt}\bigg|_{I} {}^{O}\mathbf{P} &= \frac{d}{dt}\bigg|_{O} {}^{O}\mathbf{P} + {}^{O}\mathbf{\Omega}_{O} \times {}^{O}\mathbf{P} \\ &= M_{total} {}^{O}\dot{\mathbf{V}}_{O} + M_{total} {}^{O}\ddot{\xi}_{O} + {}^{O}\dot{\mathbf{\Omega}}_{O} \times M_{total} {}^{O}\xi_{O} + {}^{O}\mathbf{\Omega}_{O} \times M_{total} {}^{O}\dot{\xi}_{O} \\ &\quad + {}^{O}\mathbf{\Omega}_{O} \times {}^{O}\mathbf{P} \end{aligned} \tag{4.8}$$

The rate of change of angular momentum is given by,

$$\begin{aligned}
\frac{d}{dt}\bigg|_I {}^O\mathbf{H}_O &= \sum \frac{d}{dt}\bigg|_I {}^O\mathbf{r}^n \times \mu^n \frac{d}{dt}\bigg|_I {}^O\mathbf{R}^n + \sum {}^O\mathbf{r}^n \times \mu^n \frac{d^2}{dt^2}\bigg|_I {}^O\mathbf{R}^n \\
&\quad + \sum \mathcal{C}^{OB^n} \frac{d}{dt}\bigg|_I {}^B\mathcal{I}^{nB}\boldsymbol{\Omega}^n \\
&= \sum \frac{d}{dt}\bigg|_I \left({}^O\mathbf{R}^n - {}^O\mathbf{R}_O\right) \times \mu^n \frac{d}{dt}\bigg|_I {}^O\mathbf{R}^n + \sum {}^O\mathbf{r}^n \times \mathcal{C}^{OB^nB}\mathbf{f}^n \\
&\quad + \sum \mathcal{C}^{OB^nB}\mathbf{m}^n \\
&= -\frac{d}{dt}\bigg|_I {}^O\mathbf{R}_O \times \sum \mu^n \frac{d}{dt}\bigg|_I {}^O\mathbf{R}^n + \sum {}^O\mathbf{r}^n \times \mathcal{C}^{OB^nB}\mathbf{f}^n + \sum \mathcal{C}^{OB^nB}\mathbf{m}^n \\
&= -{}^O\mathbf{V}_O \times {}^O\mathbf{P} + \sum {}^O\mathbf{r}^n \times \mathcal{C}^{OB^nB}\mathbf{f}^n + \sum \mathcal{C}^{OB^nB}\mathbf{m}^n \qquad (4.9)
\end{aligned}$$

An alternate expression is given by,

$$\begin{aligned}
\frac{d}{dt}\bigg|_I {}^O\mathbf{H}_O &= \frac{d}{dt}\bigg|_O {}^O\mathbf{H}_O + {}^O\boldsymbol{\Omega}_O \times {}^O\mathbf{H}_O \\
&= M_{total}{}^O\dot{\xi}_O \times {}^O\mathbf{V}_O + M_{total}{}^O\xi_O \times {}^O\dot{\mathbf{V}}_O + \sum {}^O\mathbf{r}^n \times \mu^n \frac{d^2}{dt^2}\bigg|_O {}^O\mathbf{r}^n \\
&\quad + \sum \left({}^O\dot{\mathbf{r}}^n \times \mu^n({}^O\boldsymbol{\Omega}_O \times {}^O\mathbf{r}^n) + {}^O\mathbf{r}^n \times \mu^n({}^O\boldsymbol{\Omega}_O \times {}^O\dot{\mathbf{r}}^n)\right) \\
&\quad + \sum {}^O\mathbf{r}^n \times \mu^n({}^O\dot{\boldsymbol{\Omega}}_O \times {}^O\mathbf{r}^n) + \sum \mathcal{C}^{OB^nB}\mathcal{I}^{nB}\dot{\boldsymbol{\Omega}}^n + {}^O\boldsymbol{\Omega}_O \times {}^O\mathbf{H}_O \\
&= M_{total}{}^O\dot{\xi}_O \times {}^O\mathbf{V}_O + M_{total}{}^O\xi_O \times {}^O\dot{\mathbf{V}}_O + \sum {}^O\mathbf{r}^n \times \mu^n \frac{d^2}{dt^2}\bigg|_O {}^O\mathbf{r}^n \\
&\quad + {}^O\dot{\mathcal{I}}_O{}^O\boldsymbol{\Omega}_O + {}^O\mathcal{I}_O{}^O\dot{\boldsymbol{\Omega}}_O + {}^O\boldsymbol{\Omega}_O \times {}^O\mathbf{H}_O \\
&\quad + \sum \mathcal{C}^{OB^nB}\mathcal{I}^{nB}\dot{\boldsymbol{\Omega}}^n + \sum \dot{\mathcal{C}}^{OB^nB}\mathcal{I}^{nB}\boldsymbol{\Omega}^n \qquad (4.10)
\end{aligned}$$

where

$$\begin{aligned}
{}^O\dot{\mathcal{I}}_O &= \sum \mu^n \left(2\left({}^O\mathbf{r}^n \cdot {}^O\dot{\mathbf{r}}^n\right)\mathbb{I} - {}^O\mathbf{r}^n{}^O\dot{\mathbf{r}}^n - {}^O\dot{\mathbf{r}}^n{}^O\mathbf{r}^n\right) \qquad (4.11) \\
\dot{\mathcal{C}}^{OB^n} &= \mathcal{C}^{OB^nB}\widetilde{\boldsymbol{\Omega}}^n - {}^O\widetilde{\boldsymbol{\Omega}}_O\mathcal{C}^{OB^n} \qquad (4.12)
\end{aligned}$$

The expression for $\dot{\mathcal{C}}^{OB^n}$ is obtained from Ref. [77].

Now place the origin of the frame O at the center of gravity of the system. The subscript O on the right-hand side of velocity, moment-of-inertia and angular momentum is now changed to cg to denote the shift of origin to the center of gravity. This sets the vector ${}^{O}\xi_{O}$ and the corresponding rate term to zero. Eqs. (4.1) and (4.3) now give the expression for velocity of the center of gravity as,

$$ {}^{O}\mathbf{V}_{cg} = \frac{1}{M_{total}} \sum \mu^{n} \mathcal{C}^{OB^{n}B} \mathbf{V}^{n} \tag{4.13} $$

This prescribes the translational velocity of the origin of the O frame. Placing the origin of the O frame at the center-of-gravity of the system ensures that the linear momentum due to deformation is zero in the O frame.

Eqs. (4.4) and (4.5) when equated can be used to obtain multiple solutions to the angular velocity ${}^{O}\mathbf{\Omega}_{O}$. Choosing the angular velocity of the O frame to be,

$$ {}^{O}\mathbf{\Omega}_{M} = {}^{O}\mathcal{I}_{cg}^{-1} \sum {}^{O}\mathbf{r}^{n} \times \mu^{n} \mathcal{C}^{OB^{n}B} \mathbf{V}^{n} \tag{4.14} $$

implies,

$$ \sum {}^{O}\mathbf{r}^{n} \times \mu^{n} \frac{d}{dt}\bigg|_{O} {}^{O}\mathbf{r}^{n} = 0 $$

This choice of angular velocity of the O frame ensures that the deformation motion has zero angular momentum in the O frame. If the linear and angular velocity of the O frame are calculated as shown in Eqs. (4.13) and (4.14) respectively, the axis system O corresponds to the mean axis system M [9].

Eqs. (4.7) and (4.8) give the force equation as,

$$ M_{total} {}^{O}\dot{\mathbf{V}}_{cg} + {}^{O}\mathbf{\Omega}_{M} \times {}^{O}\mathbf{P} = \sum \mathcal{C}^{OB^{n}B} \mathbf{f}^{n} \tag{4.15} $$

and Eqs. (4.9) and (4.10) give the moment equation as

$$
\begin{aligned}
{}^{O}\mathcal{I}_{cg}\,{}^{O}\dot{\mathbf{\Omega}}_{M} + {}^{O}\dot{\mathcal{I}}_{cg}\,{}^{O}\mathbf{\Omega}_{M} + {}^{O}\mathbf{\Omega}_{M} \times {}^{O}\mathbf{H}_{cg} = \sum {}^{O}\mathbf{r}^{n} \times \mathcal{C}^{OB^{n}B}\mathbf{f}^{n} + \sum \mathcal{C}^{OB^{n}B}\mathbf{m}^{n} \\
- \sum \mathcal{C}^{OB^{n}B}\mathcal{I}^{nB}\dot{\mathbf{\Omega}}^{n} - \sum \dot{\mathcal{C}}^{OB^{n}B}\mathcal{I}^{nB}\mathbf{\Omega}^{n}
\end{aligned} \tag{4.16}
$$

where ${}^{O}\mathbf{P}$ and ${}^{O}\mathbf{H}_{cg}$ are calculated as shown in Eq. (4.1) and (4.4) respectively.

Eqs. (4.15)-(4.16) represent the equations of motion of the mean axis system with its origin at the center-of-mass of the system of bodies. If the relative position of the rigid bodies does not vary significantly, ${}^{O}\dot{\mathcal{I}}_{cg}$ can be approximated to be equal to zero. If the system of rigid bodies is taken to be a finite-state representation of a flexible body, Eqs. (4.15)-(4.16) represent the flight dynamics equations that are decoupled from the equations for structural dynamics under the small-deformation assumption. However, it is important to note that these equations are not completely decoupled due to the coupling through aerodynamic forces and moments.

4.2.2 Application to current problem

Calculation of the mean axis parameters for the flying wing problem are carried out in the root axis system R whose origin is at the center of the airplane on the beam X axis. The forces and moments acting on each element, and the corresponding masses and moments of inertia are split into two equal halves and lumped at the nodes on the ends of each element. The expressions for these quantities are given by,

$$
\begin{aligned}
\mu^{n} &= \frac{\overline{\mu}^{n} dl}{2} + \frac{\overline{\mu}^{n-1} dl}{2} + \widehat{\mu}^{n} \\
{}^{B}\xi_{B}^{n} &= \frac{1}{\mu^{n}} \left(\frac{\overline{\mu}^{n} dl \overline{\xi}^{n}}{2} + \frac{\overline{\mu}^{n-1} dl \mathcal{C}_{lr}^{n^{T}} \overline{\xi}^{n-1}}{2} + \widehat{\mu}^{n} \widehat{\xi}^{n} \right) \\
{}^{B}\mathcal{I}^{n} &= \frac{\overline{\mathcal{I}}^{n} dl}{2} + \frac{\mathcal{C}_{lr}^{n^{T}} \overline{\mathcal{I}}^{n-1} \mathcal{C}_{lr}^{n} dl}{2} + \widehat{\mathcal{I}}^{n} + \mathcal{I}_{\mu}{}^{n} + \mathcal{C}_{lr}^{n^{T}} \mathcal{I}_{\mu}{}^{n-1} \mathcal{C}_{lr}^{n}
\end{aligned}
$$

$$
\begin{aligned}
{}^{B}\mathbf{f}^{n} &= \frac{\overline{\mathbf{f}}^{n}_{aero}dl}{2} + \frac{\mathcal{C}^{n^T}_{lr}\overline{\mathbf{f}}^{n-1}_{aero}dl}{2} + \widehat{\mathbf{f}}^{n}_{T} \\
{}^{B}\mathbf{m}^{n} &= \frac{\overline{\mathbf{m}}^{n}_{aero}dl}{2} + \frac{\mathcal{C}^{n^T}_{lr}\overline{\mathbf{m}}^{n-1}_{aero}dl}{2} + \widehat{\mathbf{m}}^{n}_{T} \\
\mathcal{I}_{\mu}{}^{n} &= \overline{\mu}^{n}\begin{bmatrix} \overline{\xi}^{n^2}dl/2 & -\overline{\xi}^{n}dl^2/8 & 0 \\ -\overline{\xi}^{n}dl^2/8 & dl^3/24 & 0 \\ 0 & 0 & (dl^3/24) + (\overline{\xi}^{n^2}dl/2) \end{bmatrix}
\end{aligned}
$$

where ${}^{B}\xi_{B}$ is position of center-of-mass of the total nodal mass.

The aeroelastic state vector contains the nodal velocities and angular velocities at the origin of the local frame B. The velocity at the mass position is given in terms of the nodal velocity and angular velocity as,

$$
\begin{aligned}
{}^{B}\mathbf{V}^{n} &= \widehat{\mathbf{V}}^{n}_{r} + \widehat{\mathbf{\Omega}}^{n}_{r} \times {}^{B}\xi^{n}_{B} \\
{}^{B}\mathbf{\Omega}^{n} &= \widehat{\mathbf{\Omega}}^{n}_{r}
\end{aligned} \tag{4.17}
$$

Eqs. (3.5)-(3.6) can be discretized and used to obtain the nodal positions on the beam axis from the origin of the root frame $\mathbf{r}^{n}_{B}$ and rotations of the deformed beam at the node $\mathcal{C}^{RB^n}$ in terms of the strains and curvatures as,

$$
\mathcal{C}^{BR^{n+1}} = \left(\frac{\Delta}{dl} + \frac{\widetilde{\overline{\kappa}}^{n} + \widetilde{\mathbf{k}}^{n}}{2}\right)^{-1}\left(\frac{\Delta}{dl} - \frac{\widetilde{\overline{\kappa}}^{n} + \widetilde{\mathbf{k}}^{n}}{2}\right)\mathcal{C}^{BR^n} \tag{4.18}
$$

$$
\mathbf{r}^{n+1}_{B} = \mathbf{r}^{n}_{B} + \left(\mathcal{C}^{BR^n} + \mathcal{C}^{n}_{lr}\mathcal{C}^{BR^{n+1}}\right)^{T}(\overline{\epsilon}^{n} + \mathbf{e}_1)dl/2 \tag{4.19}
$$

The above expression can now be used to obtain the position of the total mass at the n^{th} node relative to the center-of-gravity as,

$$
{}^{R}\mathbf{r}^{n} = \mathbf{r}^{n}_{B} + \mathcal{C}^{RB^n}{}^{B}\xi^{n}_{B} - {}^{R}\xi_{cg} \tag{4.20}
$$

It is to be noted that Eq. (4.16) which is the moment equation acting on the total airplane

uses $\left(\mathbf{r}_B^n - {}^R\xi_{cg}\right)$, as the total moment acting at the node ${}^B\mathbf{m}^n$ is calculated at the origin at the local frame. All other expressions for ${}^O\mathbf{r}^n$ in section 4.2.1 are to be substituted by ${}^R\mathbf{r}^n$.

4.2.3 Kinematic Equations

For designing the control system, three axis systems are necessary. These are the root axis system R, shown in Fig. 3.2, an inertial axis system I with the same arrangement of axes, and the mean axis system M. The relative orientation of both the mean and the root axis system relative to the inertial axis system is defined using a $3-1-2$ Euler angle rotation sequence. The corresponding rotation matrices are given below for reference:

$$\mathcal{C}_3(\psi) = \begin{bmatrix} \cos\psi & \sin\psi & 0 \\ -\sin\psi & \cos\psi & 0 \\ 0 & 0 & 1 \end{bmatrix} \mathcal{C}_1(\theta) = \begin{bmatrix} 1 & 0 & 0 \\ 0 & \cos\theta & \sin\theta \\ 0 & -\sin\theta & \cos\theta \end{bmatrix} \mathcal{C}_2(\phi) = \begin{bmatrix} \cos\phi & 0 & -\sin\phi \\ 0 & 1 & 0 \\ \sin\phi & 0 & \cos\phi \end{bmatrix}$$

The rotation matrices can now be defined as,

$$\begin{aligned} \mathcal{C}^{MI} &= \mathcal{C}_2(\phi_{mi})\mathcal{C}_1(\theta_{mi})\mathcal{C}_3(\psi_{mi}) \\ \mathcal{C}^{RI} &= \mathcal{C}_2(\phi_{ri})\mathcal{C}_1(\theta_{ri})\mathcal{C}_3(\psi_{ri}) \\ \mathcal{C}^{MR} &= \mathcal{C}^{MI}\mathcal{C}^{RI^T} \end{aligned} \tag{4.21}$$

The rate of change of Euler angles is related to the inertial components of the angular velocity vector by,

$$\begin{Bmatrix} \dot{\phi} \\ \dot{\theta} \\ \dot{\psi} \end{Bmatrix} = \begin{bmatrix} -\sin\psi\sec\theta & \cos\psi\sec\theta & 0 \\ \cos\psi & \sin\psi & 0 \\ \sin\psi\tan\theta & -\cos\psi\tan\theta & 1 \end{bmatrix} {}^I\boldsymbol{\Omega} \tag{4.22}$$

The inertial position of the center of gravity is related to the root axis components of velocity by,

$$^{I}\dot{\mathbf{x}}_{cg} = \mathcal{C}^{IRR}\mathbf{V}_{cg} \tag{4.23}$$

4.3 Control System Design

4.3.1 Guidance Algorithm

The nonlinear guidance algorithm used in this dissertation for path following was developed by Park *et al.* [83]. This guidance law was shown to give superior performance as compared to linear guidance laws in following curved paths. This is due to its ability to calculate the required lateral acceleration based on the commanded path ahead of the current vehicle position, and the use of the inertial velocity in calculating the acceleration to compensate for external disturbances such as wind [83].

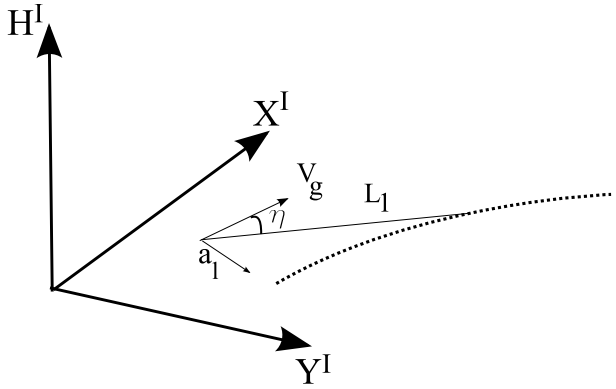

Figure 4.2: Guidance Algorithm

Consider a trajectory defined by a sequence of points in the inertial frame as shown in Fig. 4.2. Denote the current inertial co-ordinates of the airplane by (x,y,h). Select a reference point on the trajectory at a specified distance L_1 ahead of the current position. Let V_g represent the velocity of the airplane in the X^IY^I plane and η represent the angle

between the velocity vector and the line to the reference point. The guidance algorithm gives the demanded lateral acceleration as [83],

$$a_l^d = 2\frac{{V_g}^2}{L_1}\sin\eta \tag{4.24}$$

The lookforward distance L_1 also gives a lower bound on the radius of the circular ground path that can be followed as $L_1/2$ [83].

4.3.2 Review of Dynamic Inversion

Theoretical Foundations

Application of linear control theory to non-linear problems requires the system to be linearized at multiple operating points. Controllers designed at each operating point using linear control theory can then be combined by specifying the gains as function of the operating point (gain-scheduling algorithms). However, gain-scheduling can be tedious and may be impossible to implement if nonlinearities are present in multiple variables. On the other hand, dynamic inversion controllers work by canceling the inherent dynamics of selected control variables (CVs) over the entire domain and replacing them with desired dynamics [86].

Consider a system whose dynamics can be represented in the form,

$$\dot{\mathbf{x}} = \mathbf{f}(\mathbf{x}) + \mathbf{g}(\mathbf{x})\mathbf{u} \tag{4.25}$$

where $\mathbf{x} \in \mathbb{R}^n$ represents the state vector and $\mathbf{u} \in \mathbb{R}^m$ represents the control vector. Let the vector of CVs be given by,

$$\mathbf{y} = \mathbf{h}(\mathbf{x}) \tag{4.26}$$

where, $\mathbf{y} \in \mathbb{R}^k$.

The rate of change of CVs is given by,

$$\begin{aligned} \dot{\mathbf{y}} &= \frac{d\mathbf{h}}{d\mathbf{x}}\dot{\mathbf{x}} = \frac{d\mathbf{h}}{d\mathbf{x}}(\mathbf{f}(\mathbf{x}) + \mathbf{g}(\mathbf{x})\mathbf{u}) \\ &= \mathbf{F}(\mathbf{x}) + \mathbf{G}(\mathbf{x})\mathbf{u} \end{aligned} \tag{4.27}$$

$\mathbf{G}(\mathbf{x})$ is invertible if the number of CVs is equal to the number of states in the control input $\mathbf{u}$. Now, if $\mathbf{G}(\mathbf{x})$ is invertible, select the vector of control inputs $\mathbf{u}$ such that,

$$\mathbf{u} = \mathbf{G}^{-1}(\dot{\mathbf{y}}^{des} - \mathbf{F}(\mathbf{x})) \tag{4.28}$$

where $\dot{\mathbf{y}}^{des}$ represents the desired dynamics of the CVs. The control inputs give us the desired dynamics. The CVs have to be selected and the desired dynamics of the CVs' have to be specified as part of the control design process.

The choice of CVs is critical to the performance of the dynamic inversion controller. The dynamics of the states which are not controlled by the control input defined in Eq. (4.28) are known as *zero dynamics*. For the closed loop system to give the desired performance, CVs have to be selected such that the zero dynamics are stable [87].

A fundamental assumption in dynamic inversion is that Eqs. (4.25)-(4.26) represent the dynamics of the system exactly [88]. Uncertainty in the model will have to be accounted for by using robust control design techniques. In general, dynamic inversion controllers do not require a gain scheduling algorithm. Exceptions to this occur when commanded control inputs are large enough to cause actuator saturation [88].

Method of Multiple Time-Scales

Flight dynamics for a conventional rigid airplane configuration are modeled by a set of eight first order differential equations. The state vector $\mathbf{x}$ consists of velocity V, flight

path angle γ, angle of attack α, side-slip angle β, body-axis roll angle ϕ, body-axis roll rate p, body-axis pitch rate q and body-axis yaw rate r. The control vector $\mathbf{u}$ consists of thrust T, and control surface deflections $\delta_e, \delta_a, \delta_r$ for elevator, aileron and rudder respectively. If the CV vector $\mathbf{y}$ in Eq. (4.26) is taken to be the state vector $\mathbf{x}$, then the system is required to have as many elements in the control vector $\mathbf{u}$ as there are in the state vector $\mathbf{x}$ for $\mathbf{G}(\mathbf{x})$ to be invertible. Since this is not the case for a typical airplane, a two-step approach has been devised which makes use of the multiple time-scales inherent in the dynamics of the system [84, 85]. Ref. [88, 89] present a good review of Dynamic Inversion as applied to the airplane control problem.

4.3.3 Control Architecture for Flying Wings

The dynamic inversion controller is designed using the force equation given by Eq. (4.15), the moment equation given by Eq. (4.16) and the kinematic equation given below:

$$\begin{Bmatrix} {}^{M}\Omega_{M1} \\ {}^{M}\Omega_{M2} \\ {}^{M}\Omega_{M3} \end{Bmatrix} = \begin{bmatrix} 0 & \cos\phi_{mi} & -\sin\phi_{mi}\cos\theta_{mi} \\ 1 & 0 & \sin\theta_{mi} \\ 0 & \sin\phi_{mi} & \cos\phi_{mi}\cos\theta_{mi} \end{bmatrix} \begin{Bmatrix} \dot{\phi}_{mi} \\ \dot{\theta}_{mi} \\ \dot{\psi}_{mi} \end{Bmatrix} \tag{4.29}$$

Applying the method of multiple time scales, the equations are inverted sequentially, and the output of inversion from one step is fed into the next. This procedure is represented schematically in Fig. 4.3.

The inputs given to the controller are the commanded velocity V_c, commanded altitude h_c and commanded ground path in terms of the inertial $X-Y$ co-ordinates (x_c, y_c). These inputs are used in the first step to compute the demanded lateral acceleration and the commanded flight path angle γ_c. Based on the current position, ground speed and a pre-specified length, the guidance algorithm is used to compute the demanded lateral acceleration. The magnitude of this demanded lateral acceleration is given by Eq. (4.24),

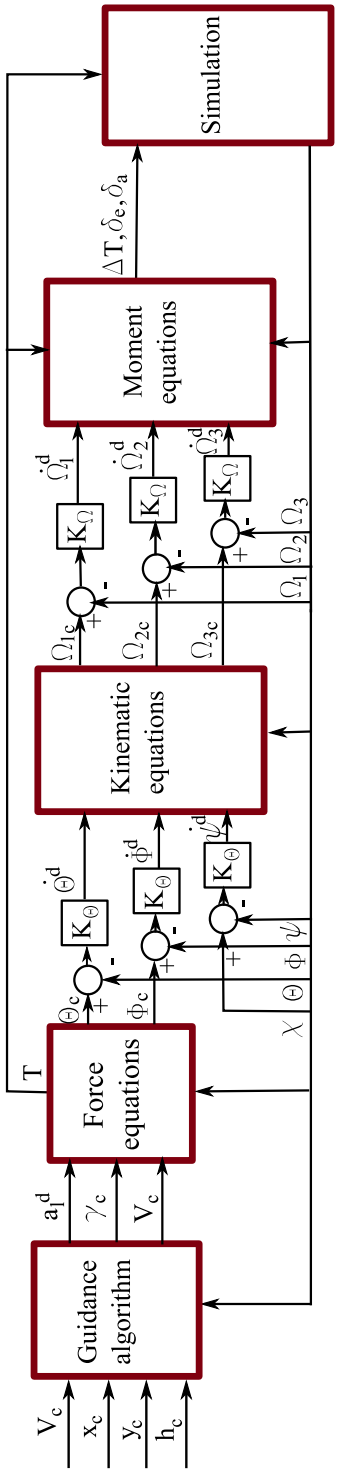

Figure 4.3: Schematic of Control System

and it is oriented in the direction normal to the projection of velocity vector in the inertial $X^I Y^I$ plane as shown in Fig. 4.2. The commanded flight path angle γ_c is calculated as,

$$\gamma_c = \frac{(h_c - h)}{L_h} \tag{4.30}$$

where L_h is the reference length in the $Z^I - V_\infty$ plane. This demanded lateral acceleration is specified in an intermediate frame V which is offset from the inertial frame by a rotation χ about the Z^I axis. The components of the acceleration in the V frame are given by,

$${}^V\mathbf{a}^d = \left\{ \begin{array}{c} a_l^d \\ 0 \\ 0 \end{array} \right\} \tag{4.31}$$

In the second step, the force equations in Eq. (4.15) are inverted to find the magnitude of thrust required and the commanded pitch and roll angles, while holding constant the commanded velocity along the inertial Z axis ($V_c \sin\gamma_c$) and inertial $X - Y$ plane ($V_c \cos\gamma_c$). The accelerations in the mean axis system are given by,

$${}^M\dot{\mathbf{V}}_{cg} + {}^M\widetilde{\mathbf{\Omega}}_M {}^M\mathbf{V}_{cg} = \mathcal{C}^{MV} {}^V\mathbf{a}^d \tag{4.32}$$

where the accelerations ${}^V\mathbf{a}^d$ are computed in the previous step and the rotation matrix $\mathcal{C}^{MV}$ is given by,

$$\mathcal{C}^{MV} = \mathcal{C}_2(\phi_{mi})\mathcal{C}_1(\theta_{mi})\mathcal{C}_3(\psi_{mi} + \chi) \tag{4.33}$$

Eq. (4.15) is non-linear in T, θ and ϕ and is solved using a Newton-Raphson solver to obtain commanded values of thrust T, pitch angle θ_{mi_c} and roll angle ϕ_{mi_c}. In order to solve this set of nonlinear equations, the velocity and angular velocity at any spanwise location has to be expressed as function of $V_c \cos\gamma_c$ and $V_c \sin\gamma_c$ and the angular velocity of the mean axis. This is done using Eqs. (3.45)-(3.46) while setting the rates $\dot{\bar{\epsilon}}^n$ and

$\dot{\overline{\kappa}}^n$ to zero. This is equivalent to assuming that the structure of the flying wing is rigid with its shape being the instantaneous deformed shape, and that aerodynamic forces and moments generated by structural vibrations are ignored. These new velocity and angular velocity values, which correspond to the motion of a deformed, rigid flying wing are used in the controller to compute aerodynamic forces and moments.

In the next step, the demanded roll, pitch and yaw rates are prescribed as,

$$\dot{\phi}^d_{mi} = K_\theta(\phi_{mi_c} - \phi_{mi}) \tag{4.34}$$

$$\dot{\theta}^d_{mi} = K_\theta(\theta_{mi_c} - \theta_{mi}) \tag{4.35}$$

$$\dot{\psi}^d_{mi} = -K_\theta(\chi + \psi_{mi}) \tag{4.36}$$

The dynamics are prescribed such that the controller tries to drive the states to the prescribed values with a time-constant that is inversely proportional to the gain K_θ. These three rates are used to compute the commanded angular velocities ${}^M\mathbf{\Omega}_{Mc}$ using Eq. (4.29).

In the final step, the demanded angular velocity rates are computed as,

$${}^M\dot{\mathbf{\Omega}}^d_M = K_\Omega({}^M\mathbf{\Omega}_{Mc} - {}^M\mathbf{\Omega}_M) \tag{4.37}$$

${}^R\dot{\mathbf{\Omega}}^d_M$ and Eq. (3.46) is used to compute the ${}^B\dot{\mathbf{\Omega}}^n$ term present in Eq. (4.16). Eq. (4.16) is inverted to find the differential thrust required for yaw control, and the required aileron and flap deflections.

4.4 Time-marching Implementation

A set of non-linear equations given by,

$$[\mathcal{M}]\,\dot{\mathbf{x}} = \mathbf{f}(\mathbf{x}) \tag{4.38}$$

can be discretized for time-marching as,

$$[\mathcal{M}]\,\frac{\mathbf{x}^{t+\Delta t}-\mathbf{x}^{t}}{\Delta t}=\mathbf{f}(\alpha\mathbf{x}^{t}+\beta\mathbf{x}^{t+\Delta t}) \tag{4.39}$$

The above set of discretized equations represent a forward-difference scheme for $\alpha = 1, \beta = 0$, a backward-difference scheme for $\alpha = 0, \beta = 1$ and a central-difference scheme for $\alpha = 0.5, \beta = 0.5$. The explicit forward-difference scheme is unstable and first-order accurate, while the implicit backward-difference scheme is first-order accurate and damps out high frequency oscillations. The central difference scheme is implicit, second-order accurate and energy conserving. The energy-conserving nature of the central-difference scheme may cause it to become unstable due to oscillations whose time periods are much smaller than the time-step of the simulation. In addition, the accuracy of these higher order modes is dependent on the spatial discretization of the finite-difference scheme used in this dissertation.

Therefore, time marching is implemented in this dissertation by setting $\alpha = 0.495, \beta = 0.505$ and time step of $\Delta t = 0.02s$. The choice of α and β damps out high frequency oscillations while giving almost second-order accuracy. Given $\mathbf{x}^t$, Eq. (4.39) now represents an implicit, non-linear set of equations in $\mathbf{x}^{t+\Delta t}$, which is solved for using a Newton-Raphson solver.

For the closed-loop system, this time-marching algorithm is implemented at each time-step on two sets of equations. The first set corresponds to the complete aeroelastic model given by Eqs. (3.43)-(3.46), (3.51), (3.54)-(3.55) and (3.63) which has $(21 \times N) + ((N-1) \times m)$ states, where N corresponds to the number of nodes and m corresponds to the number of unsteady aerodynamic states at each element. The second set consists of kinematic equations given by Eq. (4.22) applied to both the root and the mean axis, and Eq. (4.23) applied to the center-of-gravity of the flying wing.

4.5 Overview of Closed-Loop Simulation

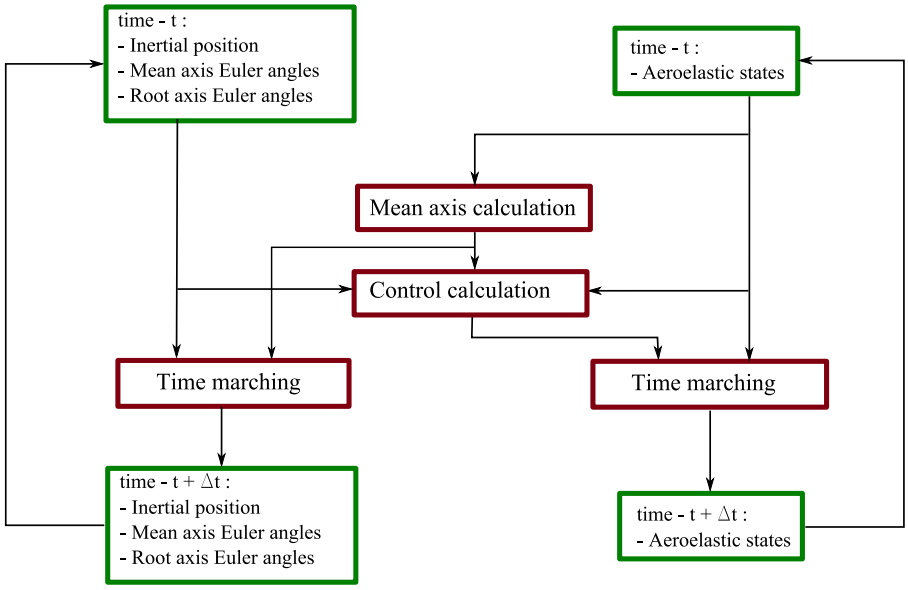

Figure 4.4: Closed-Loop Schematic

The schematic of the closed-loop system is shown in Fig. 4.4. Given a state vector of the complete aeroelastic system at time t, a module computes the velocity, angular velocity, linear and angular momentum, and moment of inertia at that time instant in the mean axis. These values, together with the inertial position and Euler angles, are used to compute the control input to be applied to the system from time t to $t + \Delta t$. The time-marching algorithm described in the previous section is used to compute the aeroelastic state vector at time $t + \Delta t$ using the state vector at the previous time instant and the control input. Concurrently, the velocity of the center of gravity and the angular velocity of the mean axis are used to obtain the inertial co-ordinates and the Euler angles at time $t + \Delta t$.

4.6 State Estimation for Control

The controller design presented in this chapter requires nodal values of velocities $\widehat{\mathbf{V}}_r^n$, angular velocities $\widehat{\mathbf{\Omega}}_r^n$, nodal positions with respect to the origin of the root frame $\mathbf{r}^n$, rotation of the local frame with respect to the root frame $\mathcal{C}^{RB^n}$ and unsteady aerodynamic states λ for load calculation. Nodal positions and rotations of the local frame were computed from the nodal strains and curvatures at each time step as shown in Eqs. (4.18) and (4.19). However, the nodal values of velocity, angular velocity and unsteady aerodynamic states were directly extracted from the aeroelastic state variable at that time instant. As the aeroelastic state vector will not be available when the controller is implemented on a real airplane, unsteady aerodynamic states will have to be simulated on-board using Eq. (3.63) for each element before the loads can be computed. Nodal velocities and angular velocities will have to be calculated in terms of the corresponding values at the wing root using the following expressions obtained by rewriting Eqs. (3.45) and (3.46):

$$\begin{aligned}
\left(\frac{\Delta}{dl}+\frac{\widetilde{\widehat{\kappa}}_l^{n+1}+\widetilde{\mathbf{k}}^n}{2}\right)\mathcal{C}_{lr}^{n+1}\widehat{\mathbf{\Omega}}_r^{n+1} &= \left(\frac{\Delta}{dl}-\frac{\widetilde{\widehat{\kappa}}_r^{n}+\widetilde{\mathbf{k}}^n}{2}\right)\widehat{\mathbf{\Omega}}_r^{n} \\
&\quad +\frac{\dot{\widehat{\kappa}}_l^{n+1}+\dot{\widehat{\kappa}}_r^{n}}{2} \\
\left(\frac{\Delta}{dl}+\frac{\widetilde{\widehat{\kappa}}_l^{n+1}+\widetilde{\mathbf{k}}^n}{2}\right)\mathcal{C}_{lr}^{n+1}\widehat{\mathbf{V}}_r^{n+1}+\frac{\widetilde{\widehat{\epsilon}}_l^{n+1}+\widetilde{\mathbf{e}}_1}{2}\mathcal{C}_{lr}^{n+1}\widehat{\mathbf{\Omega}}_r^{n+1} &= \left(\frac{\Delta}{dl}-\frac{\widetilde{\widehat{\kappa}}_r^{n}+\widetilde{\mathbf{k}}^n}{2}\right)\widehat{\mathbf{V}}_r^{n} \\
-\frac{\widetilde{\widehat{\epsilon}}_r^{n}+\widetilde{\mathbf{e}}_1}{2}\widehat{\mathbf{\Omega}}_r^{n} &+ \frac{\dot{\widehat{\epsilon}}_l^{n+1}+\dot{\widehat{\epsilon}}_r^{n}}{2}
\end{aligned} \tag{4.40}$$

Chapter 5

Results

5.1 Open Loop Verification

Table 5.1: Geometric parameters for Goland Wing

$b = 6.096$ m	$C_{L_0} = 0$	$C_{L_\alpha} = 2\pi$	$C_{L_\delta} = 1$	$C_{D_0} = 0.0$
$c = 1.829$ m	$C_{m_0} = 0$	$C_{m_\alpha} = 0$	$C_{m_\delta} = -0.25$	$\mu = 35.71$ kg/m
	$I_{xx} = 8.641$ kg m	$I_{yy} = 0.0$ kg m	$I_{zz} = 8.641$ kg m	

Table 5.2: Elastic parameters for Goland Wing

Number of nodes	41
Sectional center of gravity	43% chord
Elastic axis position	33% chord
Torsional Rigidity	0.987×10^6 N m^2
Bending Rigidity	9.77×10^6 N m^2

The open loop aeroelastic code has been verified for a number of test cases against standard results. Boundary conditions presented in Eq. (3.65)-(3.69) are changed to simulate a cantilevered beam case by specifying the velocity, angular velocity and pitch angle at the root. Flutter prediction results from the code are compared with results from

		analytical	computational	percentage difference
Flutter	Velocity	137.16 m/s	136.22 m/s	0.68 %
	Frequency	70.685 rad/s	70.063 rad/s	0.88 %
Free-vibration bending frequencies	1st mode	49.492 rad/s	49.502 rad/s	0.02 %
	2nd mode	310.16 rad/s	310.90 rad/s	0.24 %
	3rd mode	868.46 rad/s	874.07 rad/s	0.65 %
Divergence velocity		252.39 m/s	250.82 m/s	0.62 %
Control reversal velocity		141.38 m/s	141.40 m/s	0.01 %
Euler buckling load		648.93 kN	649.10 kN	0.03 %
Tip moment for circle		100.73 kNm	100.94 kNm	0.002 %

Table 5.3: Verification results

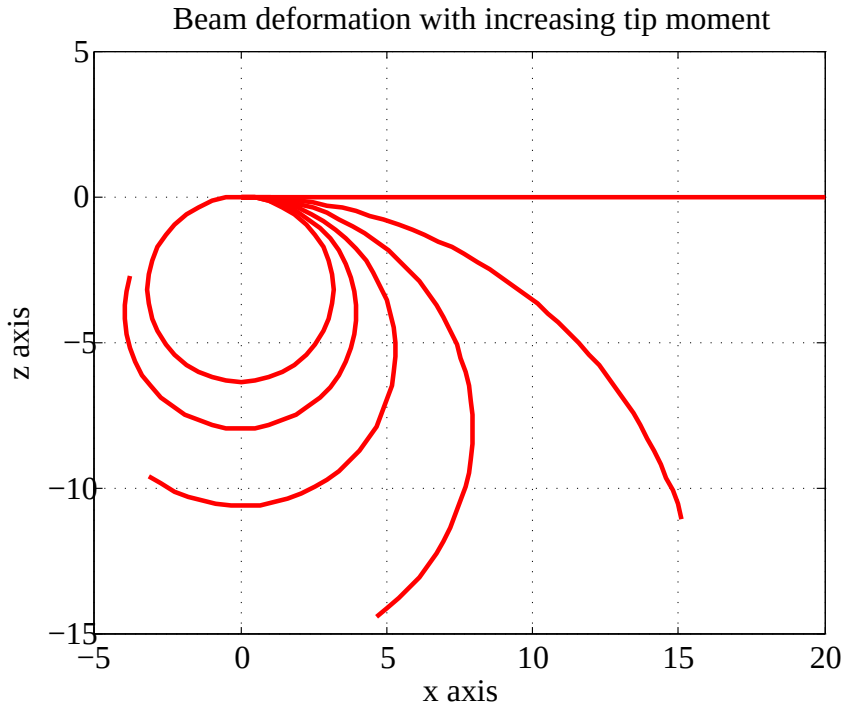

Figure 5.1: Test for geometric exactness

an analytical model for the Goland wing [90, 91] whose parameters are given in Table 5.1 and 5.2. Free-vibration bending frequencies, Euler buckling loads, divergence velocity and control reversal velocity are compared with analytical results for a modified Goland wing, which has its sectional center of mass relocated to the beam elastic axis. These results are presented in Table 5.3. Application of a sufficiently large moment about the Y axis

at the tip of the beam is seen to deform the beam into a circle as shown in Fig. 5.1, thus verifying geometric exactness of the beam model. The bending rigidity of the beam is decreased to 9.77×10^4 N m^2 for the test for geometric exactness.

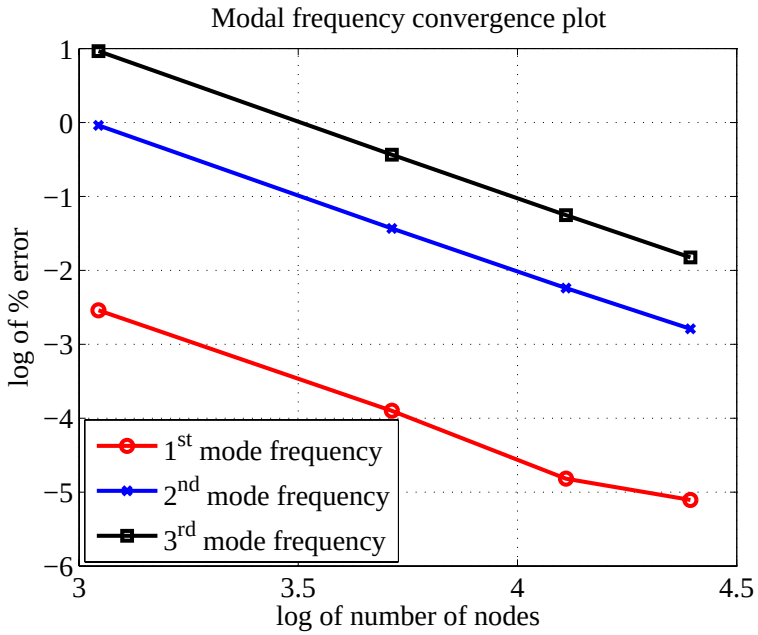

Figure 5.2: Error Convergence plot for bending frequencies

Fig. 5.2 plots the log of the percentage error between the computed and analytical bending frequencies for the cantilevered beam versus the log of the number of the nodes. The plots for all the three modes show a slope of negative two. This implies that the percentage error in the computed frequency decreases with an increase in number of nodes, and that the percentage error is inversely proportional to the square of the number of nodes.

5.2 Open Loop Dynamics

A sample configuration is used to study both open and closed loop characteristics of the flying wing. Parametric values used to define the configuration are given in Tables 5.4

and 5.5. A schematic of the configuration is given in Fig. 5.3.

5.2.1 Sample configuration

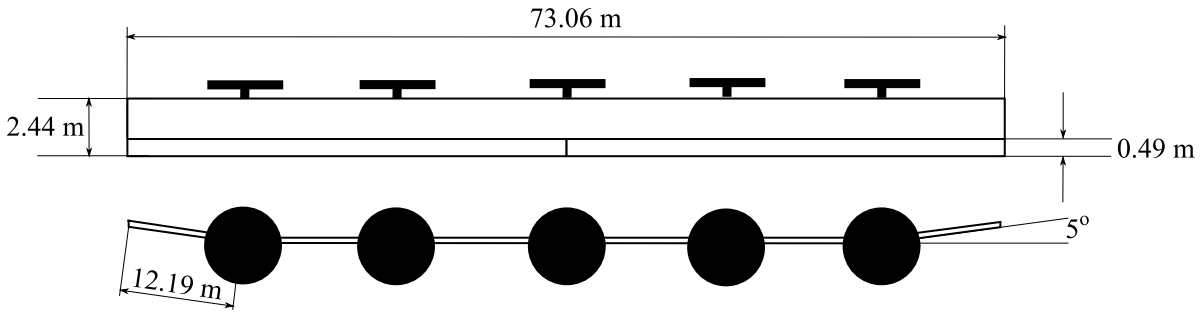

Figure 5.3: Schematic of configuration

Table 5.4: Geometric parameters for HALE configuration

$b = 73.06$ m	$C_{L_0} = 0$	$C_{L_\alpha} = 2\pi$	$C_{L_\delta} = 1$	$C_{D_0} = 0.01$
$c = 2.44$ m	$C_{m_0} = 0.025$	$C_{m_\alpha} = 0$	$C_{m_\delta} = -0.25$	$\mu = 8.93$ kg/m
	$I_{xx} = 4.15$ kg m	$I_{yy} = 0.69$ kg m	$I_{zz} = 3.46$ kg m	

Table 5.5: Elastic parameters for HALE configuration

Number of nodes	25
Payload mass variation at center	0 kg to 250 kg
Wing tip dihedral	5°
Position of wing tip dihedral	12.19 m from wing tip
Sectional center of gravity	22% chord
Elastic axis position	25% chord
Torsional Rigidity	0.165×10^6 N m^2
Bending Rigidity	1.03×10^6 N m^2
Bending Rigidity (*chordwise*)	12.39×10^6 N m^2

In order to identify the influence of static aeroelastic deformation on the open-loop flight dynamics, the following three configurations are compared: an undeformed rigid

flying wing (UNDEFORMED), a rigid flying wing defined using static aeroelastic deformation at trim for a given flight condition (DEFORMED), and a flexible flying wing configuration (FLEXIBLE). Open-loop analysis is carried out in two steps: trim computation, followed by linear stability analysis.

5.2.2 Trim Computation

A comparison of control parameters at straight and level trim for the UNDEFORMED and FLEXIBLE configuration was carried out by Patil and Hodges [7], and has not been repeated here. The trim computed for the FLEXIBLE configuration is used to defined the rigid body shape for the DEFORMED configuration. This section presents control parameters computed for four different trim states for the FLEXIBLE/DEFORMED configuration.

Figs. 5.4-5.8 shows the variation of control parameters with nodal mass at the center (payload) for four different trim cases. These consist of a straight and level trim at 12.19 m/s at sea-level, a straight climb at 12.19 m/s at a 2° slope, a level turn at 12.19 m/s with a radius of 6096 m, and a helical climbing turn at 12.19 m/s with a 2° slope and a radius of 6096 m. Increasing the payload mass at the center increases the net bending moment acting on the wing, leading to a larger bending deformation and a corresponding decrease in local angle of attack on the outboard wing sections. This effect is reflected in the variation of the required angle of attack at the root and the required aileron deflection with increasing payload mass.

As previously observed in Ref. [7], the variation in thrust required for straight and level trim is not found to vary significantly with the payload mass. This is attributed to the fact that the 2D aerodynamic model assumes a constant C_{D_0}. The thrust required for climbing flight with a 2° flight path angle increases linearly with nodal mass. This is consistent with the aircraft performance equation which shows that excess thrust required for climb increases linearly with aircraft weight for a given flight path angle [92].

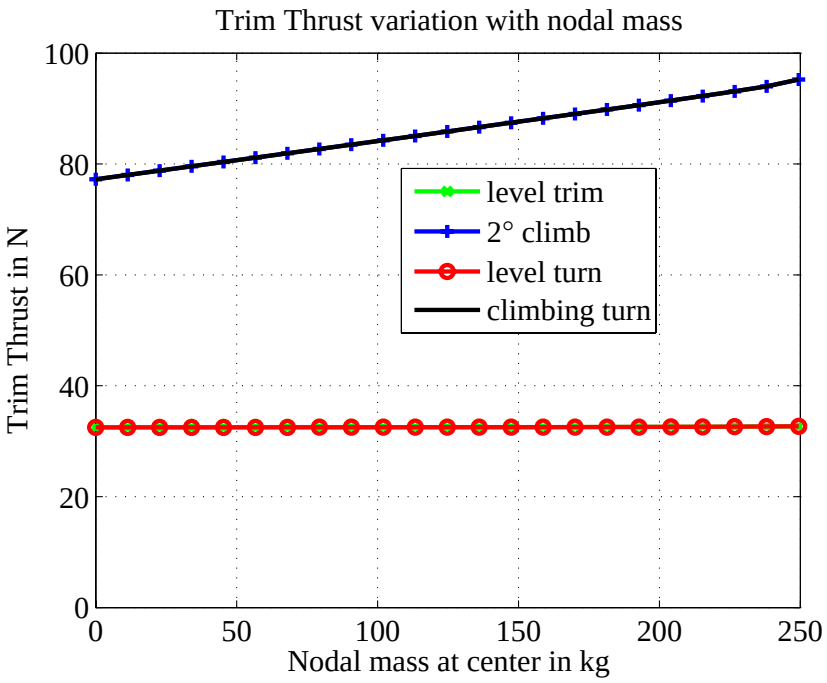

Figure 5.4: Trim Thrust variation with nodal mass

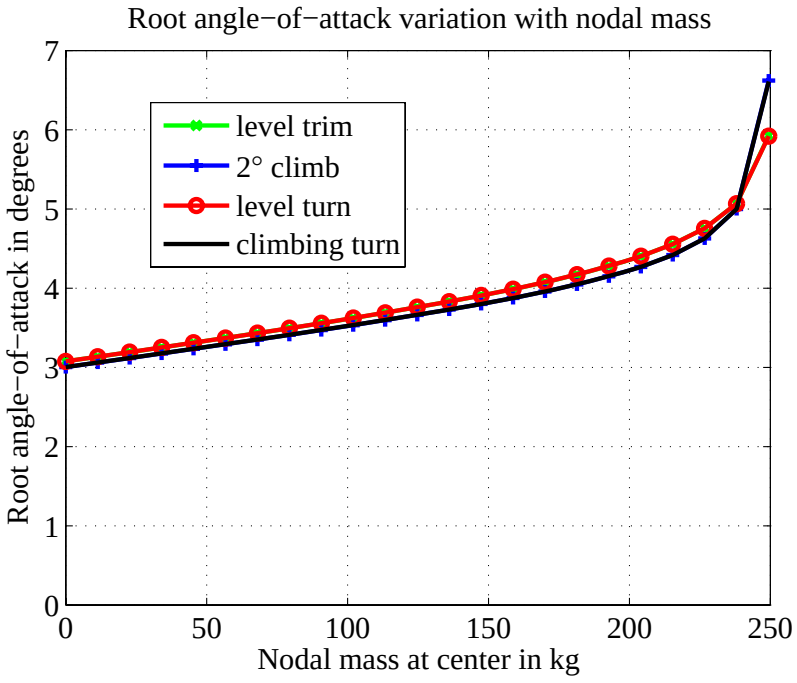

Figure 5.5: Root angle-of-attack variation with nodal mass

The angle of attack at the center node at trim is seen to increase monotonically for all trim cases. This can be attributed to the decrease in the contribution of the outboard wing sections to net aerodynamic force in the vertical direction with increasing bending deformation.

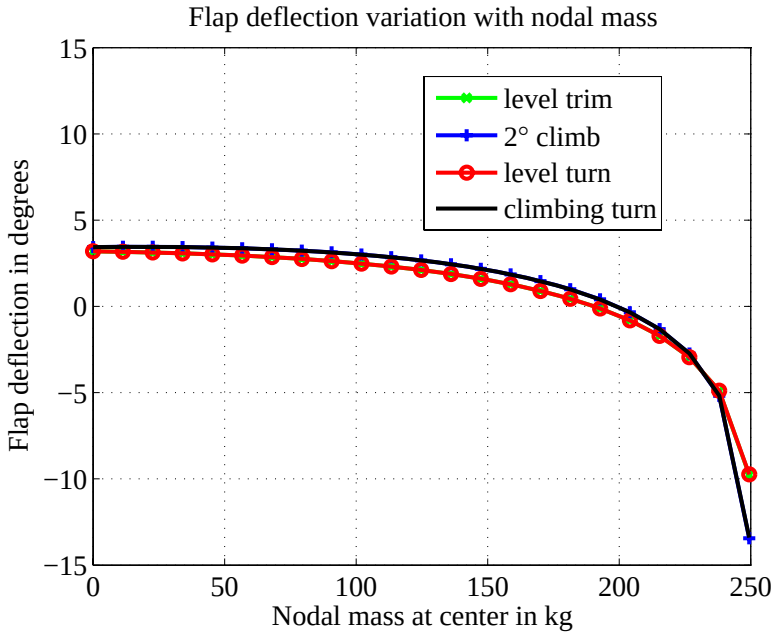

Figure 5.6: Flap deflection variation with nodal mass

The required flap deflection is positive at low values of payload mass. This value decreases with increasing payload mass and becomes negative. The decrease and change in sign of the required flap deflection can be attributed to the increase in pitch-down moment created by the outboard engines with increasing bending deformation.

The magnitude of the required aileron deflection increases with increasing payload mass. Once again, this can be attributed to the decrease in aileron effectiveness of the outboard section of the wing with increasing bending deformation. Neither the deformation, nor the sectional aerodynamic forces and moments are symmetric about the body frame YZ plane for a flying wing trimmed in turning flight, resulting in a new aerodynamic yawing moment. The differential thrust ΔT gets adjusted accordingly to trim the airplane with zero sideslip.

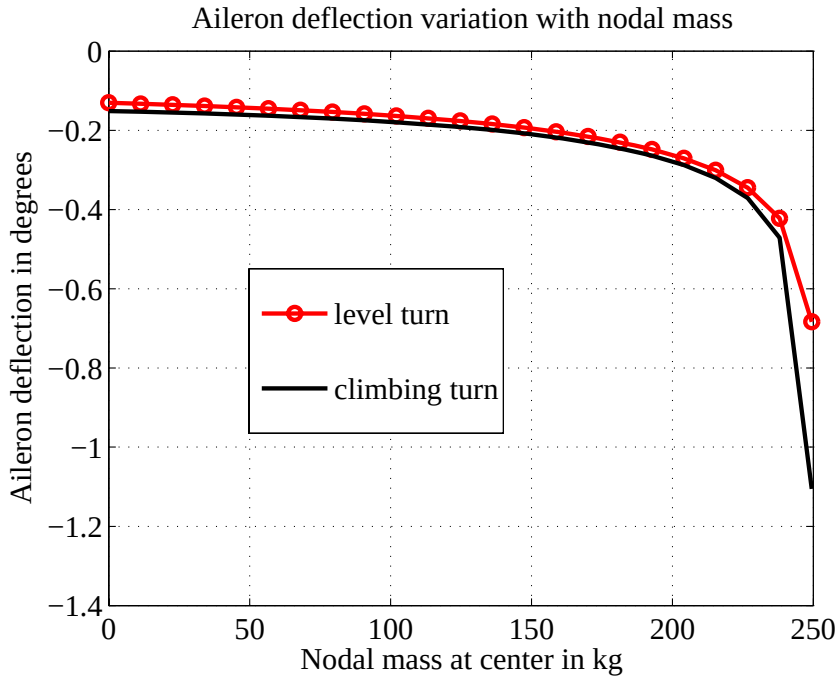

Figure 5.7: Aileron deflection variation with nodal mass

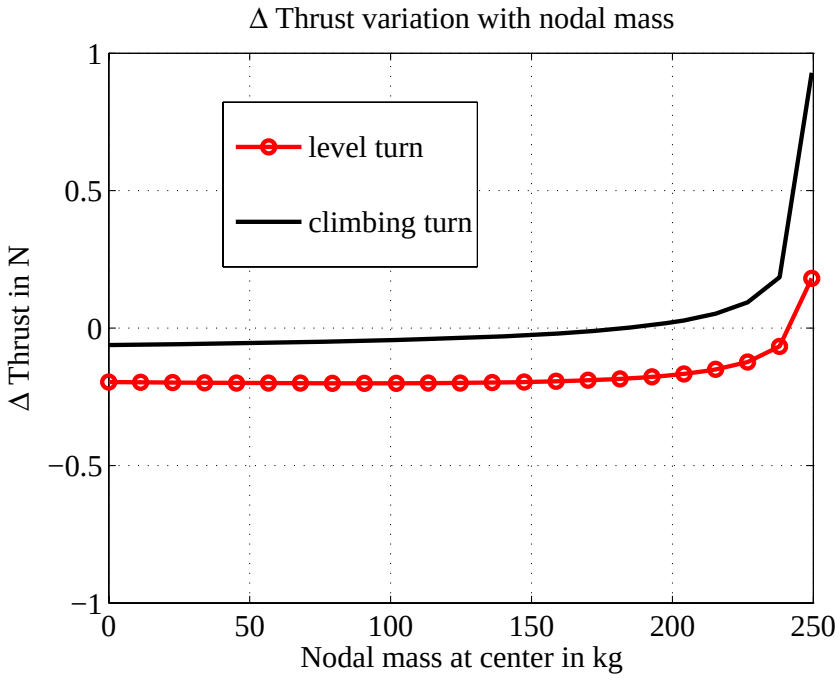

Figure 5.8: Δ Thrust variation with nodal mass

5.2.3 Linear Stability Analysis for Straight and Level Trim

This section looks at the variation of dutch roll, phugoid and spiral eigenvalues with the nodal mass at the center of the flying wing. The root locus plots for the eigenvalues are obtained by varying the nodal mass from 0 kg to 249.47 kg. The eigenvalues corresponding to the 0 kg case are indicated by green squares on the root locus plots, while the eigenvalues corresponding to the 249.47 kg case are indicated by green triangles. The roll mode and short period mode couple with the unsteady aerodynamic modes in the UNDEFORMED and DEFORMED configuration and with the aeroelastic modes in the FLEXIBLE configuration and are not studied in this section. The dutch roll and the phugoid mode exhibit dynamic instability as the nodal mass at the center of the wing is increased. This onset of dynamic instability in the FLEXIBLE configuration is captured by the DEFORMED configuration but not by the UNDEFORMED configuration. Static stability characteristics are studied in Section 5.2.5.

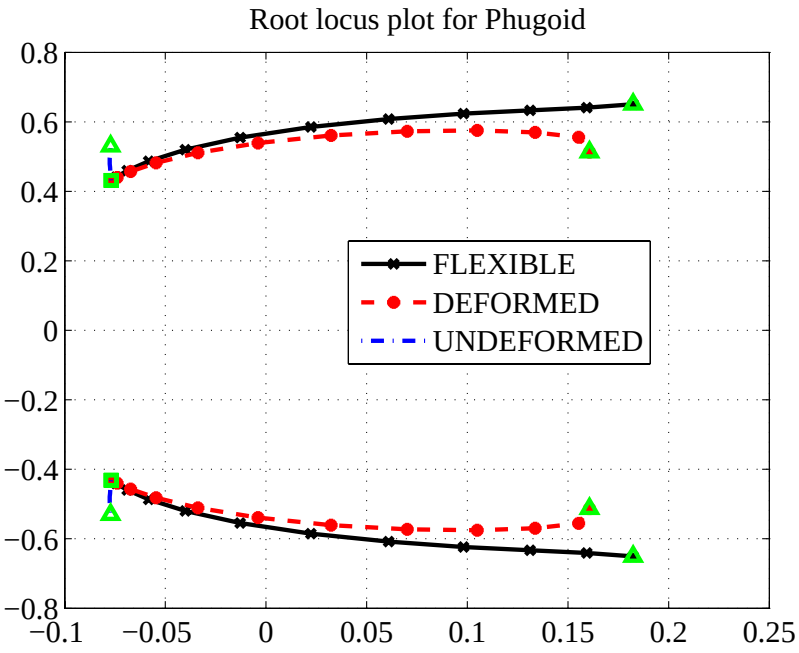

Figure 5.9: Root locus plot for Phugoid

The root locus plot for the phugoid mode is shown in Fig. 5.9. For both the FLEXIBLE and DEFORMED configuration, the phugoid mode is seen to go unstable with increasing payload mass, though the UNDEFORMED configuration remains stable as seen in Fig. 5.9. More significantly, the phugoid mode corresponding to the FLEXIBLE configuration goes unstable near the mass value at which the phugoid mode of the DEFORMED configuration crosses the zero damping line. Table 5.6 shows eigenvalues for phugoid modes for two values of payload, denoted by 'light' (45.35 kg) and 'heavy' (181.4 kg) respectively.

		'light' payload (45.35 kg)	'heavy' payload (181.4 kg)
UNDEFORMED	Phugoid	$-0.0773 \pm 0.4509\ i$	$-0.0775 \pm 0.5052\ i$
DEFORMED	Phugoid	$-0.0672 \pm 0.4572\ i$	$0.1049 \pm 0.5754\ i$
FLEXIBLE	Phugoid	$-0.0689 \pm 0.4596\ i$	$0.0981 \pm 0.6235\ i$

Table 5.6: Longitudinal Eigenvalues

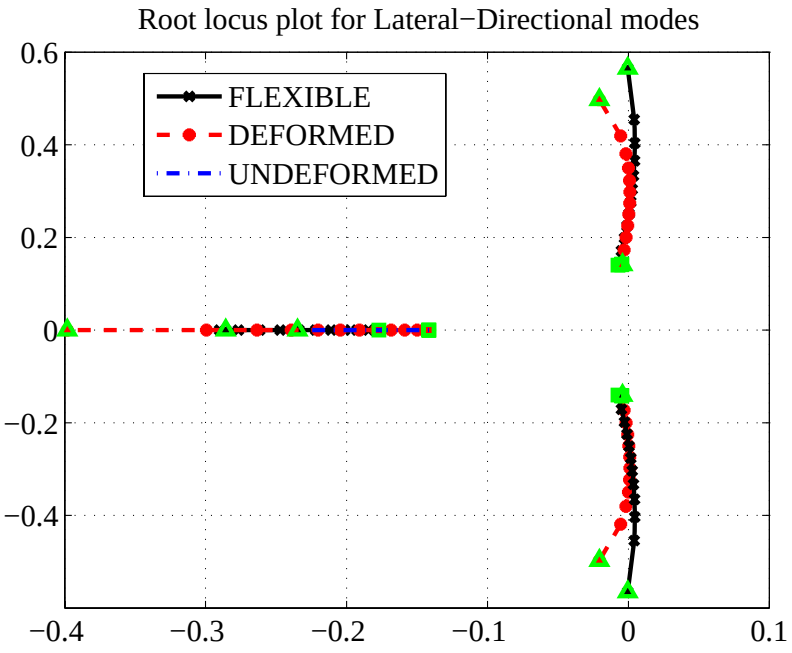

Figure 5.10: Root locus plot for Lateral-Directional modes

The root locus plot for lateral-directional modes is plotted in Fig. 5.10. For lateral-

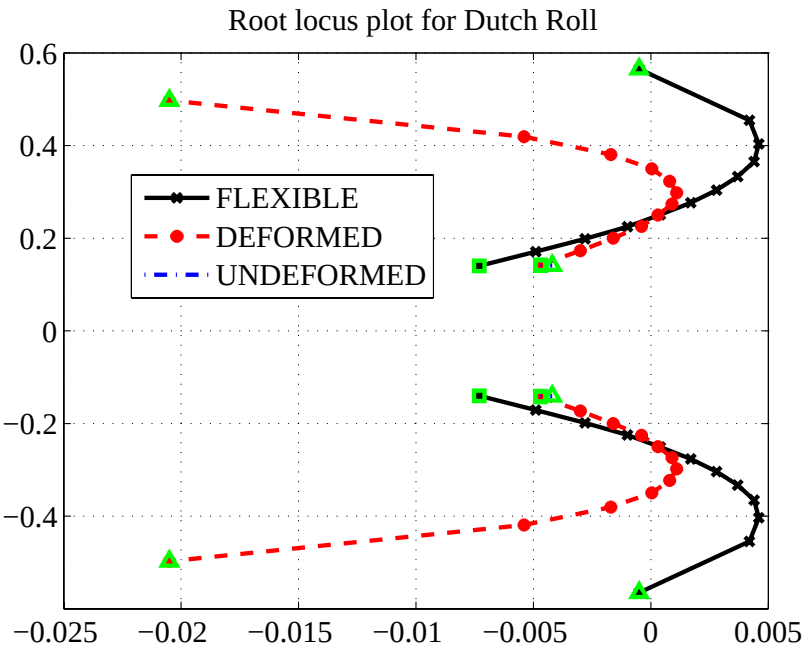

Figure 5.11: Root locus plot for Dutch roll mode

directional modes, the eigenvalues of the DEFORMED configuration are seen to track those of the FLEXIBLE configuration. The dutch roll mode is seen to go unstable with increasing payload mass in Fig. 5.11. Once again, it is seen that the instability in the dutch roll mode in the FLEXIBLE configuration is captured by the DEFORMED configuration, but not by the UNDEFORMED configuration. The spiral mode is seen to be stable for the entire range of nodal mass for all three configurations. Table 5.7 shows eigenvalues for lateral-directional modes for the 'light' and 'heavy' payload cases.

		'light' payload (45.35 kg)	'heavy' payload (181.4 kg)
UNDEFORMED	Dutch Roll	$-0.0045 \pm 0.1410\ i$	$-0.0043 \pm 0.1410\ i$
	Spiral	-0.1559	-0.2060
DEFORMED	Dutch Roll	$-0.0016 \pm 0.2003\ i$	$4.2488e-005 \pm 0.3499\ i$
	Spiral	-0.1587	-0.2392
FLEXIBLE	Dutch Roll	$-0.0028 \pm 0.1987\ i$	$0.0044 \pm 0.3654\ i$
	Spiral	-0.1925	-0.2616

Table 5.7: Lateral-Directional Eigenvalues

5.2.4 Stability Boundary for Straight and Level Trim

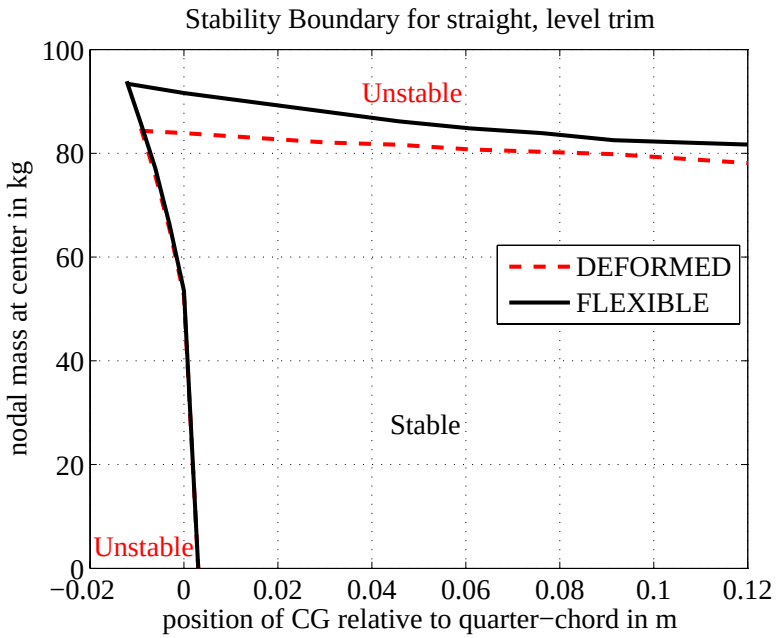

Figure 5.12: Stability Boundary

For a flying wing trimmed in straight and level flight, Fig. 5.12 shows the dependence of stability on the payload mass at the center node and position of chordwise sectional center-of-gravity location. The DEFORMED rigid wing is seen to go unstable at a lower payload value than the corresponding FLEXIBLE system for all chordwise positions of center of gravity. For both configurations, the dutch roll mode is the one that goes dynamically unstable at a lower payload (as compared to the phugoid mode) for the entire center-of-gravity range. The discussion on static stability characteristics is given in the next section.

5.2.5 Modified Static Stability Criteria

The criteria for static stability for longitudinal flight dynamics gets modified in the presence of significant structural deformation. Typically, airplanes show static stability in the longitudinal plane if the chordwise CG location is ahead of the aerodynamic center. This

center of gravity position ensures that the aerodynamic pitching moment perturbation resulting from a perturbation in angle of attack stabilizes the airplane. Mathematically, this condition is expressed as,

$$(C_{m_\alpha})_{cg} < 0 \tag{5.1}$$

The above condition assumes that the thrust does not induce a pitching moment, and consequently the net pitching moment about the center-of-gravity at trim is purely aerodynamic in nature and is equal to zero. However, for configurations which undergo significant structural deformation or have engines vertically offset from the center of gravity, thrust does induce a pitching moment. In this case, the aerodynamic pitching moment at trim about the center-of-gravity is non-zero. The condition for static stability gets modified as,

$$(C_{m_\alpha})_{cg} - (C_m^{aero})_{cg} \frac{C_{L_\alpha}}{C_L} < 0 \tag{5.2}$$

The above condition can be obtained by assuming a non-zero aerodynamic pitching moment at trim, and computing the determinant of the coefficients of the four linearized equations for dynamics in the longitudinal plane. For a given chordwise center-of-mass location, the criteria obtained in Eq. (5.2) is found to predict the nodal mass value for the onset of static instability for the DEFORMED configuration with an error of less than 1% and for the FLEXIBLE configuration with an error of 2%.

5.3 Closed Loop Dynamics

Changes to configuration

The configuration studied in the previous section was found to be susceptible to aileron reversal. In this condition, the effect of aileron deflection is to induce a rolling moment

in the opposite direction from the intended rolling moment. The dynamic pressure corresponding to onset of this instability can be detected by equating the aileron efficiency to zero, which is defined as the ratio of the rolling moment acting on the flexible wing to the rolling moment acting on the corresponding rigid wing, for the same aileron input. For an unswept, untapered, cantilevered wing with sectional center-of-mass located on the elastic axis and full span ailerons, the aileron efficiency factor is given by,

$$\eta = 1 + \frac{5}{12}\frac{C_{L_\alpha} l^2}{C_{L_\delta}} \left(\frac{\overline{q} c^2 C_{m_\delta}}{GJ} \right)$$

For the set of parameters given in the previous section, the corresponding half-span cantilevered wing was found to undergo aileron reversal at 7.19 m/s. Scaling up the torsional stiffness coefficient GJ by an order of 5 to a new value of 0.825×10^6 Nm^2 prevented aileron reversal and gave an aileron efficiency factor of 0.42. This new value of the torsional stiffness coefficient is used for all closed-loop simulations. The sectional center-of-mass is located at the quarter-chord point for the flying-wing configuration used for closed-loop simulations. Two configurations are studied in this section: a 'light' configuration with a 45.35 kg nodal mass at the center of the wing and a 'heavy' configuration with a 181.4 kg nodal mass at the center of the wing.

Static correction factor to control inputs

All closed-loop simulations presented in this section are initiated with the flying-wing trimmed in straight and level flight. Since the finite-difference based aeroelastic model used for time-marching and the reduced-order model used for control computation are not identical, a difference exists between the control inputs computed by the two models for straight and level trim. This difference serves as a static correction factor to the control inputs computed by the controller for straight and level trim, and is added to the controller output at every time-step. The static correction factor is tabulated below as a percentage of the trim control inputs from the aeroelastic model for straight and level

trim.

	thrust	flap deflection	aileron deflection	Δ thrust
'light' payload	$1.60 \times 10^{-3}\%$	$1.46 \times 10^{-4}\%$	0 %	0 %
'heavy' payload	0.0364 %	$-4.65 \times 10^{-3}\%$	0 %	0 %

Table 5.8: Static correction factor

Gain selection

For the multi-step dynamic inversion method used in this dissertation to work, it is important to ensure that the time scale for the prescribed faster dynamics is higher than the time scale for the prescribed slower dynamics. The equations for the rate of change of angular velocity constitute the faster dynamics, and are the first ones to be addressed. The selection of these gains is explained using the equation for the rate of change of angular velocity along the X^M axis. Since, the dynamic inversion controller inverts the moment equation exactly the new dynamics for the rate of change of angular momentum is given by Eq. (4.37) as,

$$ {}^M\dot{\Omega}_{M_1} \quad = \quad {}^M\dot{\Omega}^d_{M_1} = K_\Omega({}^M\Omega_{M_1 c} - {}^M\Omega_{M_1}) \tag{5.3} $$

Assuming the roll angle ϕ_{mi} to be zero, Eq. (5.3) can be re-written using Eqs. (4.29) and (4.35) as,

$$ \ddot{\theta}_{mi} = K_\Omega(K_\theta(\theta_{mi_c} - \theta_{mi}) - \dot{\theta}_{mi}) $$

which gives the following second-order equation for θ_{mi},

$$ \ddot{\theta}_{mi} + K_\Omega\dot{\theta}_{mi} + K_\Omega K_\theta\theta_{mi} = K_\Omega K_\theta\theta_{mi_c} $$

The values of K_Ω and K_θ are chosen to be 1 rad/s and 0.1 rad/s respectively, which

gives the following values for frequency and damping:

$$\begin{aligned} \omega_n &= \sqrt{K_\Omega K_\theta} = 0.316 \text{ rad/s} \\ \zeta &= \frac{1}{2}\sqrt{\frac{K_\Omega}{K_\theta}} = 1.581 \end{aligned}$$

For an overdamped second-order system, the time constant for the exponential decay of the amplitude is given by $1/\zeta\omega_n$. This time constant can be used as the characteristic time scale for the system response. For these gain values of K_Ω and K_θ, this time scale has a value of 2 s.

The time scales for the slow dynamics is determined by the guidance equations for path-following and altitude change. The rate of change of altitude can be written using Eq. (4.30) as,

$$\dot{h} = V_c \sin\gamma_c = \frac{V_c}{L_h}(h_c - h)$$

The above first-order system has a time constant given by L_h/V_c. For a prescribed flight speed of 12.19 m/s, the reference length L_h is chosen to be 1219 m, giving a time constant of 100 s. The guidance law linearized for following a straight-line path becomes a second-order equation in the lateral-offset distance, and has a frequency and damping value given by [83],

$$\begin{aligned} \omega_n &= \frac{\sqrt{2}V_c}{L_1} \\ \zeta &= \frac{1}{\sqrt{2}} = 0.707 \end{aligned}$$

For a lookforward length L_1 of 1219 m, the characteristic time scale $1/\zeta\omega_n$ has a value of 100 s. These gain values ensure sufficient separation between the time-scales for the fast and slow dynamics, and are used in all simulations presented in this section.

5.3.1 Path-following for straight line path

Straight and level path with initial vertical offset

The first set of simulations are for straight climbing flight. The simulation is initialized with the airplane trimmed in straight and level flight at 12.19 m/s along the inertial Y axis at the origin of the inertial reference frame, and is commanded to increase its altitude by 12.19 m while maintaining its heading. Two payload cases are considered: the 'light' payload case corresponding to a nodal mass at the center of 45.35 kg and a 'heavy' payload case corresponding to a nodal mass of 181.4 kg. For each of the two payload cases, simulations are presented for the fully flexible flying wing model (denoted by 'FLEXIBLE' in the graphs) and a rigid body model based on the deformed shape at straight and level trim (denoted by 'DEFORMED' in the graphs). Since the lateral variables are unperturbed in this simulation, only the longitudinal variables have been plotted in Figs. 5.13-5.14. These are the altitude of the airplane, the pitch angle of the mean axis, the commanded thrust and the commanded flap deflection.

The altitude of the airplane shows a first-order response and converges to the commanded altitude. The pitch angle of the mean axis shows an initial perturbation during climb before converging back the value for straight and level flight. The commanded thrust value shows an abrupt jump at the very first time instant corresponding to the step change in commanded altitude from the initial condition. The commanded flap deflection for the 'FLEXIBLE' configuration exhibits high frequency oscillations during the transient response for both the 'light' and the 'heavy' payload cases due to an abrupt change in commanded value. These oscillations are due to the coupling of the controller with a low-frequency aeroelastic bending mode, and die out as time progresses. Even in the presence of these oscillations, the mean value of the commanded flap deflection shows the same trend as the commanded flap deflection for the corresponding 'DEFORMED' configuration.

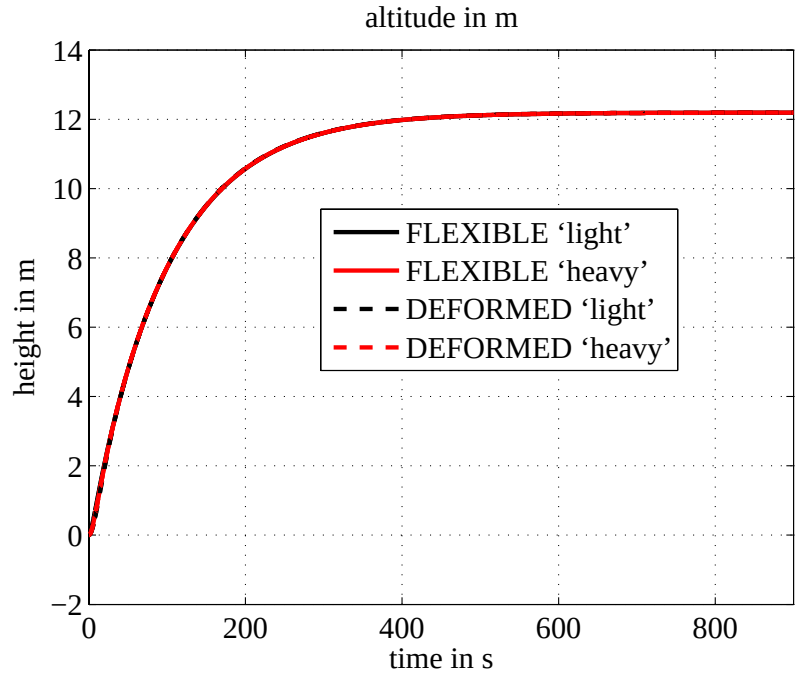

(a) Altitude history

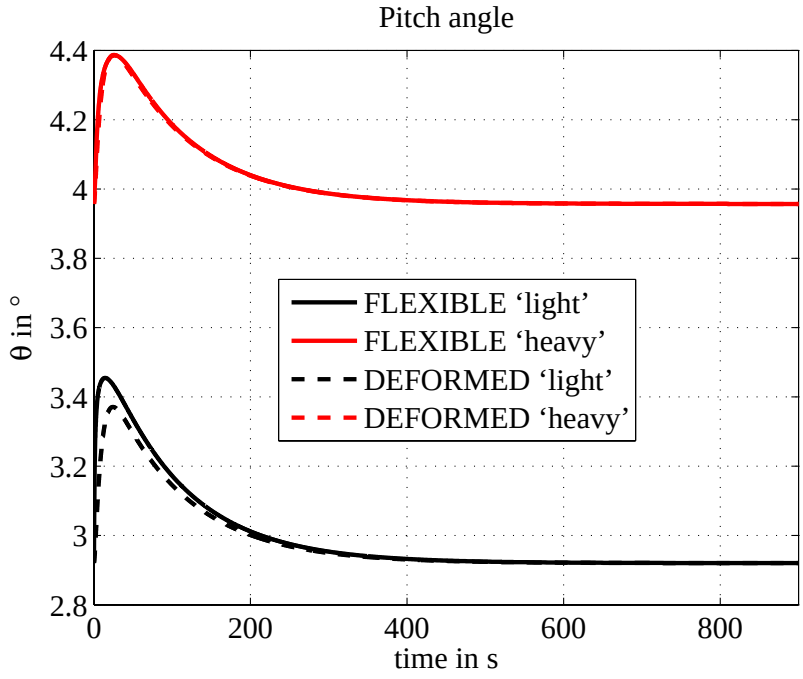

(b) Pitch angle history

Figure 5.13: Straight and level path with initial vertical offset

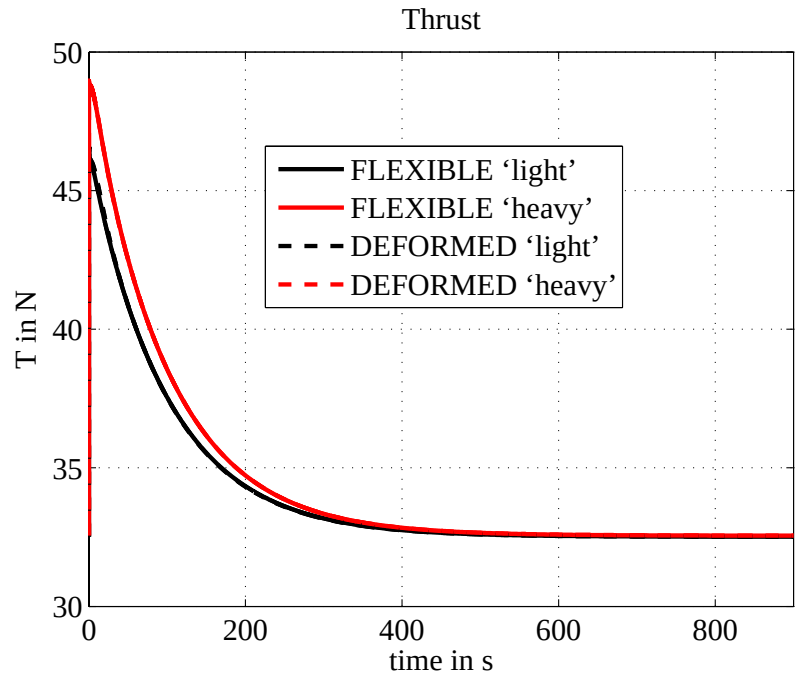

(a) Thrust history

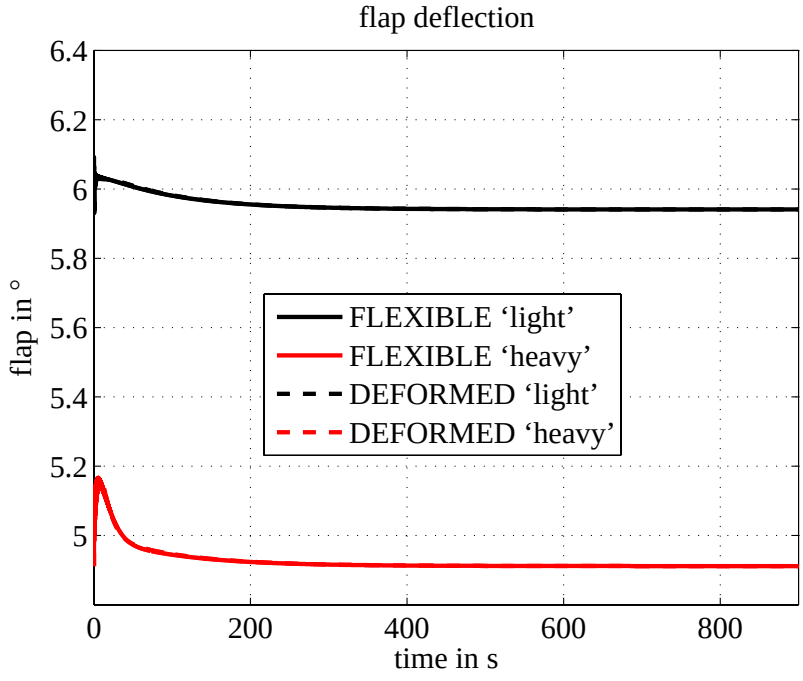

(b) Flap history

Figure 5.14: Straight and level path with initial vertical offset

Straight and level path with initial lateral offset

The second set of simulations are for level flight with an initial lateral offset from the commanded straight line path. The simulation is initialized with the airplane trimmed in straight and level flight at 12.19 m/s along the inertial Y axis at $(12.19, 0, 0)$ m in the inertial reference frame, and the airplane is commanded to follow the inertial Y axis while maintaining its altitude. As a consequence of the commanded trajectory and the initial state, lateral dynamics of the flying wing are significant in this trajectory as compared to longitudinal dynamics. Once again simulations are carried out for four cases: the 'FLEXIBLE' and 'DEFORMED' cases for both of the 'light' and 'heavy' payload. As both the lateral and longitudinal variables are perturbed from their initial values, a complete set of 9 parameters are plotted in Figs. 5.15-5.19. These are the altitude, lateral offset (the inertial 'x' co-ordinate), roll angle of the mean axis, pitch angle of the mean axis, yaw angle of the mean axis, commanded thrust, commanded flap deflection, commanded aileron deflection and commanded ΔT.

After the initial transient response, the altitude of the airplane returns to its initial value for all the four cases. The lateral offset shows a second order response with high damping and the flight path of the airplane converges to the commanded ground path. The roll and yaw angle are initialized as zero, and converge back to the same value as the flight path converges to the commanded path. High frequency oscillations are not observed in the commanded flap deflection for the 'FLEXIBLE' model as there is no abrupt change in the commanded altitude. Both the aileron deflection and the differential thrust value converge to zero after transients as the flight path of the airplane converges to the commanded ground path.

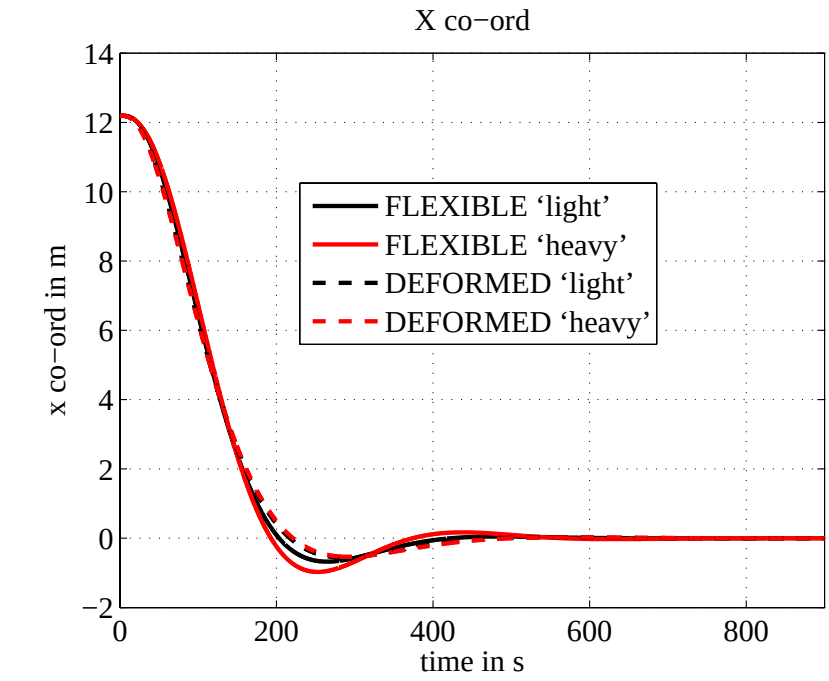

(a) Ground track history

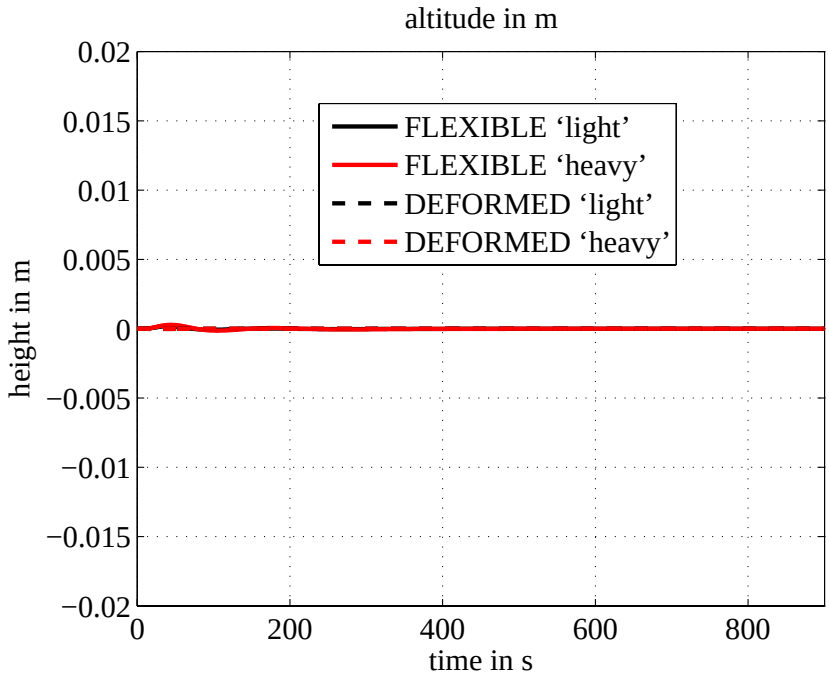

(b) Altitude history

Figure 5.15: Straight and level path with initial lateral offset

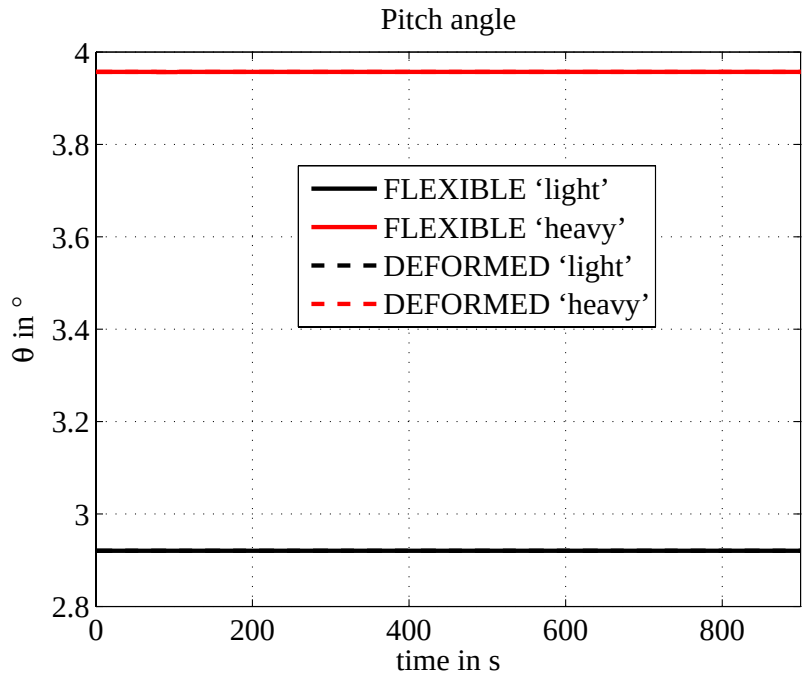

(a) Pitch angle history

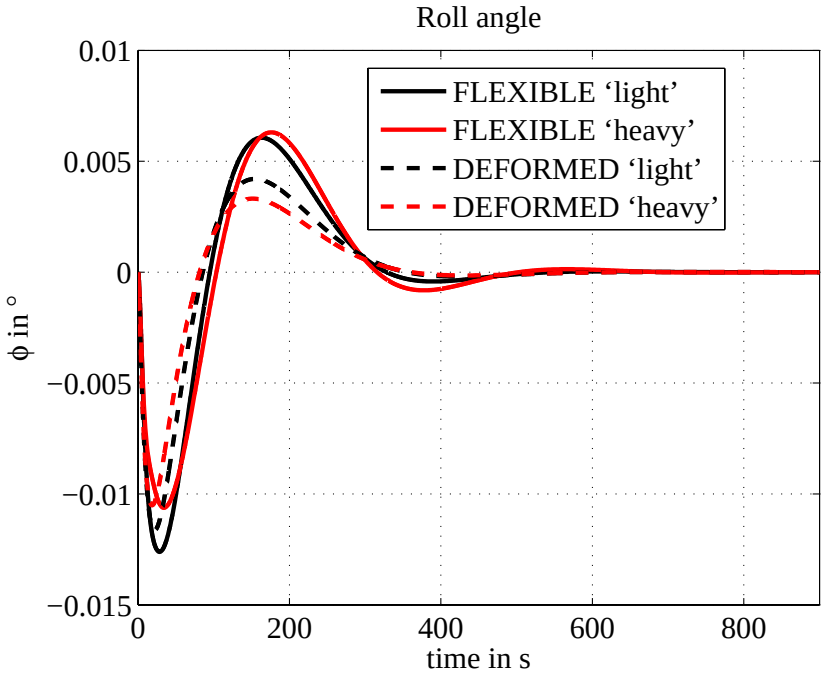

(b) Roll angle history

Figure 5.16: Straight and level path with initial lateral offset

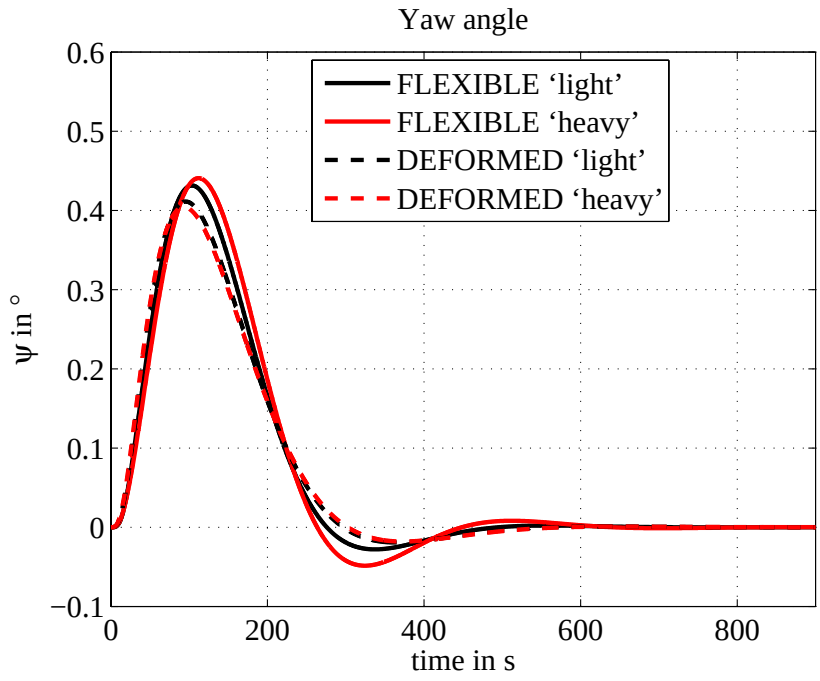

(a) Yaw angle history

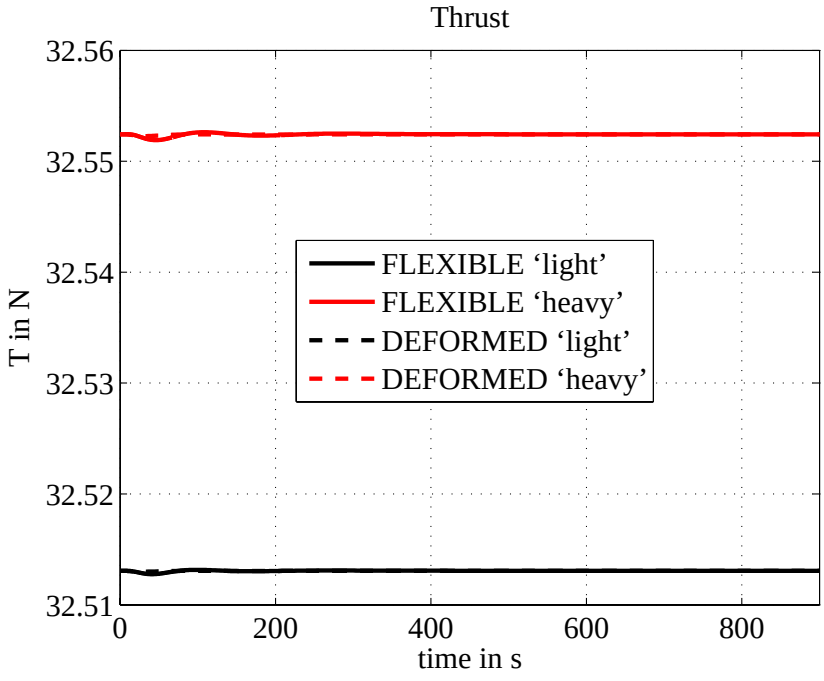

(b) Thrust history

Figure 5.17: Straight and level path with initial lateral offset

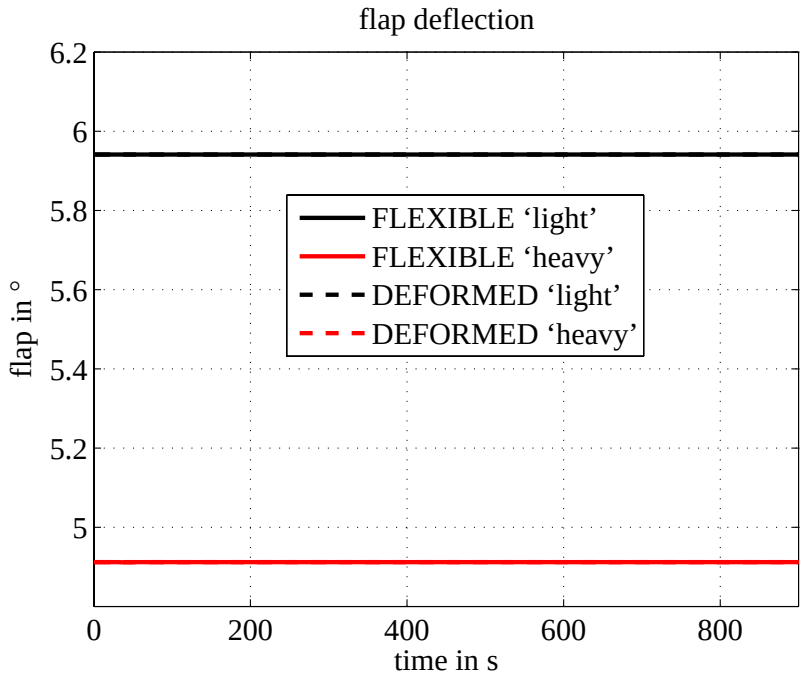

(a) Flap history

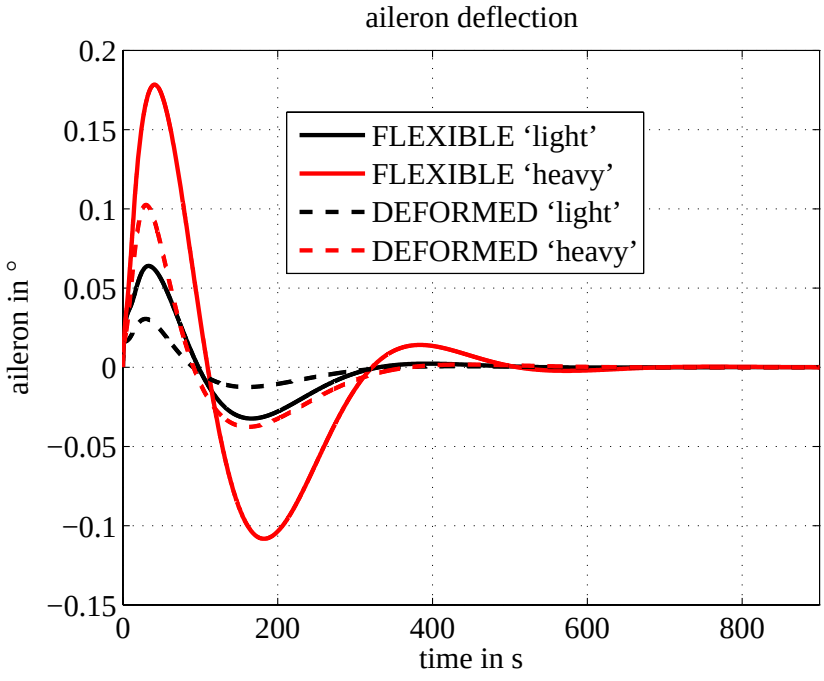

(b) Aileron history

Figure 5.18: Straight and level path with initial lateral offset

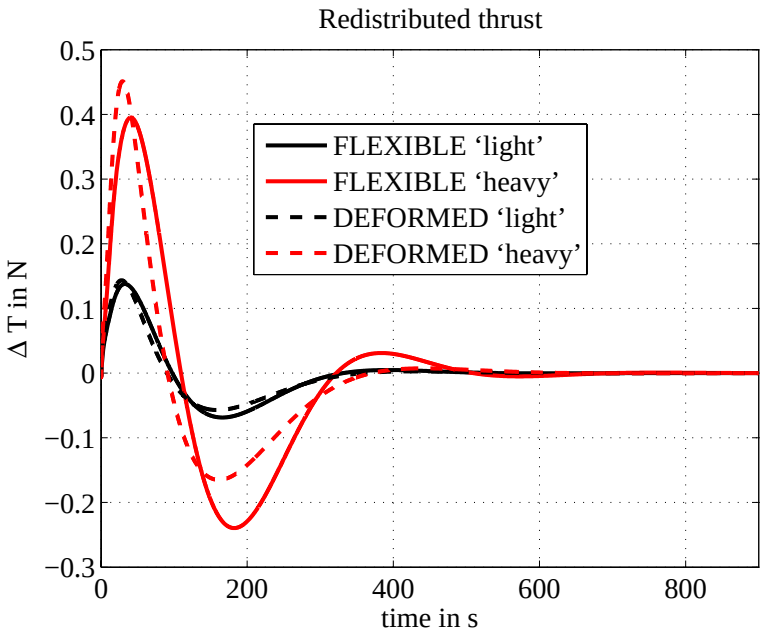

Figure 5.19: Straight and level path with initial lateral offset

5.3.2 Path-following for curved ground path

The next two sets of simulations are for following a curved ground path. The commanded path is defined to be a circle of fixed radius in the inertial XY plane. In order to study the ground path of the airplane relative to its commanded path, a new parameter is plotted for the next two sets of simulations. This new parameter ΔR is given by

$$\Delta R(t) = R(t) - R_c$$

where $R(t)$ is given by,

$$R(t) = \sqrt{(x(t) - x_0)^2 + (y(t) - y_0)^2}$$

In the above equations (x_0, y_0) represents the origin of the commanded flight path, $(x(t), y(t))$ represent the inertial co-ordinates of the airplane and R_c represents the radius of the commanded flight path.

Curved ground path with no initial offset

The simulation is initialized with the airplane trimmed in straight and level flight at 12.19 m/s along the inertial Y axis at the origin of the inertial co-ordinate system. The airplane is commanded to track a circular ground path of radius 6096 m with an origin at $(6096, 0)$ m while maintaining its current altitude. Unlike the previous two cases, the initial state of the flying wing and the final steady state correspond to two different trim conditions for this trajectory. Once again due to the nature of this trajectory, the lateral dynamics of the airplane are significant compared to the longitudinal dynamics. Both the 'light' and the 'heavy' payload cases for the FLEXIBLE configuration are studied. A total of ten parameters are plotted in Figs. 5.20-5.24. These are the ground path, ΔR, altitude, pitch, roll and yaw angles of the mean axis, and the four control parameters.

For both the 'light' and the 'heavy' payload case, the parameter ΔR and the altitude converge exactly to the commanded value. For both cases, the roll angle converges to a non-zero value corresponding to banked flight, while the yaw angle increases linearly after the transients die down. Though the airplane is commanded to maintain its altitude, the longitudinal control variables (thrust and flap deflection) do not converge to their initial value as the trim condition for turning flight is different from the trim for turning flight. The aileron deflection and differential thrust ΔT converge to a non-zero value corresponding to steady turning flight.

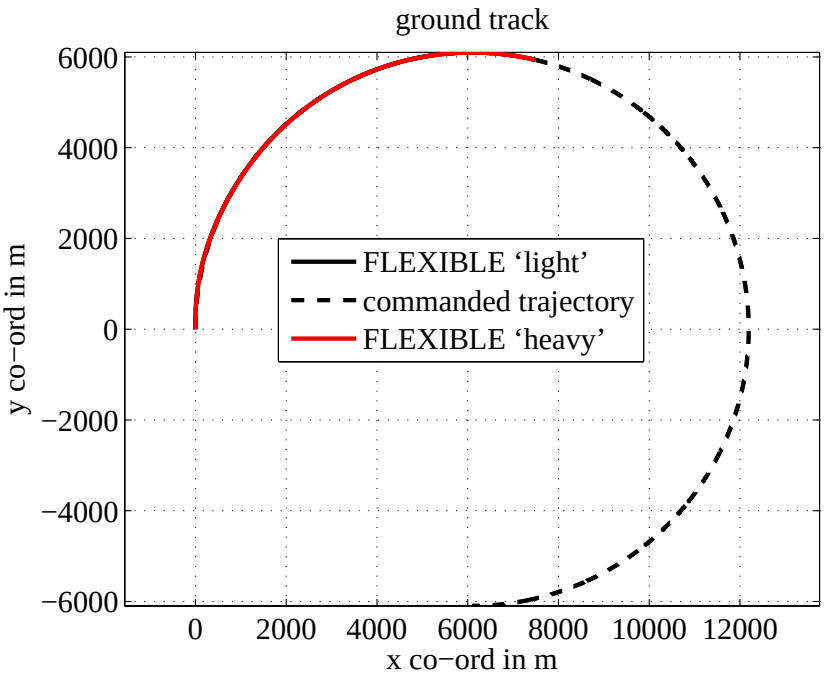

(a) Ground track history

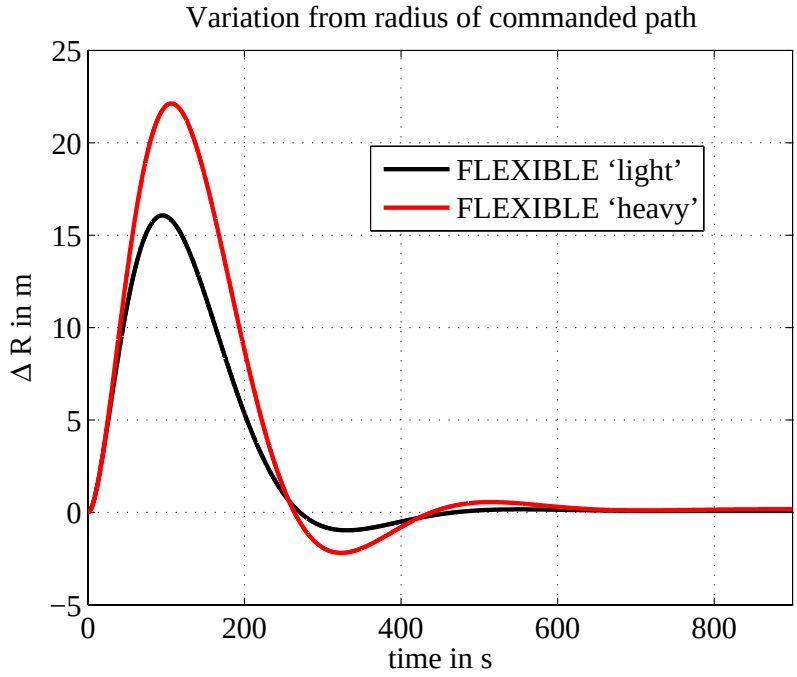

(b) Δ R history

Figure 5.20: Curved ground path with no initial offset

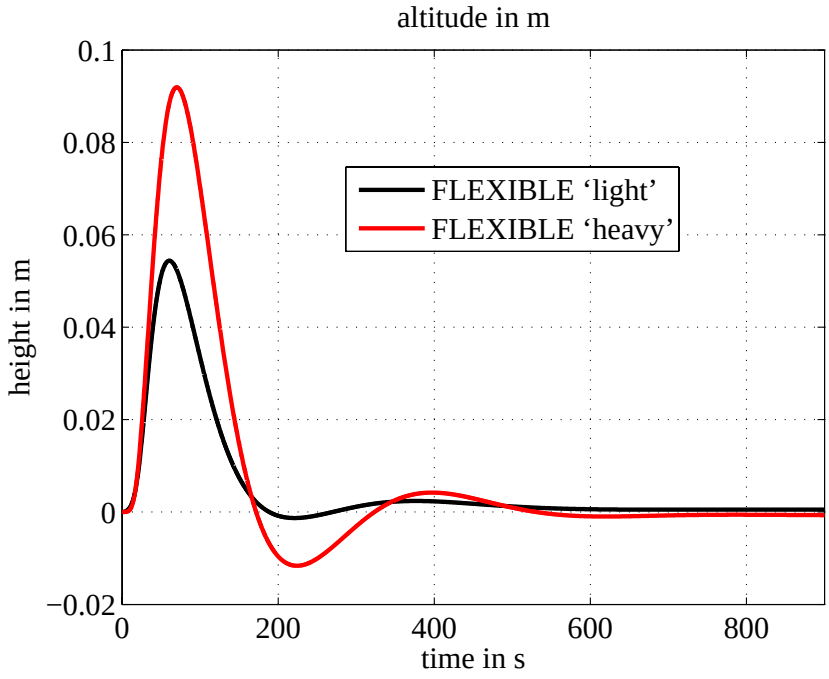

(a) Altitude history

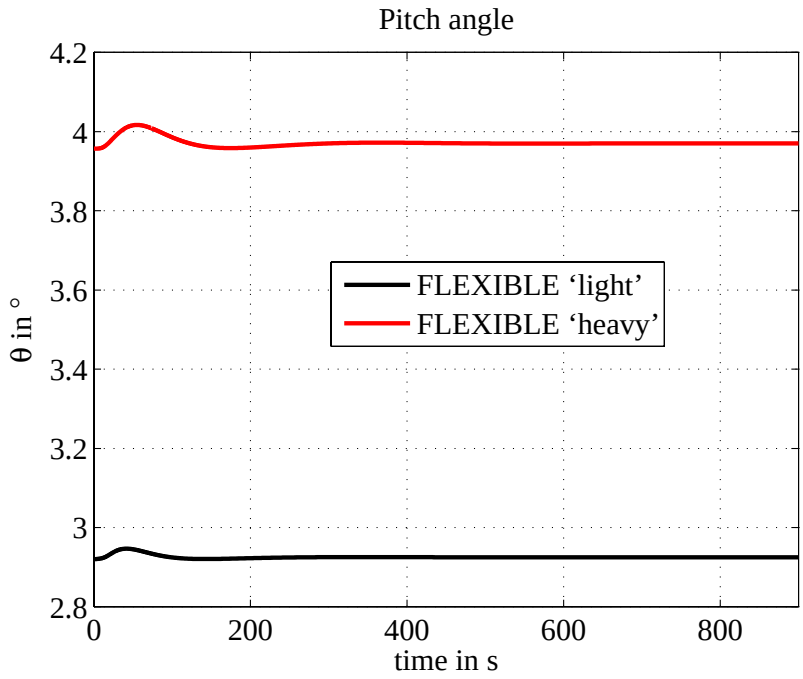

(b) Pitch angle history

Figure 5.21: Curved ground path with no initial offset

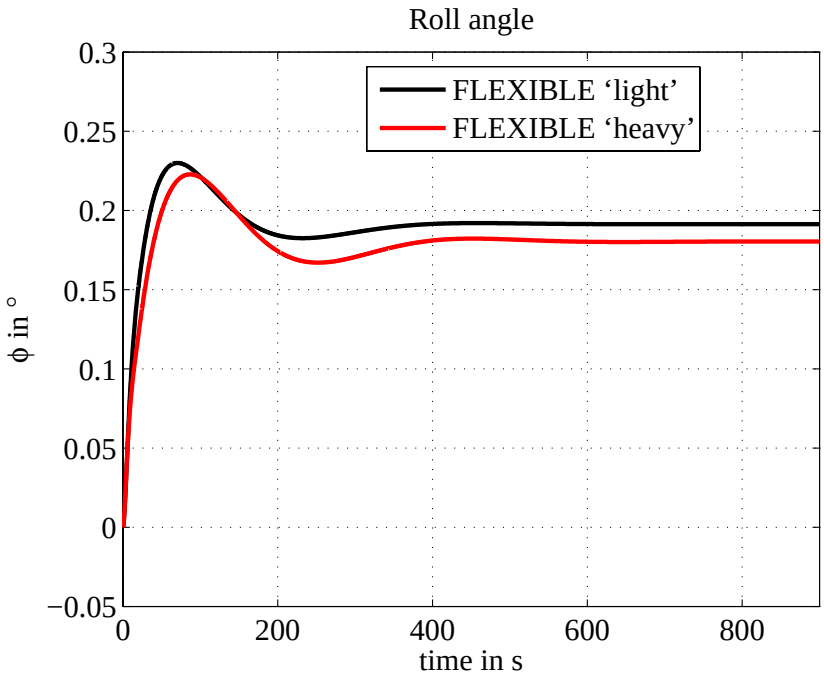

(a) Roll angle history

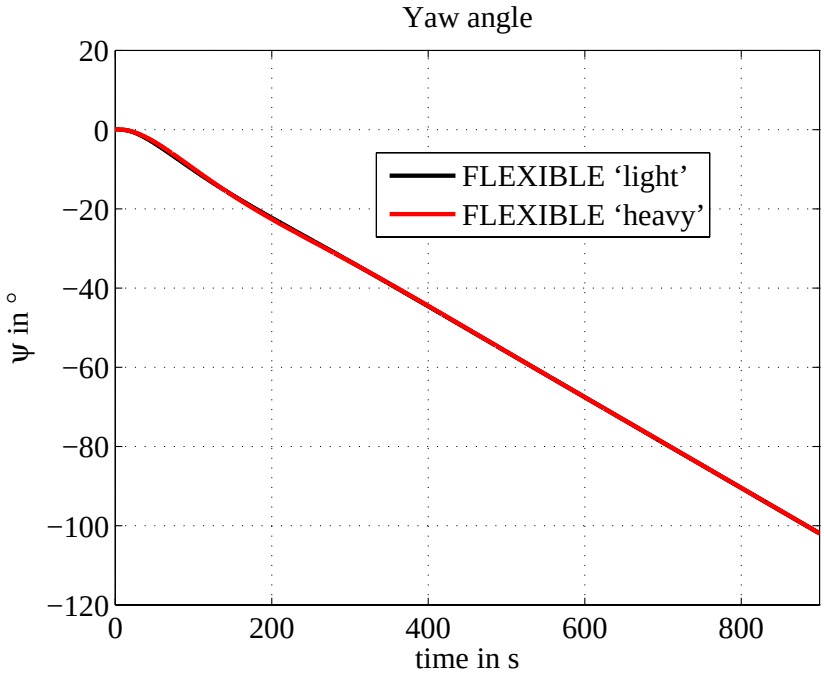

(b) Yaw angle history

Figure 5.22: Curved ground path with no initial offset

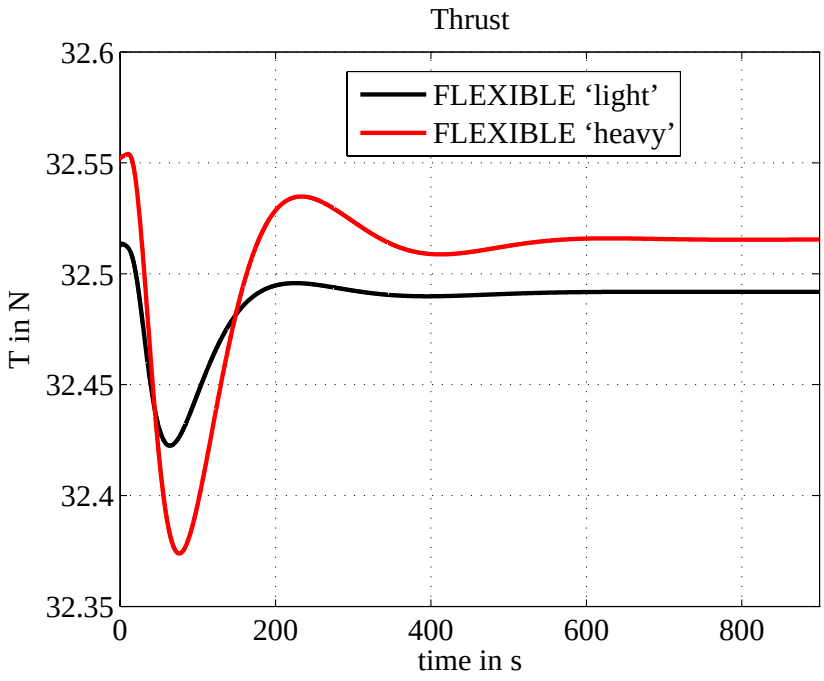

(a) Thrust history

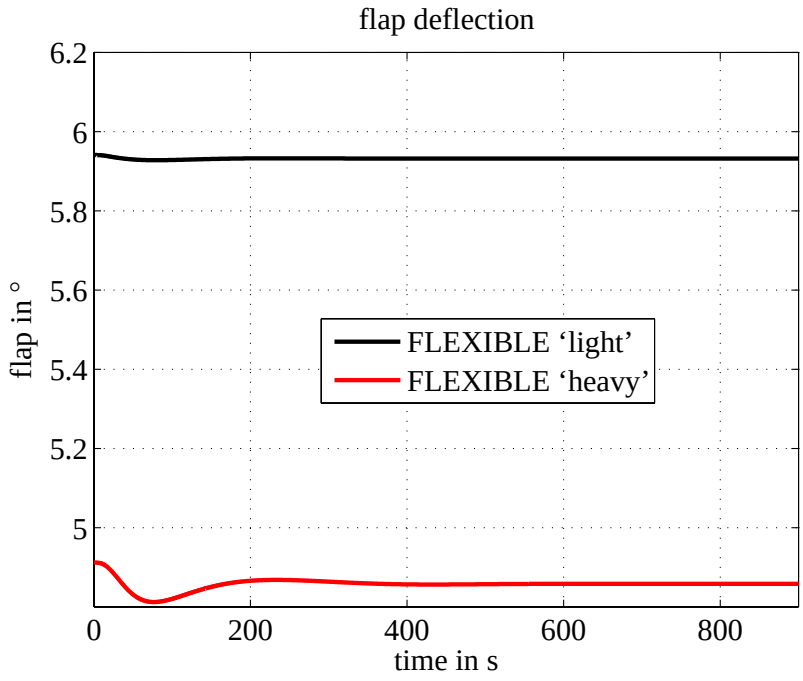

(b) Flap history

Figure 5.23: Curved ground path with no initial offset

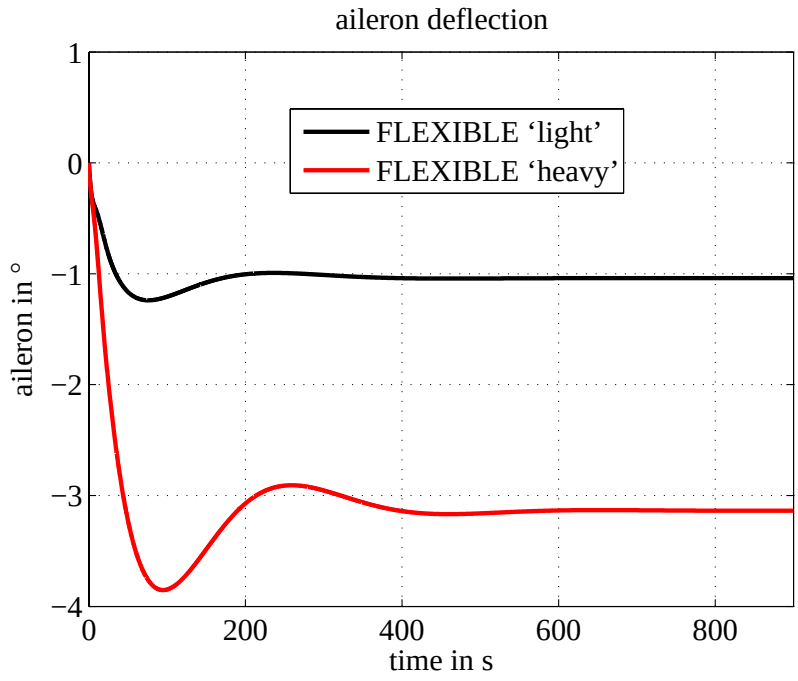

(a) Aileron history

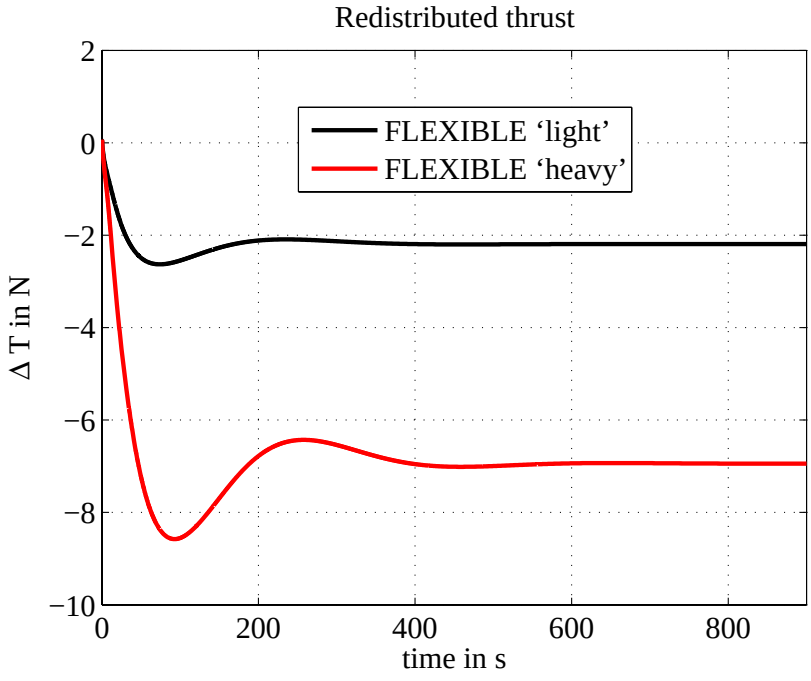

(b) Δ Thrust history

Figure 5.24: Curved ground path with no initial offset

Curved ground path with initial vertical and lateral offset

The simulation is initialized with the airplane trimmed in straight and level flight at 12.19 m/s along the inertial Y axis and with initial inertial co-ordinates of $(12.19, 0, 0)$ m. The airplane is commanded to track a circular path of radius 6096 m with an origin at $(6096, 0)$ m while increasing its altitude by 12.19 m. The commanded trajectory in this case is a combination of the commanded trajectory in the previous three cases, and the initial state and final steady state correspond to two different trim conditions. Both the 'light' and the 'heavy' payload cases for the FLEXIBLE configuration are studied. As in the previous case, a total of ten parameters are plotted in Figs. 5.25-5.29.

The parameter ΔR converges to zero for both the 'light' and 'heavy' payload cases. For both cases, the altitude converges to the commanded value of 12.19 m. The roll angle converges to a non-zero value corresponding to a banked turn while the yaw angle increases linearly with time. The commanded thrust and flap deflection converge to a steady-state value once the commanded altitude is reached. As seen in the straight climb case, the commanded flap deflection exhibits high frequency oscillations in the transient phase due to coupling with an aeroelastic bending mode of the flexible flying wing. Once again, the aileron and differential in thrust converge to non-zero values corresponding to steady turning flight.

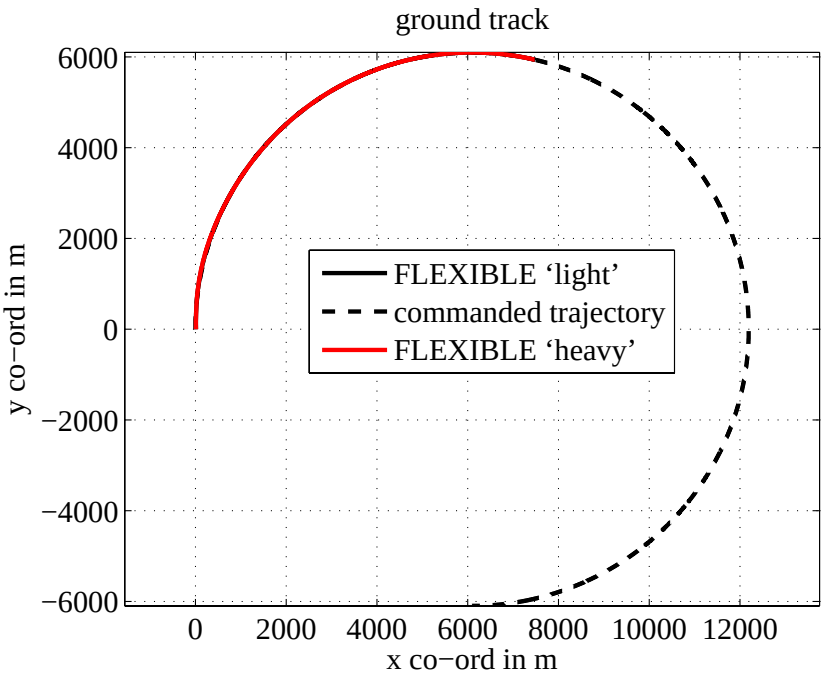

(a) Ground track history

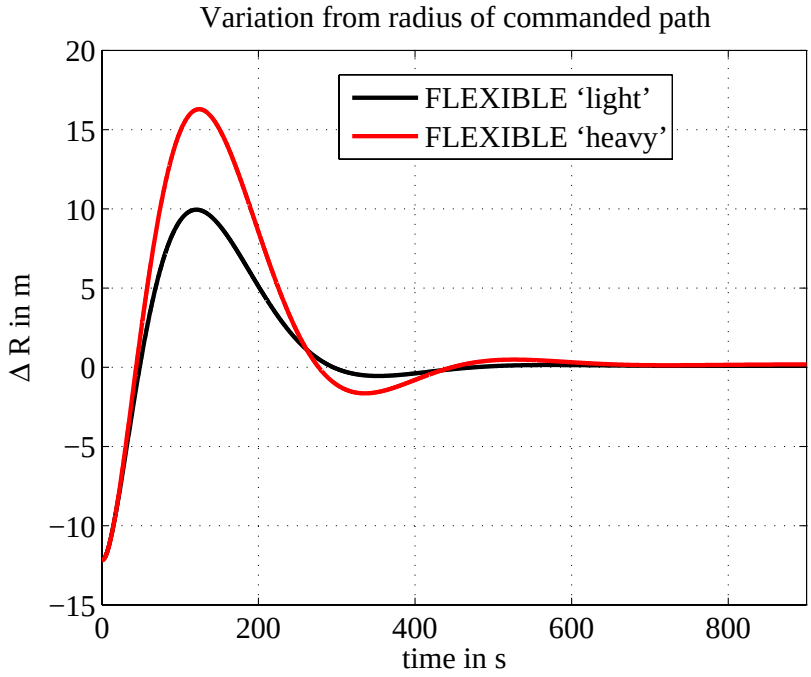

(b) Δ R history

Figure 5.25: Curved ground path with initial vertical and lateral offset

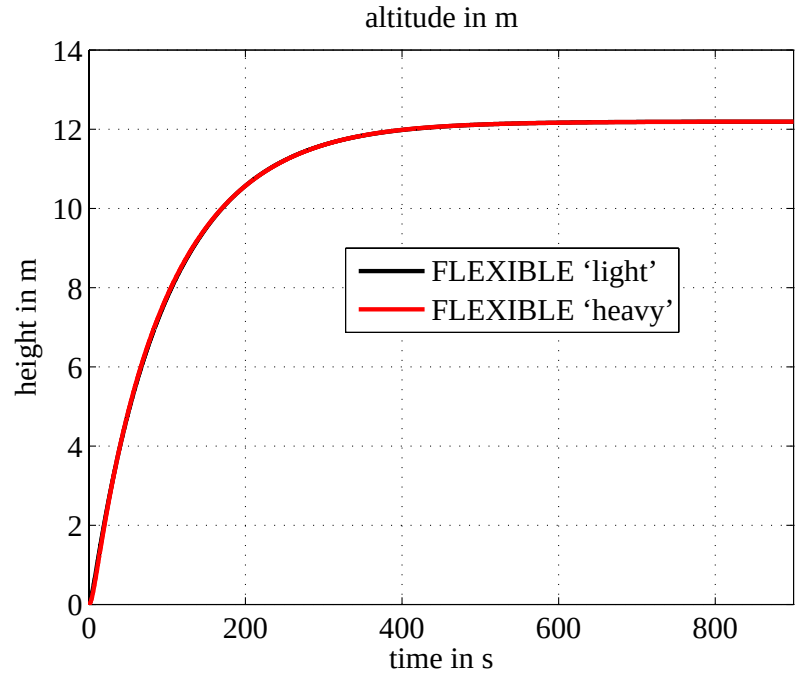

(a) Altitude history

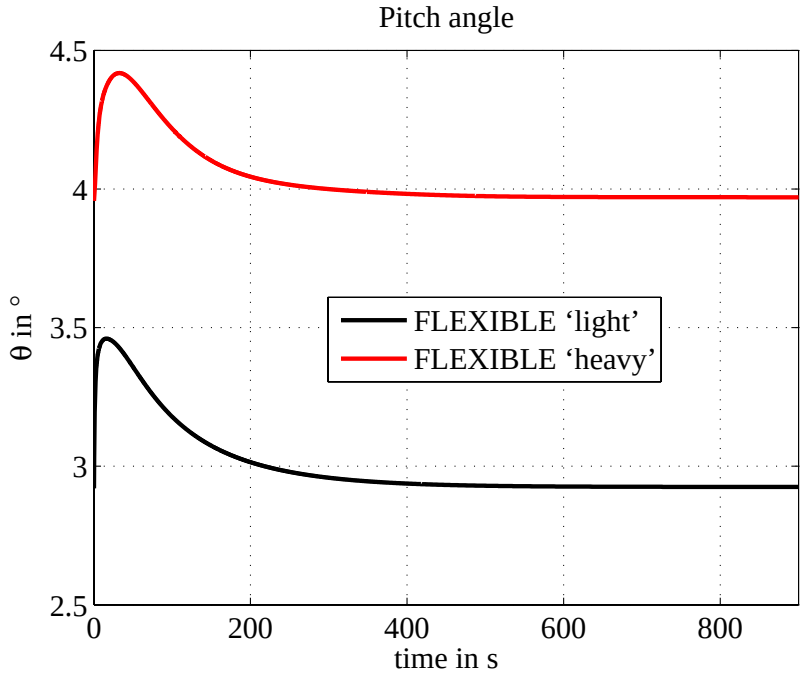

(b) Pitch angle history

Figure 5.26: Curved ground path with initial vertical and lateral offset

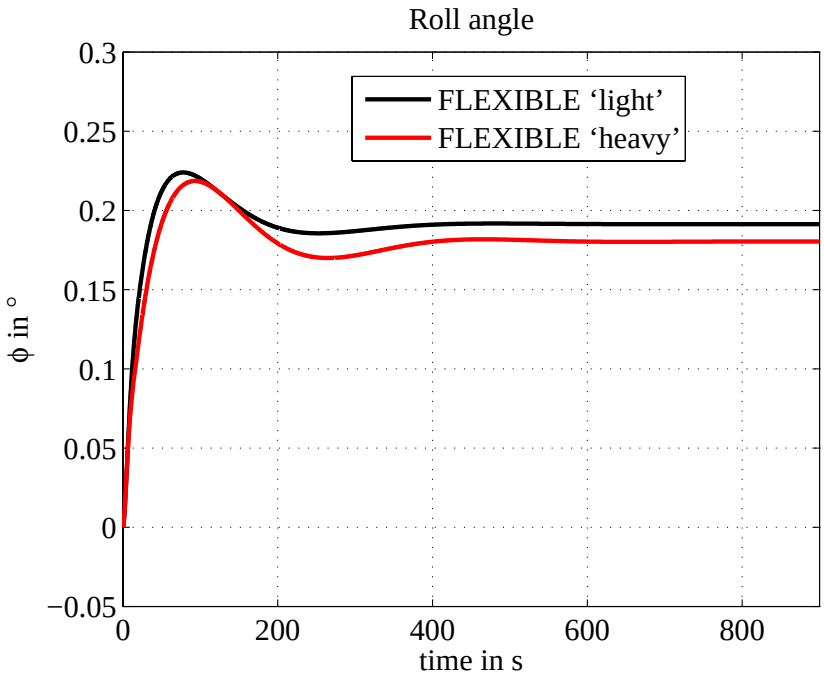

(a) Roll angle history

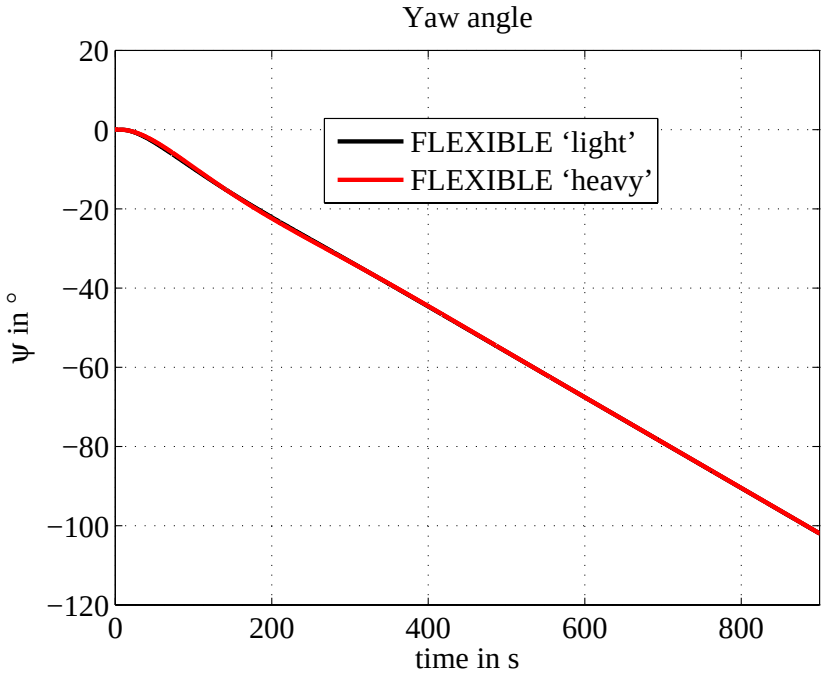

(b) Yaw angle history

Figure 5.27: Curved ground path with initial vertical and lateral offset

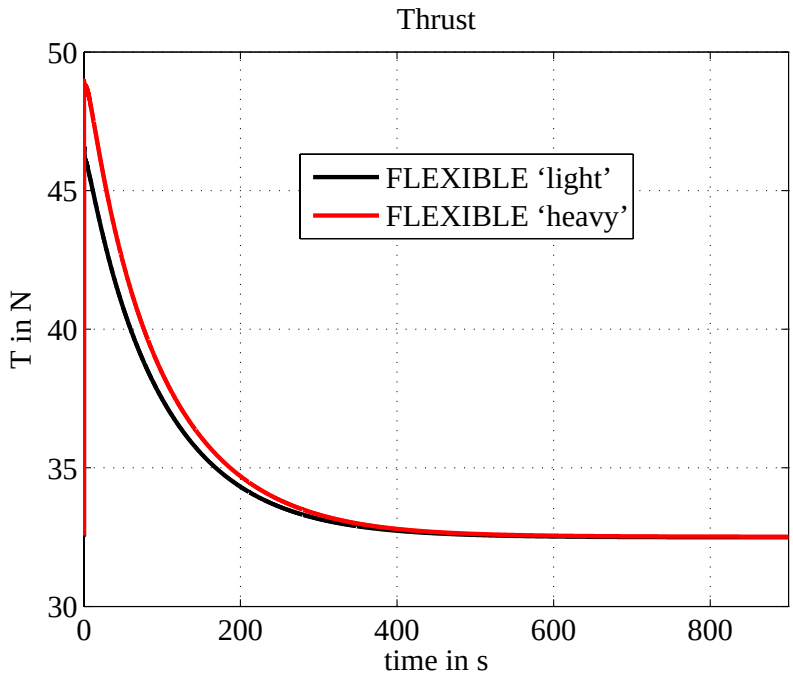

(a) Thrust history

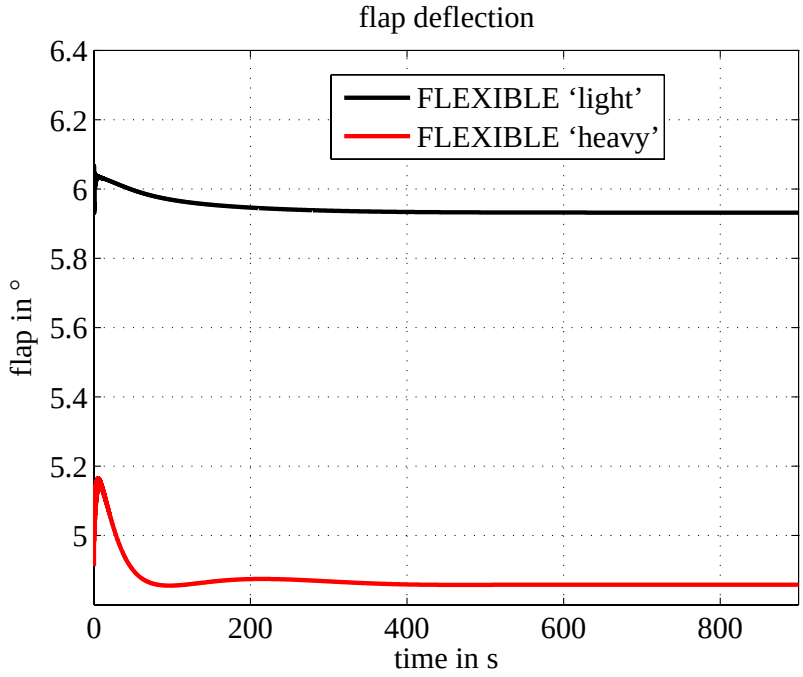

(b) Flap history

Figure 5.28: Curved ground path with initial vertical and lateral offset

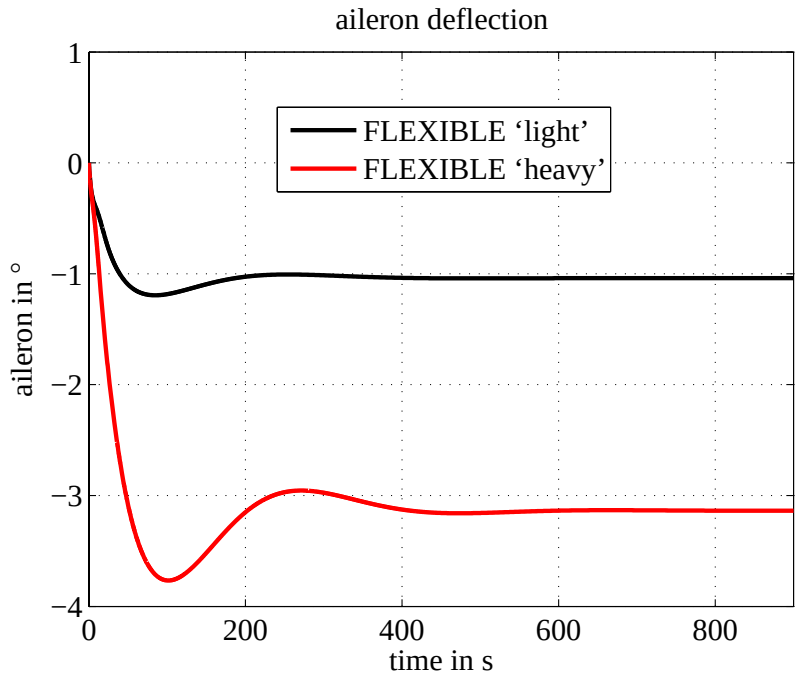

(a) Aileron history

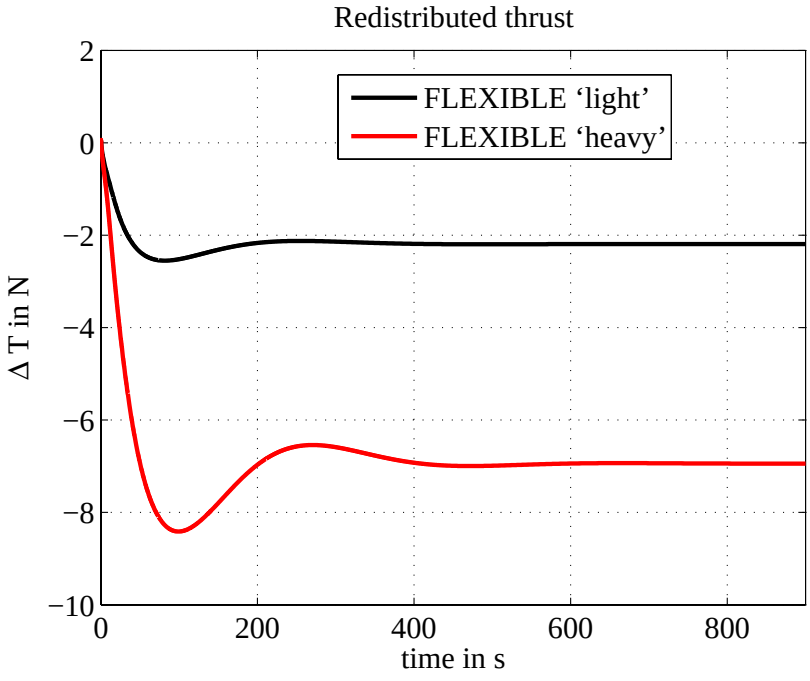

(b) Δ Thrust history

Figure 5.29: Curved ground path with initial vertical and lateral offset

5.3.3 Extreme cases

This subsection studies the variation in the response of the closed loop system with increasing lateral offset and climb altitude, and decreasing turn radius. As noted in Section 3.1, the controller assumes a linear variation in ΔT across the five engines and full span ailerons. The limits of the closed-loop system identified in this section will change if this control distribution is changed. All simulations in this subsection are carried out with a payload mass of 181.4 kg and initialized with the flying wing trimmed in straight and level flight at 12.19 m/s along the inertial Y axis, unless specified otherwise.

Straight and level path with initial vertical offset

The first set of simulations looks at the response of the system to a commanded change in altitude by 304.8 m and 152.4 m respectively while maintaining its heading. The simulation is initialized with the airplane at the origin at the inertial reference frame. The commanded altitude in subsection 5.3.1 was chosen to be 12.19 m and the corresponding simulations are provided here as a reference.

Once again, the lateral states are not perturbed. The altitude of the airplane shows a first-order response and converges to the commanded altitude. The time required for the airplane to reach the commanded altitude for all three cases in found to be of the same order. However this will no longer be true in a real system as constraints on the maximum thrust of the engine are imposed. The jump in the commanded thrust at the very first time instant increases with an increase in the commanded altitude. The commanded flap deflections exhibit damped high frequency oscillations in the transient response due to coupling with bending modes. The steady state values of the thrust, flap and pitch angle converge to their initial values as these correspond to straight and level flight.

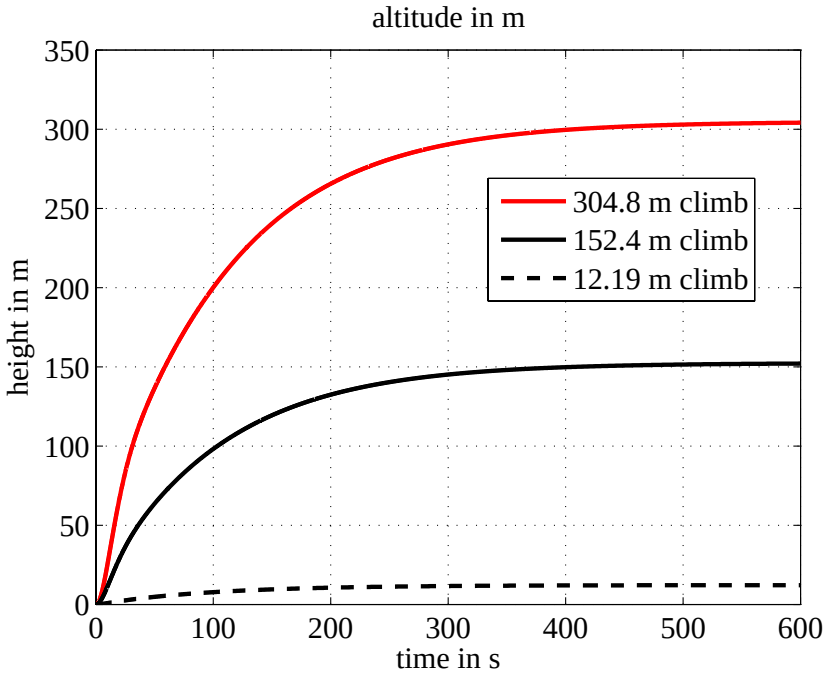

(a) Altitude history

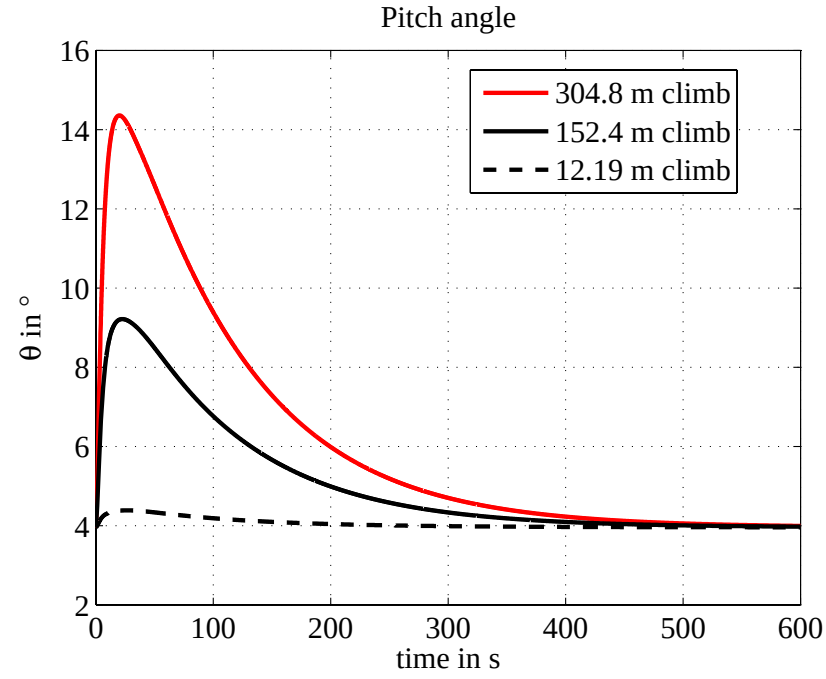

(b) Pitch angle history

Figure 5.30: Straight and level path with initial vertical offset (large offsets)

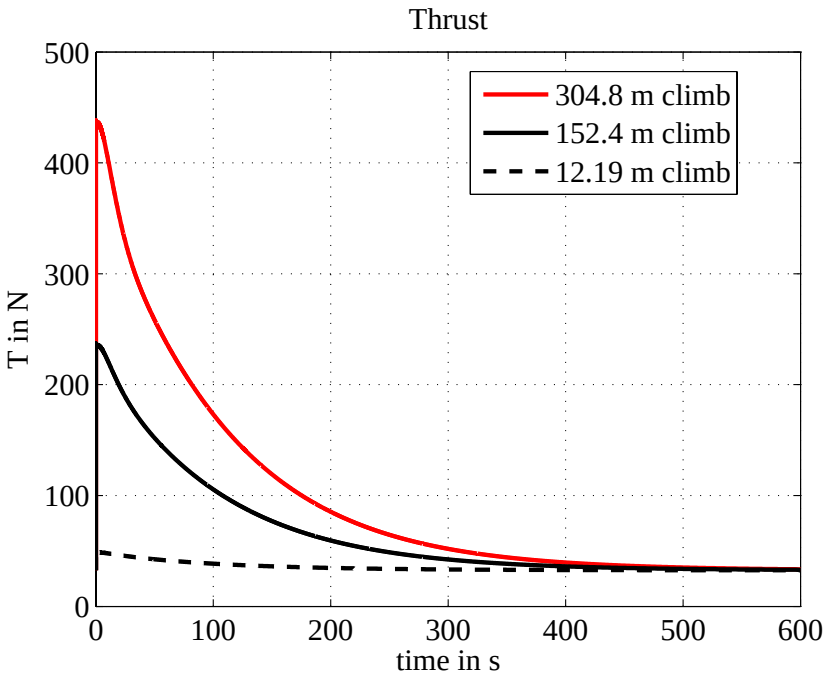

(a) Thrust history

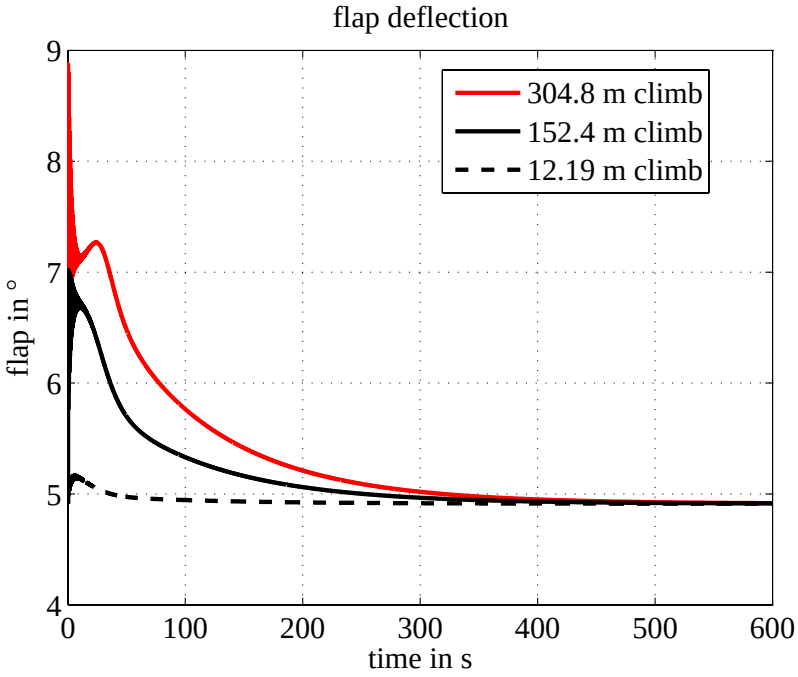

(b) Flap history

Figure 5.31: Straight and level path with initial vertical offset (large offsets)

Straight and level path with initial lateral offset

The next set of simulations studies the variation of the closed-loop response of the flying wing with increasing lateral offsets. The initial positions of the airplane are taken to be $(304.8, 0, 0)$ m and $(152.4, 0, 0)$ m respectively. The flying wing is commanded to track the inertial Y axis while maintaining its altitude. The results from section 5.3.1 for straight line path following with an initial lateral offset of 12.19 m are reproduced here as a reference. The states and control inputs are plotted in Figs. 5.32-5.36.

As seen in section 5.3.1, the lateral offset shows a second order response and converges to zero for all cases. Moreover, the time required for convergence for all three cases is found to be of the same order of magnitude. The transient response for control inputs and states show similar trends for all three cases, with the magnitudes increasing with increasing lateral offset. All the control inputs, Euler angles and the altitude of the flying wing converge back to their initial value after the transients die down, as the initial condition and the steady state correspond to the same trim. Unlike the case for climbing flight, the flap deflections do not exhibit high frequency transient oscillations, nor does the required thrust reach unrealistically large magnitudes.

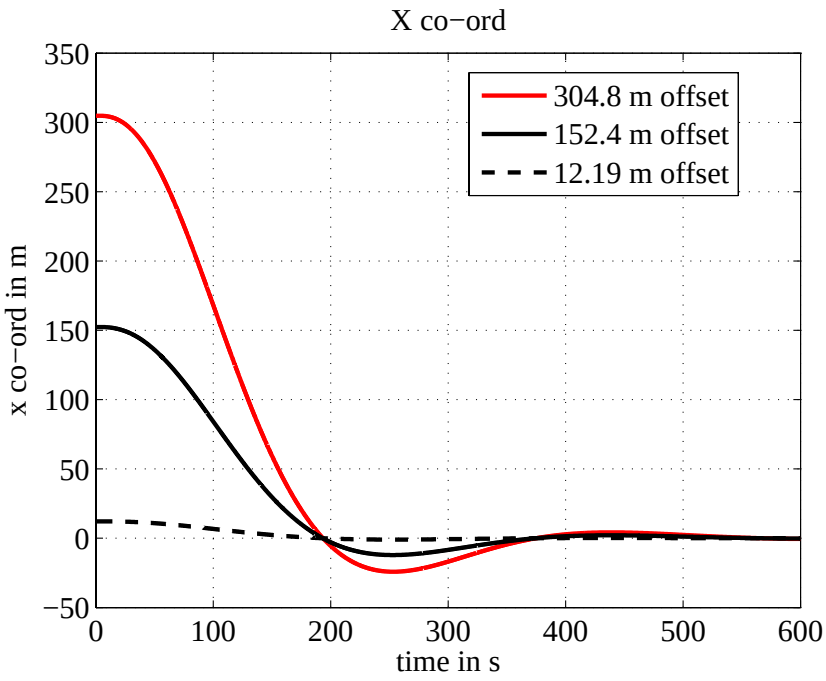

(a) Ground track history

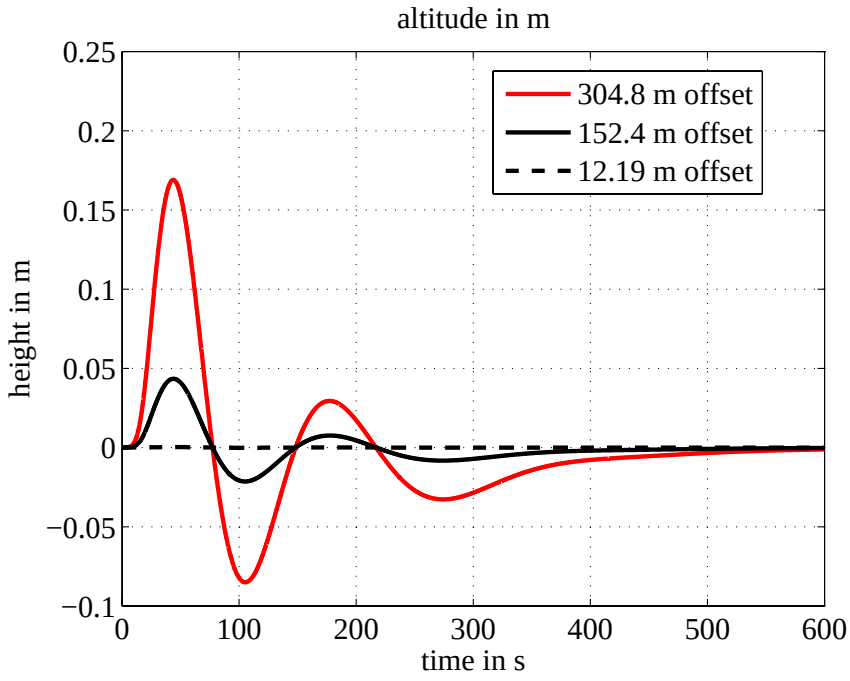

(b) Altitude history

Figure 5.32: Straight and level path with initial lateral offset (large offsets)

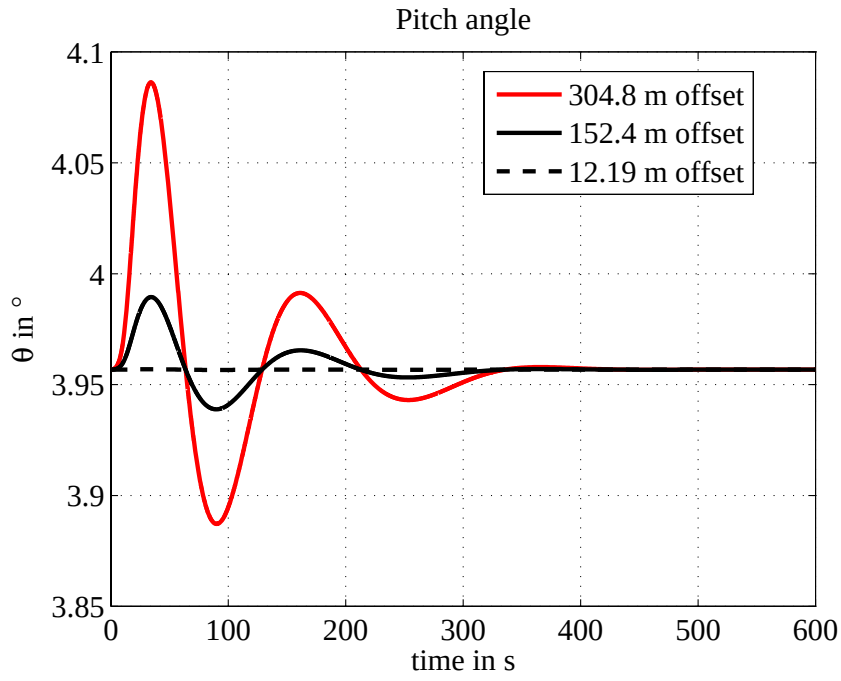

(a) Pitch angle history

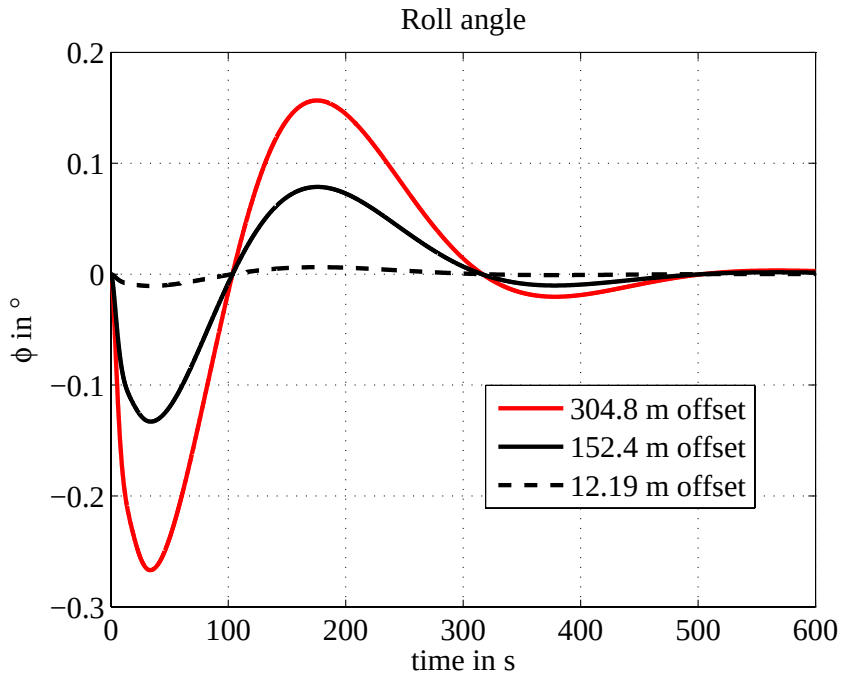

(b) Roll angle history

Figure 5.33: Straight and level path with initial lateral offset (large offsets)

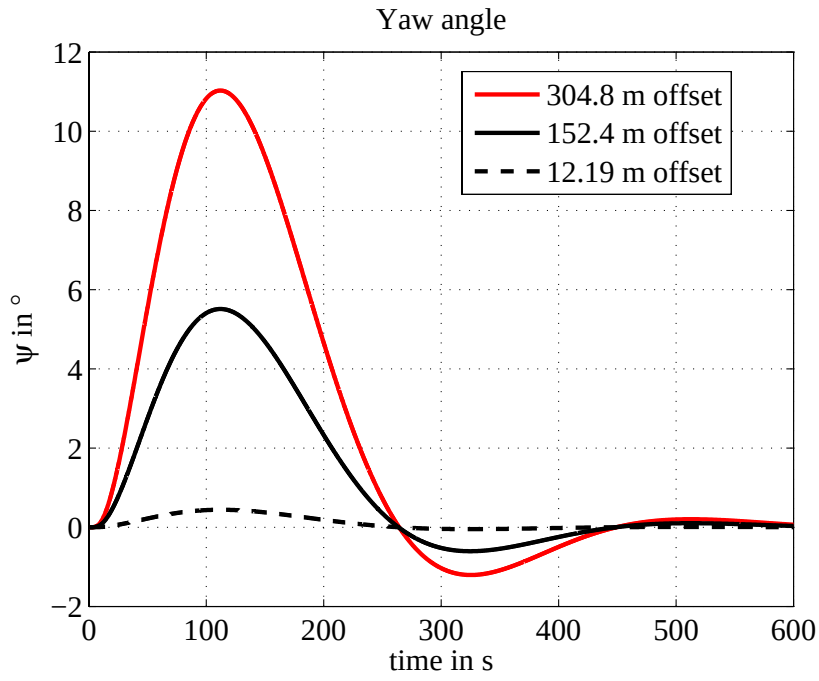

(a) Yaw angle history

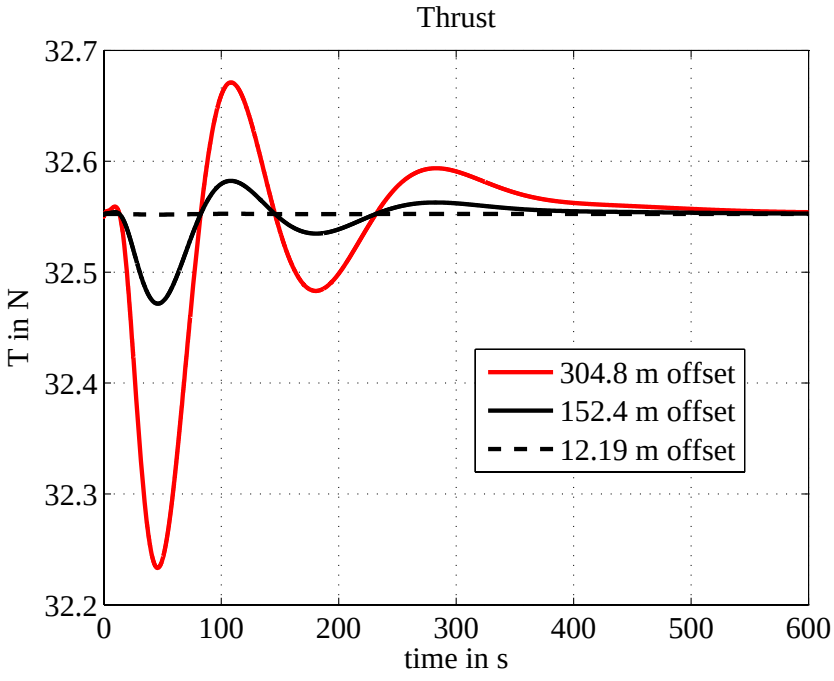

(b) Thrust history

Figure 5.34: Straight and level path with initial lateral offset (large offsets)

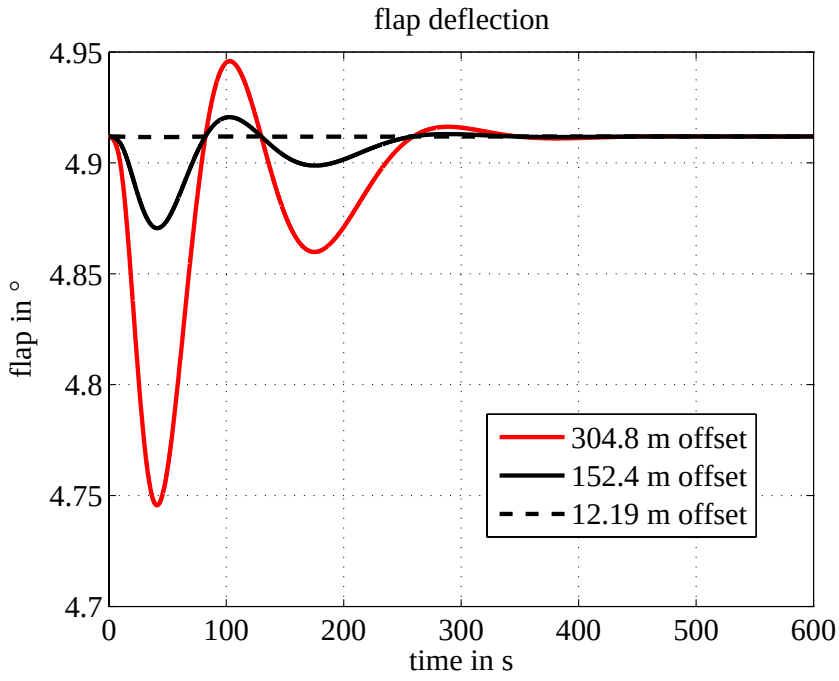

(a) Flap history

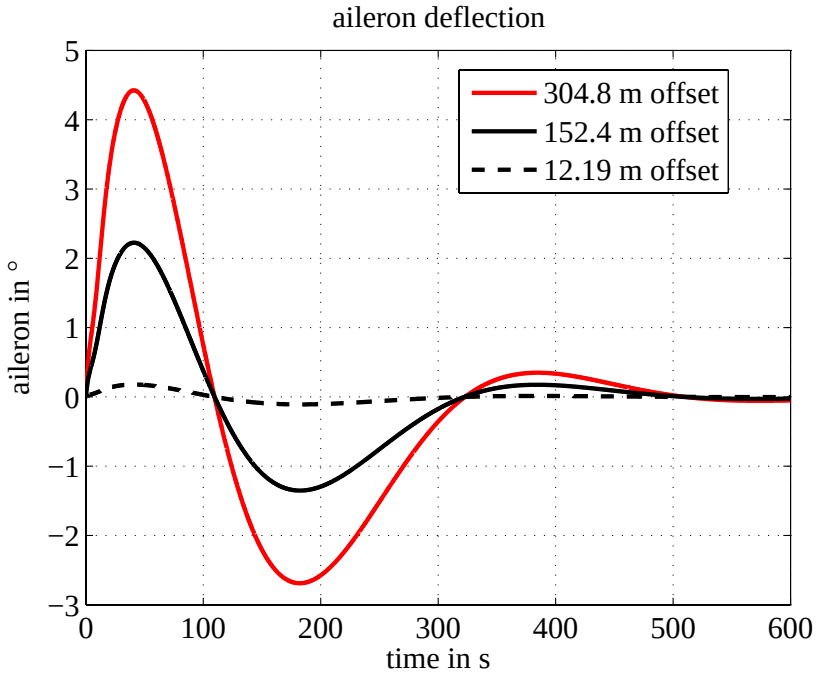

(b) Aileron history

Figure 5.35: Straight and level path with initial lateral offset (large offsets)

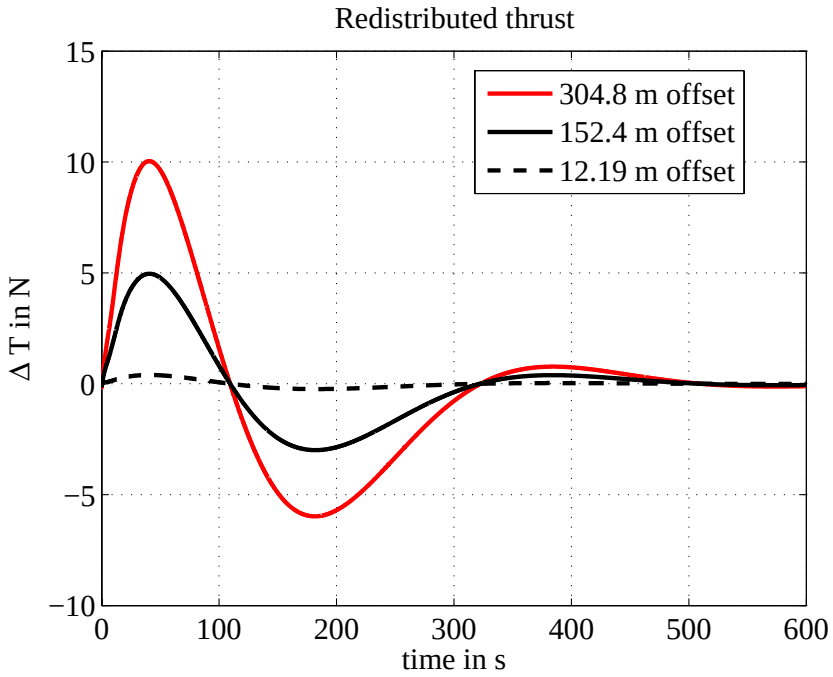

Figure 5.36: Straight and level path with initial lateral offset (large offsets)

Path following for curved ground flight

The next set of simulations studies the variation of closed loop response for turning flight with decreasing turn radius. The initial position of the flying wing is chosen to be at the origin of the inertial reference frame, and it is commanded to track a circle of a given radius while maintaining its altitude. For a given turn radius R, the origin of the circle to be tracked is chosen to be at $(R, 0, 0)$ m in the inertial frame. Figs. 5.37-5.41 show states and control inputs for turn radii of 6096 m, 4572 m and 3048 m.

Simulations show that the flying wing is able to successfully track circles of radii 6096 m and 4572 m, but is unable to track a circle of 3048 m. This limitation of the controller is explained by Fig. 5.41b. The plot shows the variation of ΔT with time, along with a plot of $-T/2$ for the 3048 m turn radius case. As $|\Delta T|$ reaches $T/2$, the thrust at one of the outboard engines goes to zero, and yaw control saturates. The simulation is terminated when T reaches zero. This saturation does not occur for the other two

cases, and the flying wing is able to successfully follow the corresponding ground paths. For the cases corresponding to the two larger radii, ΔR and altitude go to zero as the transients die down, and aileron deflection, ΔT and roll angle converge to a non-zero value corresponding to the equilibrium for turning flight.

In order to overcome the inability of the flying wing to turn with a radius of 3048 m, the initial position of the flying wing is moved to $(0, -L_1, 0)$ m, where L_1 is the lookforward distance of the guidance law. This change in initial position tells the controller of the circular path to be followed before the flying wing actually reaches the origin of the inertial XY plane, which is a point on the circular path. With this change, the flying wing is able to successfully follow a circle of radius 3048 m as seen from Figs. 5.42-5.46. However, when the radius is decreased to 1524 m, the flying wing is no longer able to follow the corresponding circular ground path as the yaw control saturates as seen in Fig. 5.46b.

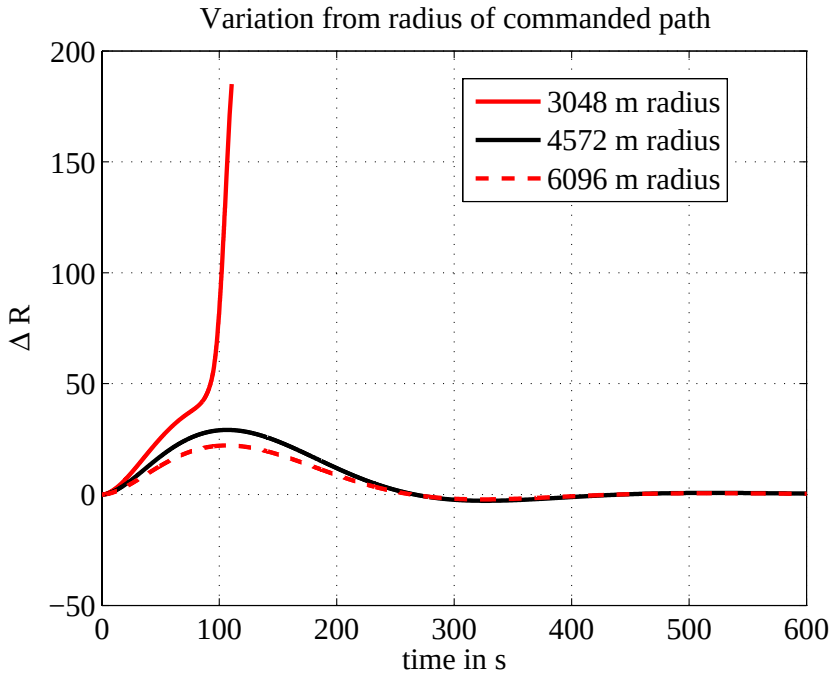

(a) Δ R history

Figure 5.37: Curved ground path with no initial offset (small radii)

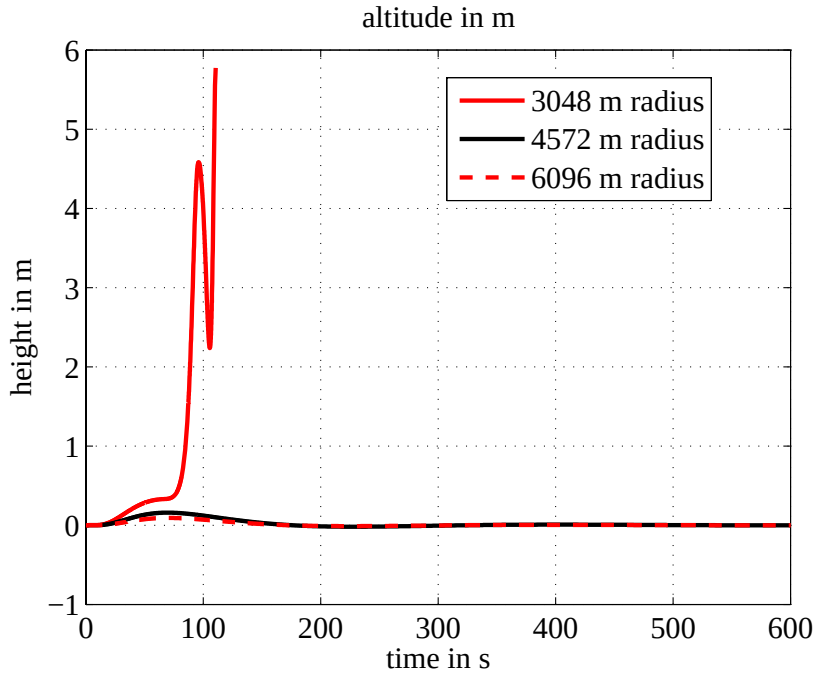

(a) Altitude history

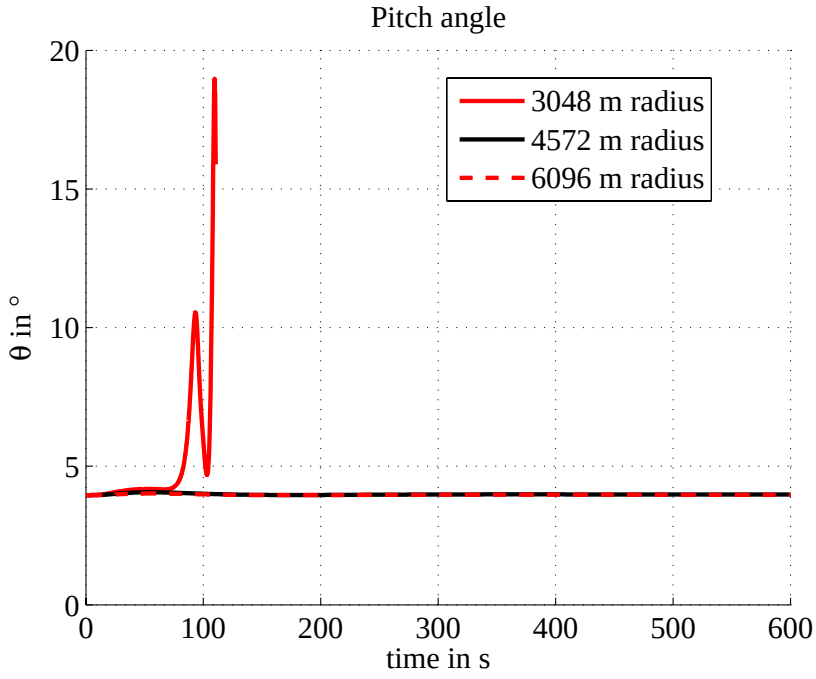

(b) Pitch angle history

Figure 5.38: Curved ground path with no initial offset (small radii)

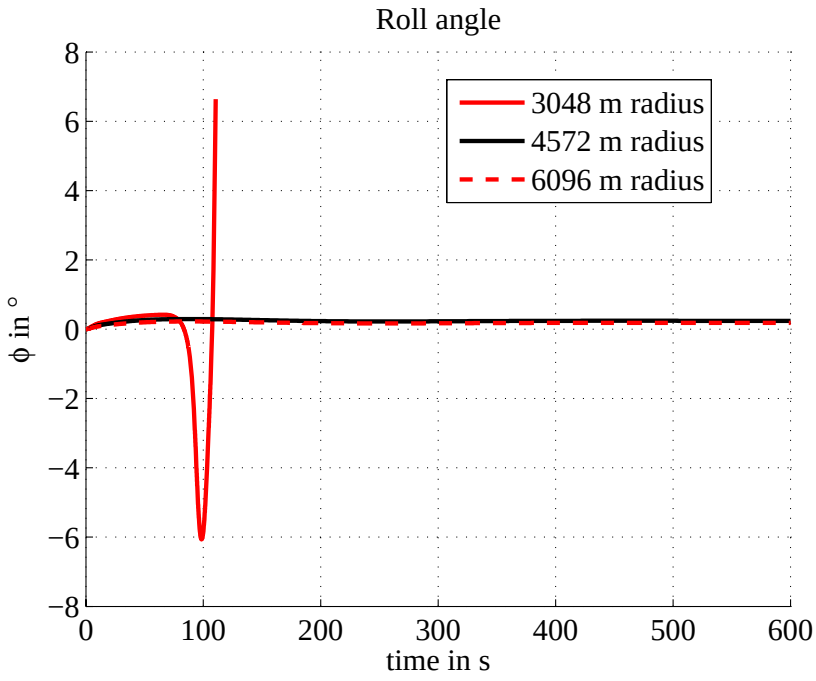

(a) Roll angle history

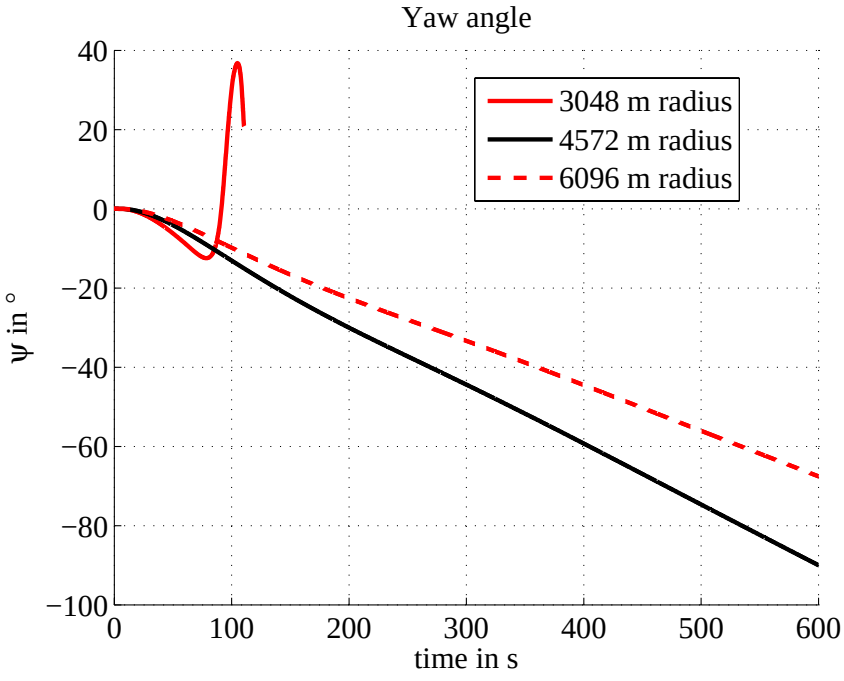

(b) Yaw angle history

Figure 5.39: Curved ground path with no initial offset (small radii)

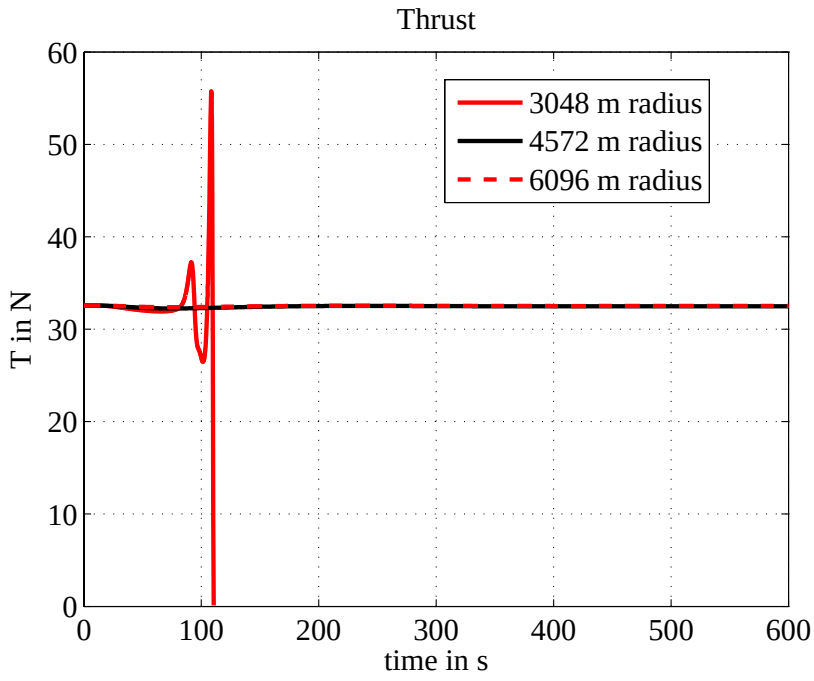

(a) Thrust history

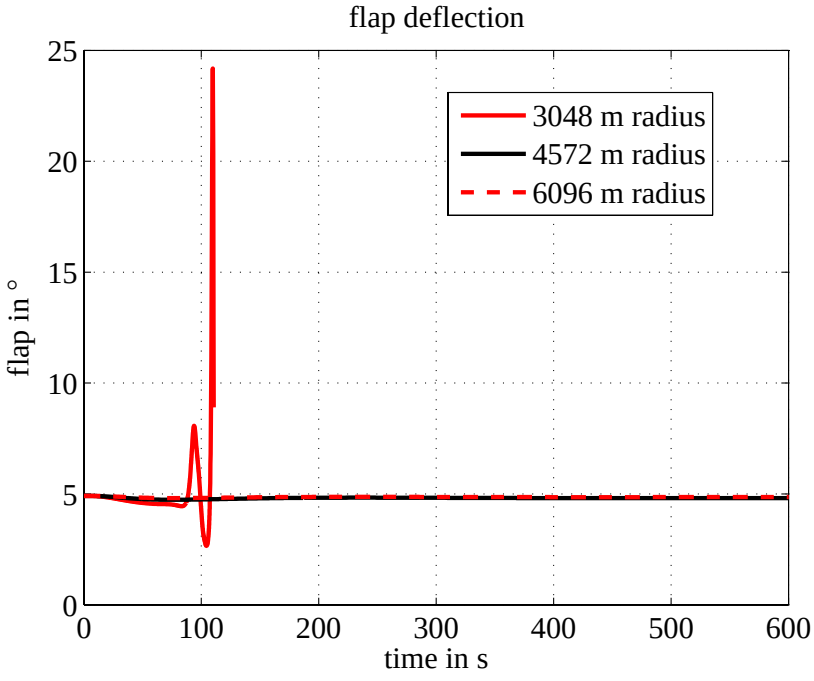

(b) Flap history

Figure 5.40: Curved ground path with no initial offset (small radii)

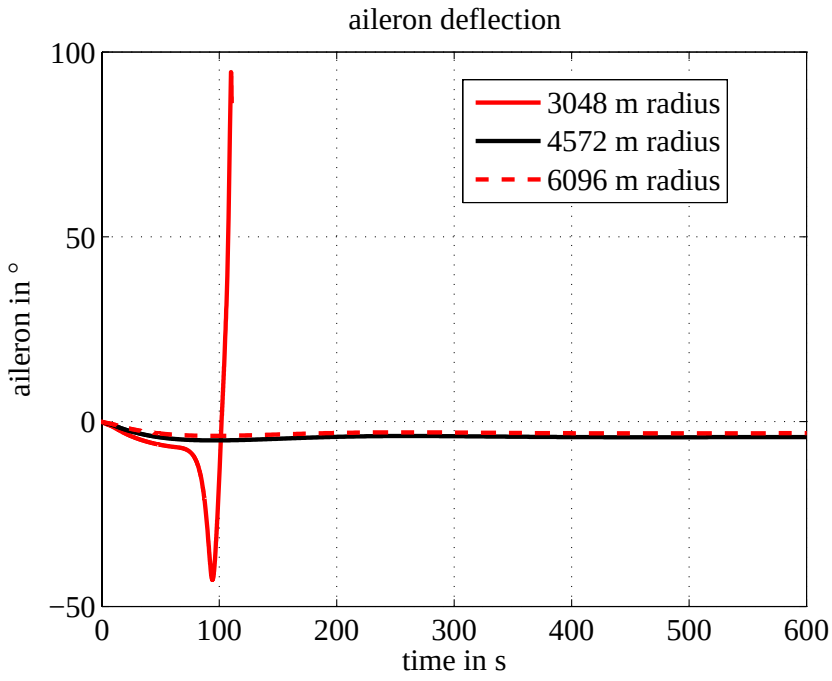

(a) Aileron history

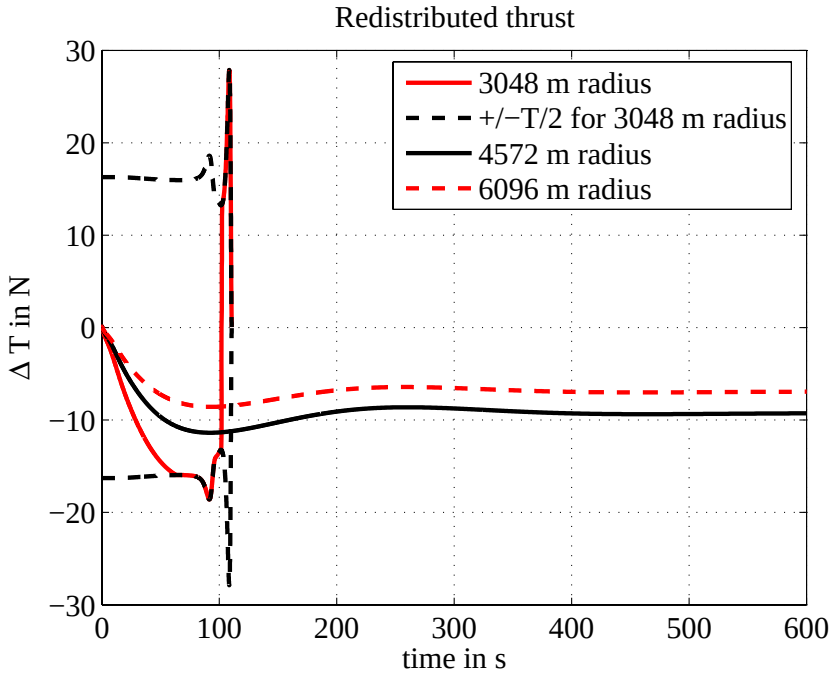

(b) Δ Thrust history

Figure 5.41: Curved ground path with no initial offset (small radii)

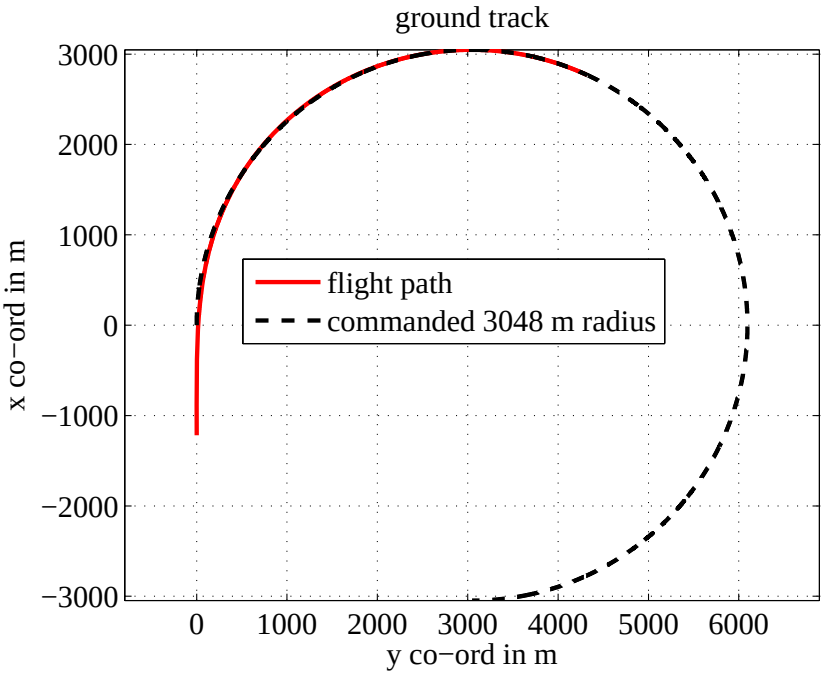

(a) Ground track history

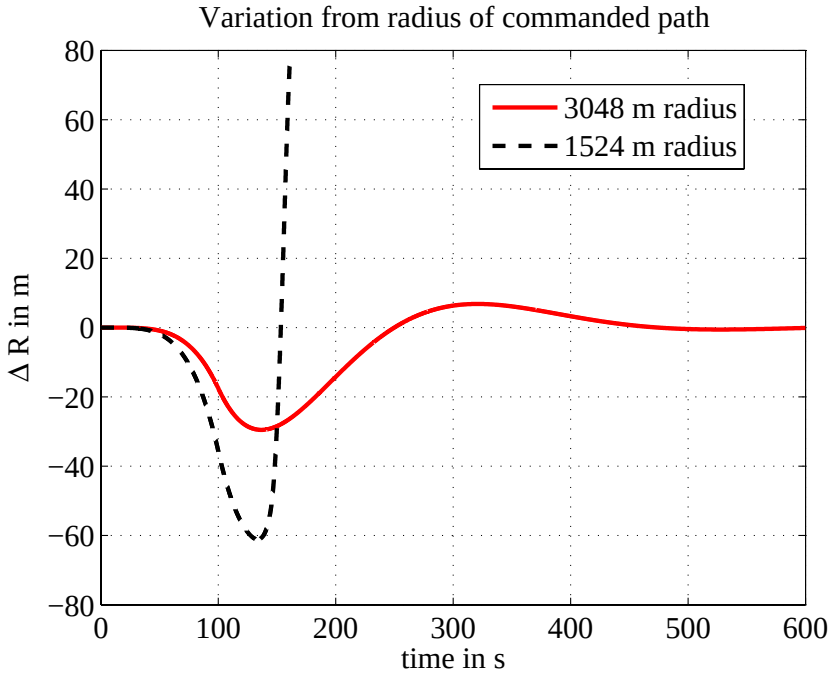

(b) Δ R history

Figure 5.42: Curved ground path with no initial offset (guidance law activated early)

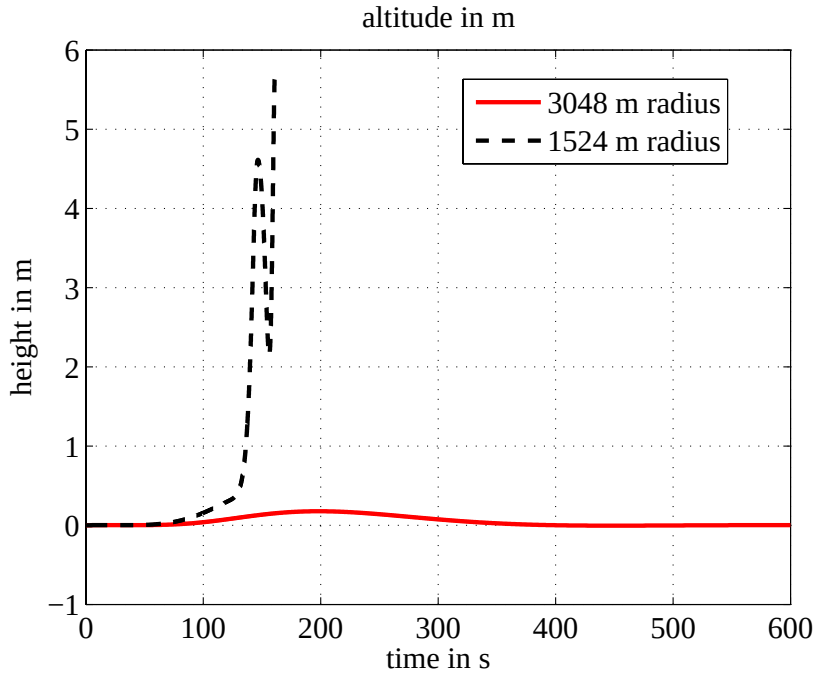

(a) Altitude history

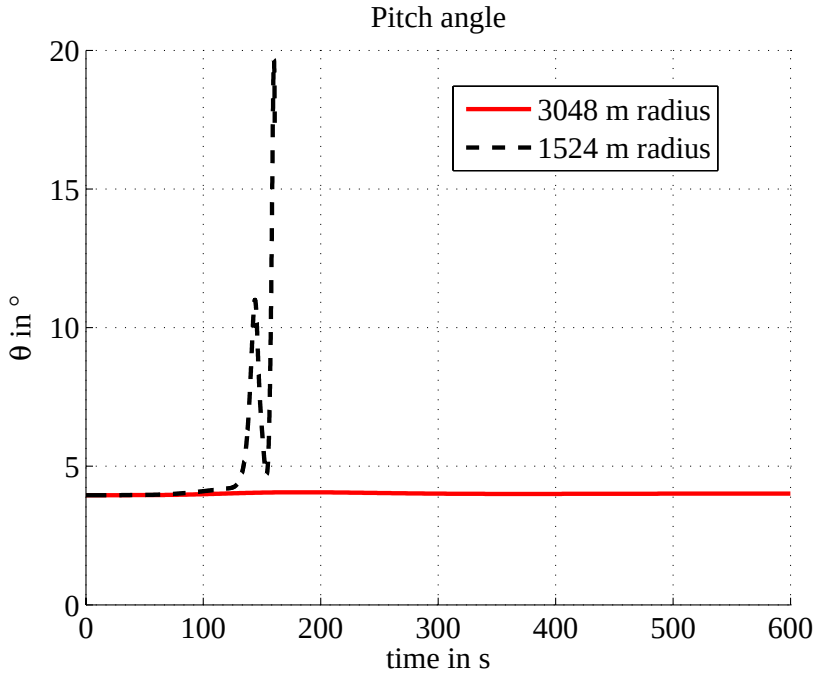

(b) Pitch angle history

Figure 5.43: Curved ground path with no initial offset (guidance law activated early)

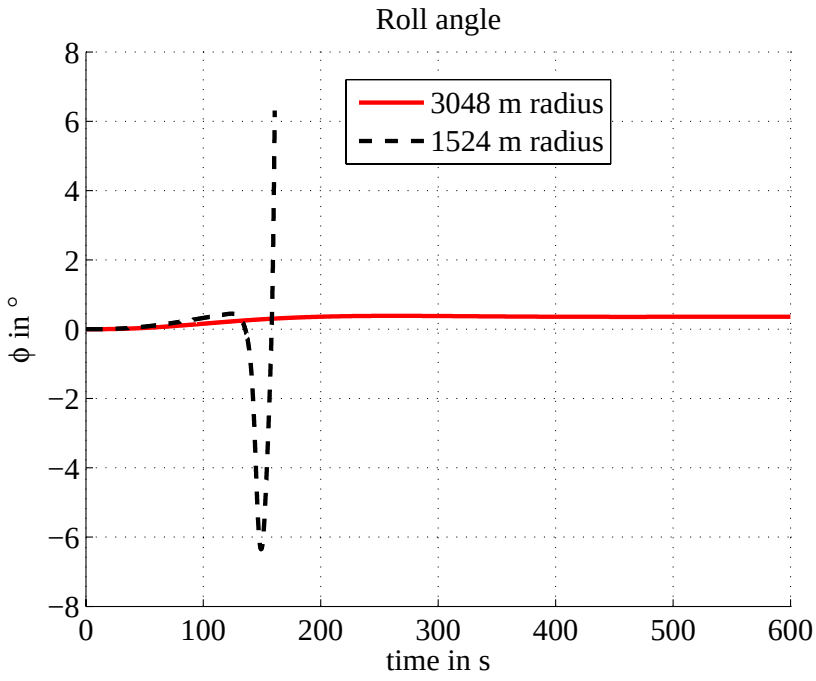

(a) Roll angle history

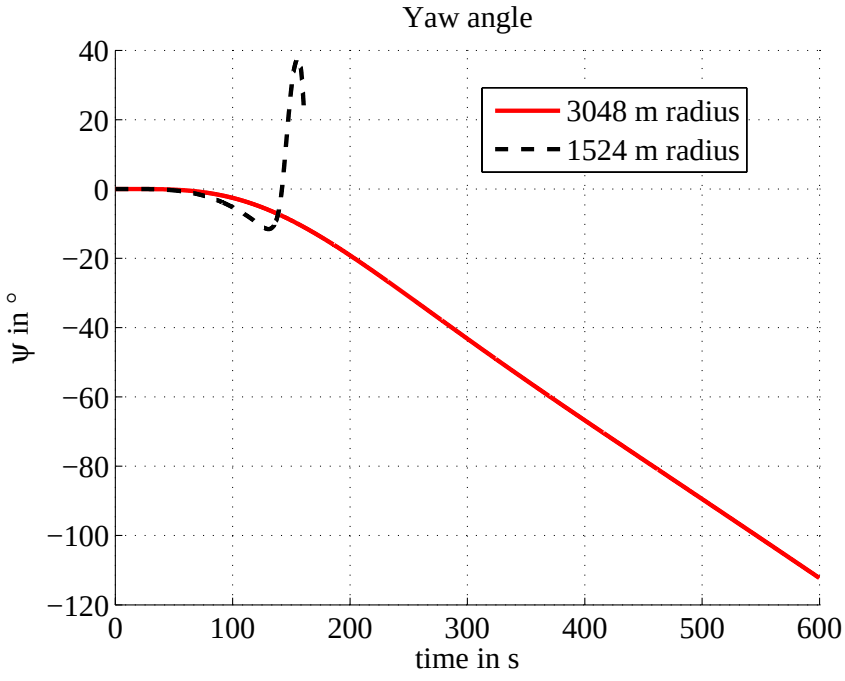

(b) Yaw angle history

Figure 5.44: Curved ground path with no initial offset (guidance law activated early)

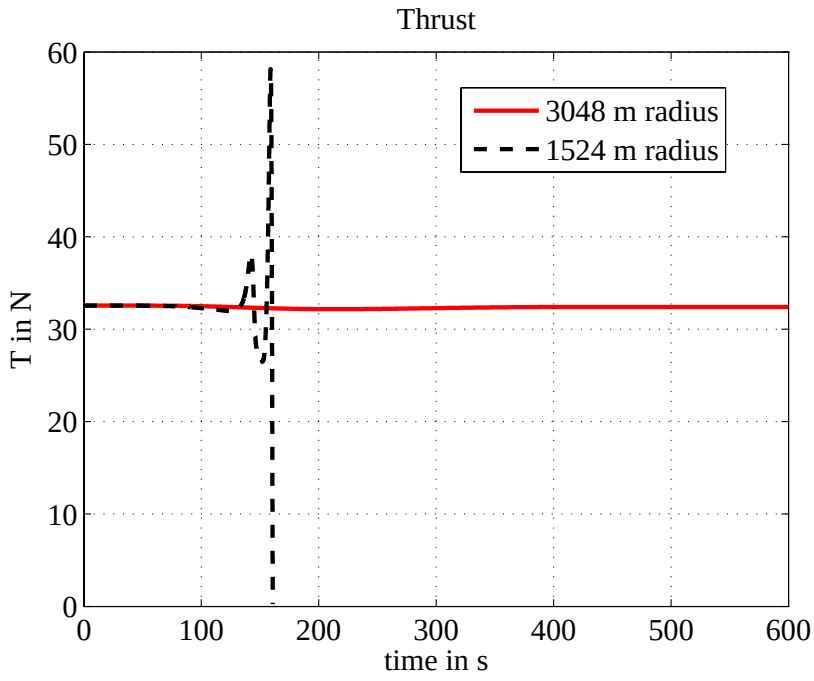

(a) Thrust history

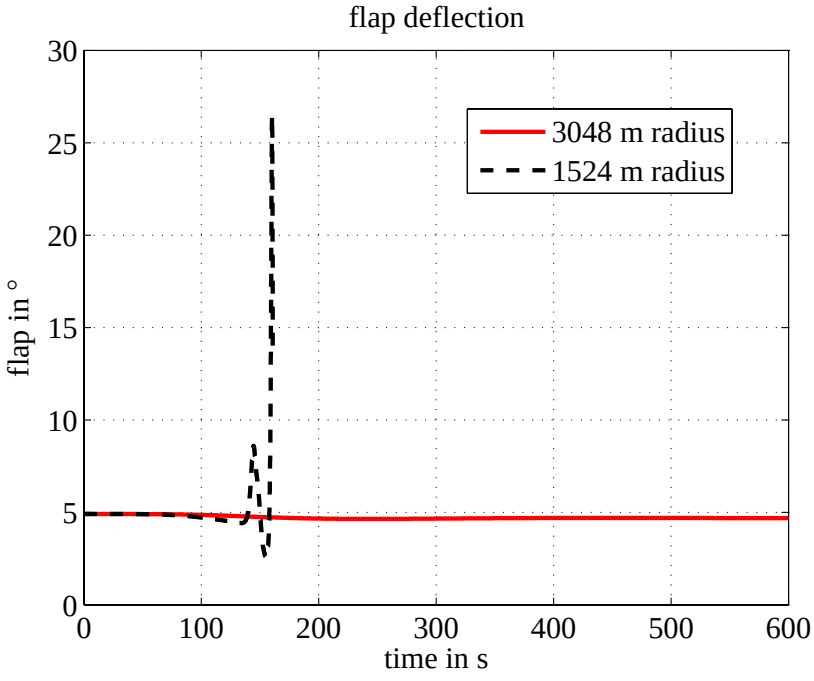

(b) Flap history

Figure 5.45: Curved ground path with no initial offset (guidance law activated early)

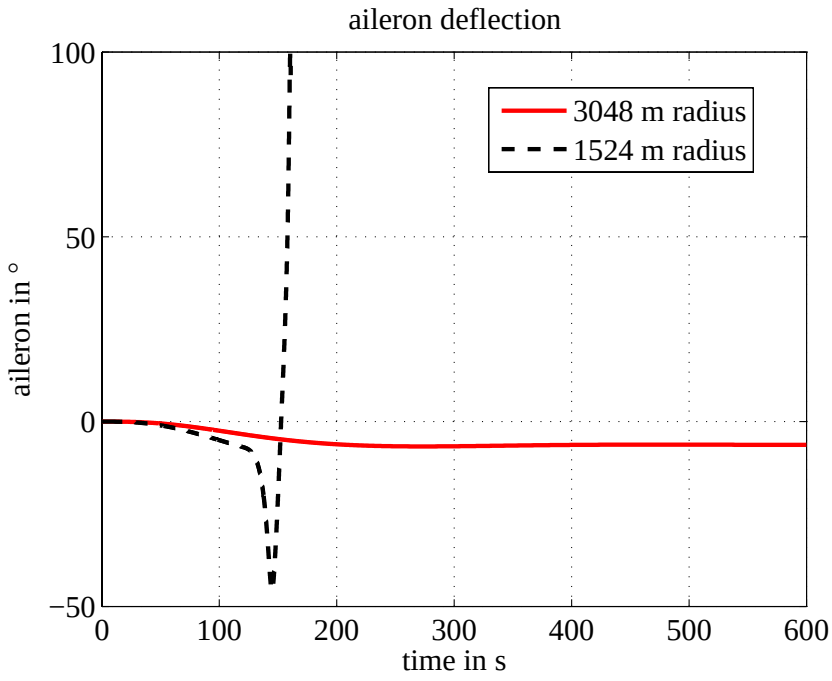

(a) Aileron history

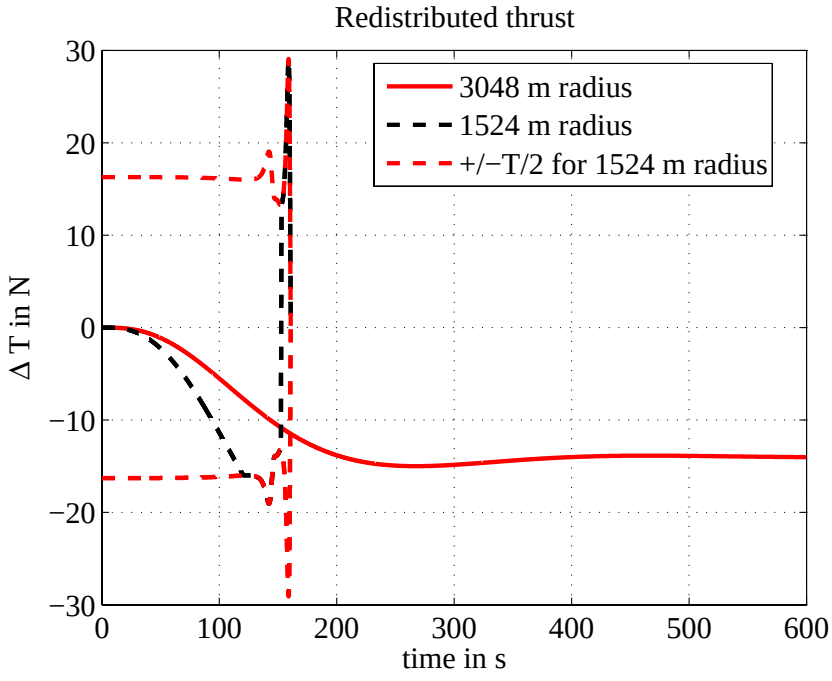

(b) Δ Thrust history

Figure 5.46: Curved ground path with no initial offset (guidance law activated early)

5.3.4 Path-following with abrupt change in payload mass

This set of simulations involves an abrupt change in the payload mass carried by the flexible flying wing. The airplane is trimmed in straight and level flight at 12.19 m/s at the origin of the inertial reference frame with the velocity vector along the inertial Y axis and is commanded to maintain its heading and altitude. The initial payload at the center of the flying wing is set as 181.4 kg (corresponding to the 'heavy' case). At $t = 50$ s, the payload is decreased abruptly. The three cases considered correspond to a decrease in payload by 50% and 25% respectively and are plotted in Figs. 5.47-5.49.

The change in payload mass also results in an abrupt change in the equilibrium aeroelastic state vector. Simulations show that the controller is able to control the transients due to the abrupt change in payload mass and drive the states to the new equilibrium condition. The change in payload mass causes the altitude to increase initially due a drop in the mass of the airplane as shown in Fig. 5.47b. The altitude of the airplane then decreases before coming back to its initial value. Once again, the transient flap response exhibits high frequency oscillations due to coupling with bending modes. The magnitude of the transient response is shown to increase with an increase in the change in the payload mass.

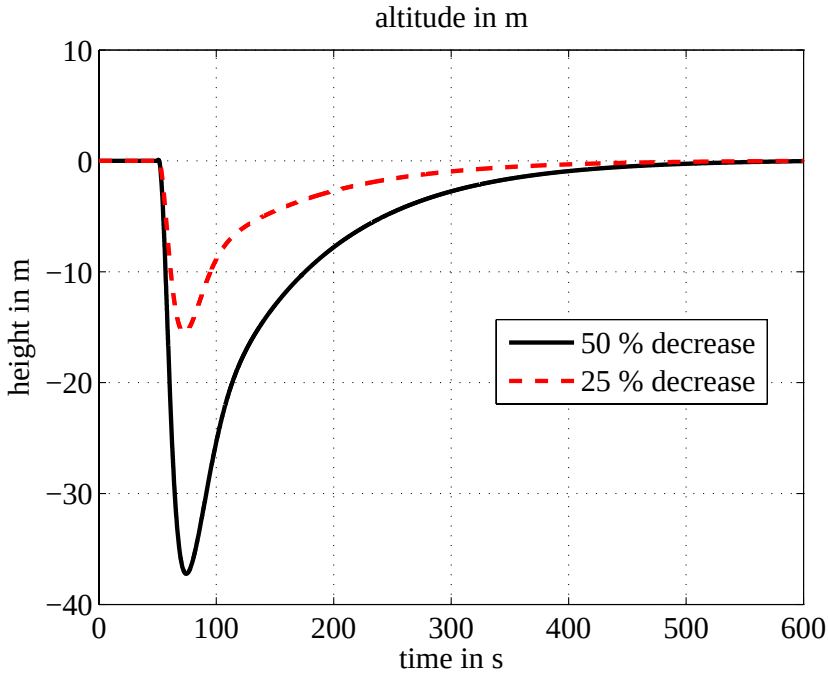

(a) Altitude history

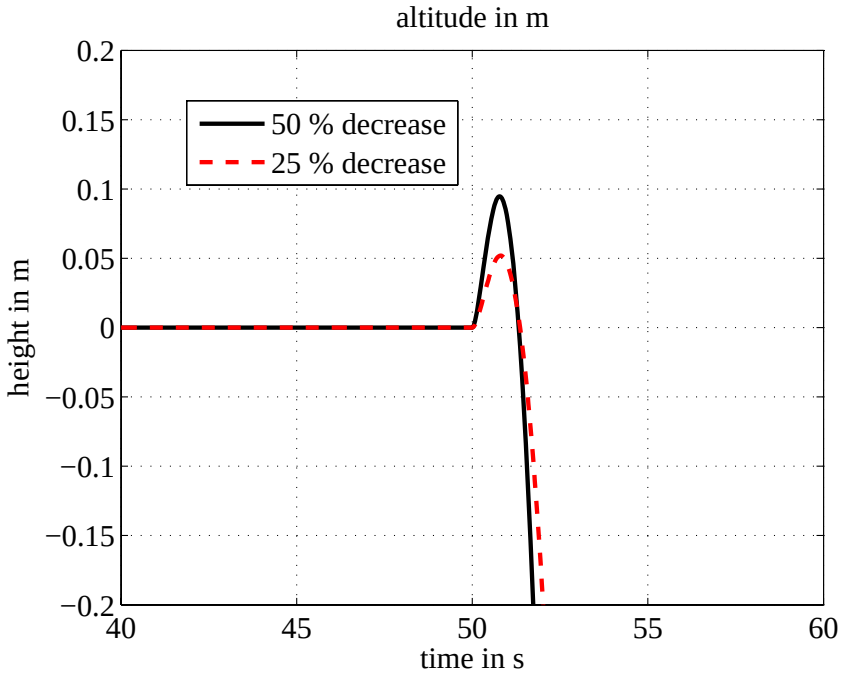

(b) Altitude history showing detail at $t = 50$s

Figure 5.47: Path following with abrupt change in payload mass

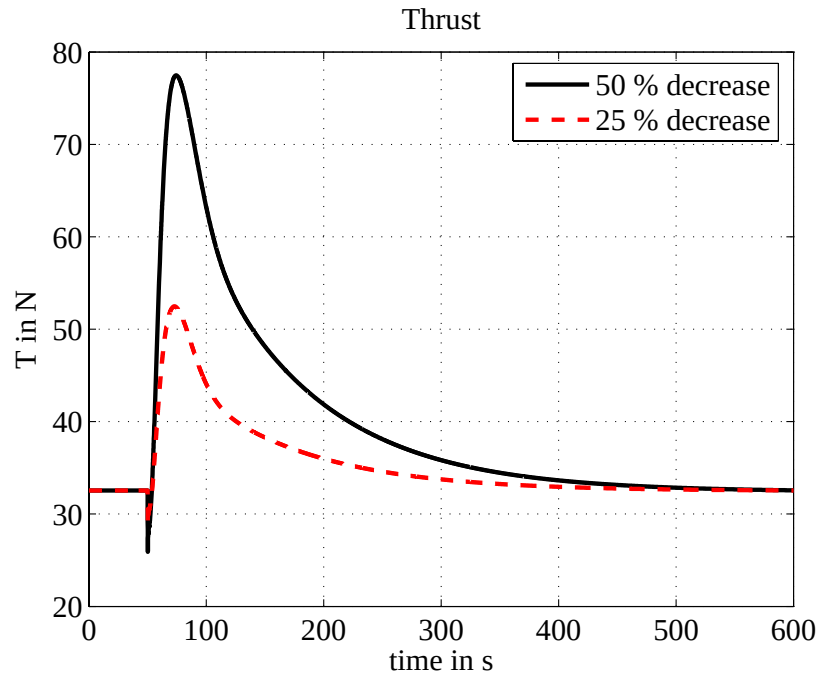

(a) Thrust history

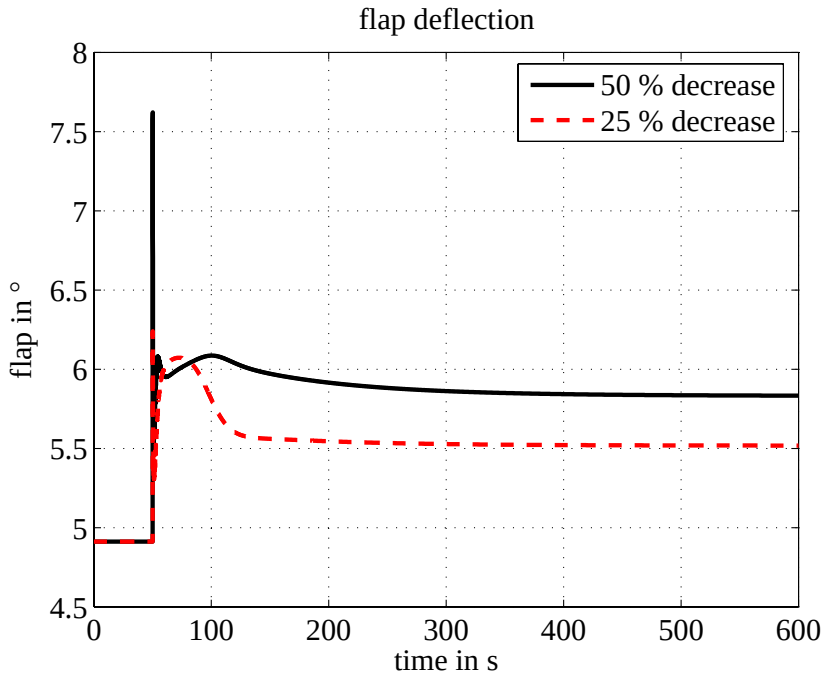

(b) Flap history

Figure 5.48: Path following with abrupt change in payload mass

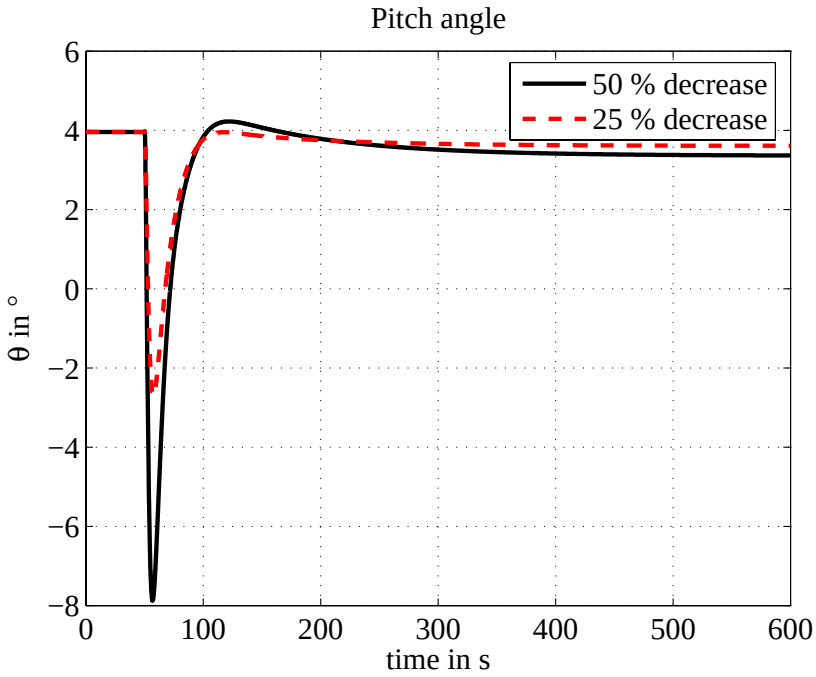

(a) Pitch angle history

Figure 5.49: Path following with abrupt change in payload mass

5.3.5 Dependence of computational time on discretization

Fig. 5.50 plots the variation of the log of the computational time in hours versus the log of the number of nodes on the flying wing. The number of nodes used in the simulation are 19, 25, 31, 37 and 43. The flying wing is commanded to maintain its heading and increase its altitude by 12.19 m. 30 s of flying time is simulated, which for a time-step of 0.02 s, corresponds to 1500 iterations. The simulations are carried out using MATLAB 7.6.0.324 on a Intel® Core™2 Quad CPU Q 9550 with 4 GB RAM and 32-bit Windows XP. The slope of the graph has a value of 1.3, which implies that the dependence of computational time on the number of nodes is close to linear.

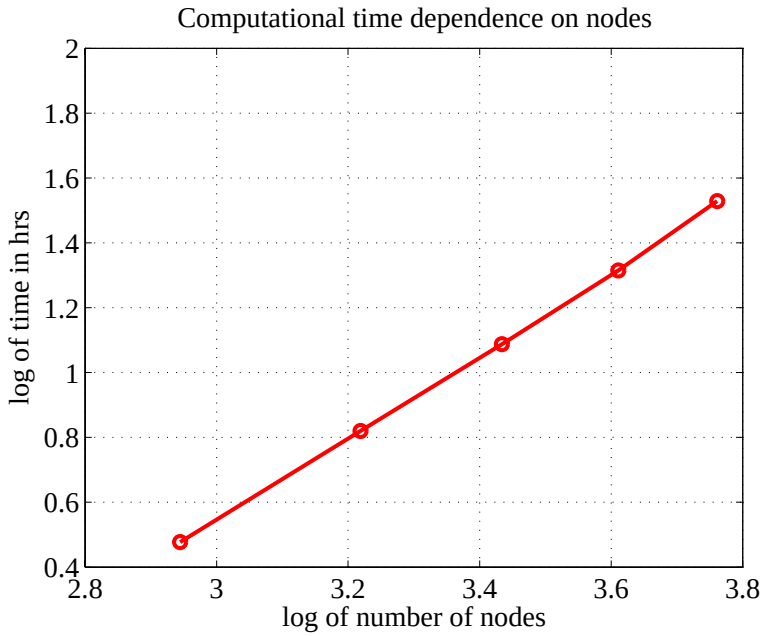

Figure 5.50: Variation of computational time with number of nodes

Chapter 6

Conclusions and Future Work

6.1 Conclusions

The objectives of this dissertation were to study the unique flight dynamic characteristics of flexible, high aspect-ratio flying wings and to design a flight control law for path-following. The flight dynamics was studied using an integrated model of the aeroelasticity and flight dynamics of flexible high aspect ratio flying wings developed by Patil and Hodges [7]. This includes analysis of lateral dynamics which was not studied by Patil and Hodges. It was found that a rigid body model that accounted for the static aeroelastic deformation at trim captured the predominant flight dynamic characteristics shown by the flexible flying wing. Moreover, this rigid body model was found to predict the onset of dynamic instability in the flight dynamics seen in the integrated model. A modified criteria was introduced for predicting the onset of static instability in the presence of large aeroelastic deformation.

Using the concept of the mean axis, a six degree-of-freedom reduced order model of the flight dynamics is constructed that minimizes the coupling between rigid body modes and the structural dynamics while accounting for the static aeroelastic deformation of

the flying wing. The original derivation of the equations of motion for a deformable airplane by Milne assumed small deformations [9]. This assumption is not made in the equations derived in this dissertation. Multi-step nonlinear dynamic inversion applied to this reduced order model is coupled with a nonlinear guidance law to design a flight controller for path following. The controls computed by this flight controller are used as inputs to a time-marching simulation of the integrated model of aeroelasticity and flight dynamics. Simulation results presented in this dissertation show that the controller is able to successfully follow both straight line and curved ground paths while maintaining the desired altitude. The controller is also shown to be able to handle an abrupt change in payload mass while path-following.

Finally, the equations of motion of the integrated model were non-dimensionalized to identify aeroelastic parameters for optimization and design of high aspect-ratio flying wings.

6.2 Future Work

Though the concept of a controller for a flexible, high aspect-ratio flying wing has been proven in this dissertation, further work needs to be done before this system can be implemented on an actual airplane. Some of the questions that need to be addressed are listed below:

- The aeroelastic model used for linear stability analysis and time-marching simulation needs to be validated with experimental data. This data is not publicly available at this point in time.
- The controller used in this dissertation takes the velocities and angular velocities of nodes from the simulation as inputs for computing mean axis parameters. In a real system, these quantities will have to be estimated as shown in Section 4.6. The

effect of this state estimation on the closed loop system needs to be addressed.

- The controller needs to be augmented for gust load alleviation and its effect on the complete closed-loop system needs to be studied.

- Actuator dynamics are not modeled in this dissertation, and the effect of these dynamics on both the aeroelasticity and flight dynamics needs to be studied.

- The configuration used to study open loop dynamics was found to be subject to control reversal. This was overcome by increasing the torsional rigidity of the configuration for closed loop simulations. However, the effect of static aeroelasticity on the effectiveness of tailing edge control surfaces and its implications for flight control needs to be studied in detail and accounted for in control design.

- The controller design implemented in this dissertation assumes that model used by the controller is known exactly. As this will not be the case in a real system, the robustness of the controller with respect to uncertainties in the model needs to be studied.

Bibliography

[1] "NASA - NASA Dryden Fact Sheet - Solar-Power Research," http://www.nasa.gov/centers/dryden/news/FactSheets/FS-054-DFRC.html.

[2] Noll, T. E., Brown, J. M., Perez-Davis, M. E., Ishmael, S. D., Tiffany, G. E., and Gaier, M., "Investigation of the Helios Prototype Aircraft Mishap," Tech. rep., NASA, 2004.

[3] DARPA, "Vulture Program: Broad Agency Announcement Solicitation 07-51," July 2007.

[4] "DARPA-Vulture Program," http://www.darpa.mil/news_images/vulture-01.html.

[5] "DARPA-Vulture Program," http://www.darpa.mil/news_images/vulture-02.html.

[6] "DARPA-Vulture Program," http://www.darpa.mil/news_images/vulture-03.html.

[7] Patil, M. J. and Hodges, D. H., "Flight Dynamics of Highly Flexible Flying Wings," *Journal of Aircraft*, Vol. 43, No. 6, Nov. – Dec. 2006, pp. 1790 – 1798.

[8] Skoog, R. B., "An Analysis of the Effects of Aeroelasticity on Static Longitudinal Stability and Control of a Swept Wing Airplane," Tech. Rep. 1298, NACA, Jan. 1957.

[9] Milne, R. D., "Dynamcis of the Deformable Aeroplane," R&M 3345, British Aeronautical Research Council, 1964.

[10] Milne, R. D., "Some Remarks on the Dynamcis of Deformable Bodies," *AIAA Journal*, Vol. 6, No. 3, Mar. 1968, pp. 556 – 558.

[11] Wykes, J. H. and Lawrence, R. E., "Aerothermoelasticity: Its Impact on Stability and Control of Winged Aerospace Vehicles," *Journal of Aircraft*, Vol. 2, No. 6, Nov. – Dec. 1965, pp. 517 – 526.

[12] Rodden, W. P., "Dihedral Effect of a Flexible Wing," *Journal of Aircraft*, Vol. 2, No. 5, Sep. – Oct. 1965, pp. 368 – 373.

[13] Swaim, R. L. and Fullman, D. G., "Prediction of Elastic-Airplane Longitudinal Dynamics from Rigid-Body Aerodynamics," *Journal of Aircraft*, Vol. 14, No. 9, Sep. 1977, pp. 868 – 873.

[14] Swaim, R. L. and Staab, G. H., "Prediction of Elastic-Airplane Lateral Dynamics from Rigid-Body Aerodynamics," *Journal of Aircraft*, Vol. 15, No. 7, Jul. 1978, pp. 392 – 398.

[15] Weisshaar, T. A. and Ashley, H., "Static Aeroelasticity and the Flying Wing," *Journal of Aircraft*, Vol. 10, No. 10, Oct. 1973, pp. 586 – 594.

[16] Weisshaar, T. A. and Ashley, H., "Static Aeroelasticity and the Flying Wing, Revisited," *Journal of Aircraft*, Vol. 11, No. 11, Nov. 1974, pp. 718 – 720.

[17] Rodden, W. P. and Love, J. R., "Equations of Motion of a Quasisteady Flight Vehicle Utilizing Restrained Static Aeroelastic Characteristics," *Journal of Aircraft*, Vol. 22, No. 9, Sep. 1985, pp. 802 – 809.

[18] Dykman, J. R. and Rodden, W. P., "Structural Dynamics and Quasistatic Aeroelastic Equations of Motion," *Journal of Aircraft*, Vol. 37, No. 3, May – Jun. 2000, pp. 538 – 542.

[19] Karpel, M., "Reduced-Order Aeroelastic Models via Dynamic Residualization," *Journal of Aircraft*, Vol. 27, No. 5, May 1990, pp. 449 – 455.

[20] Waszak, M. R. and Schmidt, D. K., "Flight Dynamics of Aeroelastic Vehicles," *Journal of Aircraft*, Vol. 25, No. 6, Jun. 1988, pp. 563 – 571.

[21] Schmidt, D. K. and Raney, D. L., "Modeling and Simulation of Flexible Flight Vehicles," *Journal of Guidance, Control and Dynamics*, Vol. 24, No. 3, May – Jun. 2001, pp. 539 – 546.

[22] Newman, B. and Schmidt, D. K., "Numerical and Literal Aeroelastic-Vehicle-Model Reduction for Feedback Control Synthesis," *Journal of Guidance, Control and Dynamics*, Vol. 14, No. 5, Sep. – Oct. 1991, pp. 943 – 953.

[23] Livneh, R. and Schmidt, D. K., "Unified Literal Approximations for Longitudinal Dynamics of Flexible Flight Vehicles," *Journal of Guidance, Control and Dynamics*, Vol. 18, No. 5, Sep. – Oct. 1995, pp. 1074 – 1083.

[24] Siepenkotter, A. and Alles, W., "Stability analysis of the nonlinear dynamics of flexible aircraft," *Aerospace Science and Technology*, Vol. 9, No. 2, Mar. 2005, pp. 135 – 141.

[25] Buttrill, C. S., Zeiler, T. A., and Arbuckle, P. D., "Nonlinear Simulation of a Flexible Aircraft in Maneuvering Flight," *Proceedings of the AIAA Flight Simulation Technologies Conference*, Monterey, CA, August 1987, AIAA-1987-2501.

[26] Drela, M., "Integrated Simulation Model for Preliminary Aerodynamic, Structural, and Control-law Design of Aircraft," *Proceedings of the 40th AIAA/ASME/ASCE/AHS/ASC Structures, Structural Dynamics, and Materials Conference*, St. Louis, MO, April 1999, AIAA-1999-1394.

[27] Winther, B. A., Goggin, P. J., and Dykman, J. R., "Reduced-Order Dynamic Aeroelastic Model Development and Integration with Nonlinear Simulation," *Journal of Aircraft*, Vol. 37, No. 5, Sep. – Oct. 2000, pp. 833 – 839.

[28] Reschke, C., *Integrated Flight Loads Modelling and Analysis for Flexible Transport Aircraft*, Ph.D. thesis, University of Stuttgart, Sturrgart, Germany, July 2006.

[29] Nguyen, N., "Integrated Flight Dynamic Modeling of Flexible Aircraft with Inertial Force-Propulsion-Aeroelastic Coupling," *Proceedings of the 46th AIAA Aerospace Sciences Meeting and Exhibit*, Reno, NV, January 2008, AIAA-2008-194.

[30] Freymann, R., "Dynamic Interactions between Active Control Systems and a Flexible Aircraft Structure," *Proceedings of the 27th Structures, Structural Dynamics and Materials Conference*, San Antonio, TX, May 1986, AIAA-1986-0960.

[31] Kubica, F., Livet, T., Le Tron, X., and Bucharles, A., "Parameter-Robust Flight Control System for a Flexible Aircraft," *Control Engineering Practice*, Vol. 3, No. 9, Sep. 1995, pp. 1209 – 1215.

[32] Becker, J., Caldwell, B., and Vaccaro, V., "The Interaction of Flight Control System and Aircraft Structure," *Proceedings of the RTO AVT Specialists' Meeting on 'Structural Aspects of Flexible Aircraft Control'*, Ottawa, Cananda, October 1999, 4.

[33] van Etten, C., Balas, G. J., and Bennani, S., "Linear Parametrically Varying Integrated Flight and Structural Mode Control for a Flexible Aircraft," *Proceedings of the AIAA Guidance, Navigation, and Control Conference and Exhibit*, Portland, OR, August 1999, AIAA-1999-4217.

[34] Miyazawa, Y., "Flight Control Law and Structural Filter Design for a Flexible Aerospace Vehicle," *Proceedings of the AIAA Guidance, Navigation, and Control Conference and Exhibit*, Denver, CO, August 2000, AIAA-2000-4256.

[35] Alazard, D., "Robust H2 Design for Lateral Flight Control of Highly Flexible Aircraft," *Journal of Guidance, Control and Dynamics*, Vol. 25, No. 3, May – Jun. 2002, pp. 502 – 509.

[36] Goman, M., Sidoryuk, M., and Ustinov, A., "Control Law Design for Flexible Aircraft: Comparison of the H_∞-based and Classical Methods," *Proceedings of the AIAA Guidance, Navigation, and Control Conference and Exhibit*, San Francisco, CA, August 2005, AIAA-2005-6265.

[37] Silvestre, F. and Paglione, P., "Dynamics and Control of a Flexible Aircraft," *Proceedings of the AIAA Atmospheric Flight Mechanics Conference and Exhibit*, Honolulu, HI, August 2008, AIAA-2008-6876.

[38] Gregory, I. M., "Dynamic Inversion to Control Large Flexible Aircraft," *Proceedings of the AIAA Guidance, Navigation, and Control Conference and Exhibit*, Boston, MA, 1998, AIAA-1998-4323.

[39] Gregory, I. M., "Modified Dynamic Inversion to Control Large Flexible Aircraft - What's Going On?" *Proceedings of the AIAA Guidance, Navigation, and Control Conference and Exhibit*, Portland, OR, 1999, AIAA-1999-3998.

[40] Gregory, I. M., "Stability Result for Dynamic Inversion Devised to Control Large Flexible Aircraft," *Proceedings of the AIAA Guidance, Navigation, and Control Conference and Exhibit*, Montreal, Canada, August 2001, AIAA-2001-4284.

[41] Meirovitch, L. and Tuzcu, I., "Unified Theory for the Dynamics and Control of Maneuvering Flexible Aircraft," *AIAA Journal*, Vol. 42, No. 4, Apr. 2004, pp. 714 – 727.

[42] Meirovitch, L. and Tuzcu, I., "Time Simulations of the Response of Maneuvering Flexible Aircraft," *Journal of Guidance, Control and Dynamics*, Vol. 27, No. 5, Sep. – Oct. 2004, pp. 814 – 828.

[43] Tuzcu, I. and Meirovitch, L., "Effects of Flexibility on the Stability of Flying Aircraft," *Journal of Dynamic Systems, Measurement, and Control*, Vol. 127, No. 1, Mar. 2005, pp. 41 – 49.

[44] Meirovitch, L. and Tuzcu, I., "Control of Flexible Aircraft Executing Time-Dependent Maneuvers," *Journal of Guidance, Control and Dynamics*, Vol. 28, No. 6, Nov. – Dec. 2005, pp. 1291 – 1300.

[45] Patil, M. J., Hodges, D. H., and Cesnik, C. E. S., "Characterizing the Effects of Geometrical Nonlinearities on Aeroelastic Behavior of High-Aspect-Ratio Wings," *Proceedings of the International Forum on Aeroelasticity and Structural Dynamics*, Williamsburg, VA, June 1999.

[46] Frulla, G., "Aeroelastic behaviour of a solar-powered high-altitude long endurance unmanned air vehicle (UAV) slender wing," *Proceedings of the I MECH E Part G Journal of Aerospace Engineering*, Vol. 218, No. 3, 2004, pp. 179 – 188.

[47] Patil, M. J. and Hodges, D. H., "On the importance of aerodynamic and structural geometrical nonlinearities in aeroelastic behavior of high-aspect-ratio wings," *Journal of Fluids and Structures*, Vol. 19, No. 7, Aug. 2004, pp. 905 – 915.

[48] Patil, M. J., Hodges, D. H., and Cesnik, C. E. S., "Nonlinear Aeroelastic Ananlysis of Complete Aircraft in Subsonic Flow," *Journal of Aircraft*, Vol. 37, No. 5, Sep. – Oct. 2000, pp. 753 – 760.

[49] Patil, M. J., Hodges, D. H., and Cesnik, C. E. S., "Limit-Cycle Oscillations in High-Aspect-Ratio Wings," *Journal of Fluids and Structures*, Vol. 15, No. 1, Jan. 2001, pp. 107 – 132.

[50] Tang, D. and Dowell, E. H., "Effects of geometric structural nonlinearity on flutter and limit cycle oscillations of high-aspect-ratio wings," *Journal of Fluids and Structures*, Vol. 19, No. 3, Apr. 2004, pp. 291 – 306.

[51] Tang, D. and Dowell, E. H., "Experimental and Theoretical Study on Aeroelastic Response for High-Aspect-Ratio Wing," *AIAA Journal*, Vol. 39, No. 8, Aug. 2001, pp. 1430 – 1441.

[52] Tang, D. and Dowell, E. H., "Limit-Cycle Hysteresis Response for a High-Aspect-Ratio Wing Model," *Journal of Aircraft*, Vol. 39, No. 5, Sep. – Oct. 2002, pp. 885 – 888.

[53] Romeo, G., Frulla, G., Cestino, E., Marzocca, P., and Tuzcu, I., "Non-Linear Aeroelastic Modeling and Experiments of Flexible Wings," *Proceedings of the 47th AIAA/ASME/ASCE/AHS/ASC Structures, Structural Dynamics, and Materials Conference*, Newport, RI, May 2006, AIAA-2006-2186.

[54] Patil, M. J. and Hodges, D. H., "Output Feedback Control of the Nonlinear Aeroelastic Response of a Slender Wing," *Journal of Guidance, Control and Dynamics*, Vol. 25, No. 2, Mar. – Apr. 2002, pp. 302 – 308.

[55] Cesnik, C. E. S. and Brown, E. L., "Modeling of High Aspect Ratio Active Flexible Wings for Roll Control," *Proceedings of the 43rd AIAA/ASME/ASCE/AHS/ASC Structures, Structural Dynamics, and Materials Conference*, Denver, CO, April 2002, AIAA-2002-1719.

[56] Su, W. and Cesnik, C. E. S., "Nonlinear Aeroelastic Modeling and Analysis of Fully Flexible Aircraft," *Proceedings of the 46th AIAA/ASME/ASCE/AHS/ASC Structures, Structural Dynamics, and Materials Conference*, Austin, TX, April 2005, AIAA-2005-2169.

[57] Smith, M. J., Patil, M. J., and Hodges, D. H., "CFD-Based Analysis of Nonlinear Aeroelastic Behavior of High-Aspect-Ratio Wings," *Proceedings of the 42nd AIAA/ASME/ASCE/AHS/ASC Structures, Structural Dynamics, and Materials Conference*, Seattle, WA, April 2001, AIAA-2001-1582.

[58] Palacios, R. and Cesnik, C. E. S., "Static Nonlinear Aeroelasticity of Flexible Slender Wings in Compressible Flow," *Proceedings of the 46th AIAA/ASME/ASCE/AHS/ASC Structures, Structural Dynamics, and Materials Conference*, Austin, TX, April 2005, AIAA-2005-1945.

[59] Garcia, J. A., "Numerical Investigation of Nonlinear Aeroelastic Effects on Flexible High-Aspect-Ratio Wings," *Journal of Aircraft*, Vol. 42, No. 4, July – Aug. 2005, pp. 1025 – 1036.

[60] Vartio, E., Shimko, A., Tilmann, C. P., and Flick, P. M., "Structural Modal Control and Gust Load Alleviation for a SensorCraft Concept," *Proceedings of the 46th AIAA/ASME/ASCE/AHS/ASC Structures, Structural Dynamics, and Materials Conference*, Austin, TX, April 2005, AIAA-2005-1946.

[61] Vartio, E., Shaw, E., and Vetter, T., "Gust Load Alleviation Flight Control System Design fir a SensorCraft Vehicle," *Proceedings of the 26th AIAA Applied Aerodynamic Conference*, Honolulu, HI, August 2008, AIAA-2008-7192.

[62] Penning, K., Zink, P., Wei, P., De La Garza, A., Love, M., and Martinez, J., "GLA and Flutter Suppression for a SensorCraft Class Concept Using System Identification," *Proceedings of the 26th AIAA Applied Aerodynamics Conference*, Honolulu, HI, August 2008, AIAA-2008-7188.

[63] Gregory, I. M., Cao, C., Patel, V. V., and Hovakimyan, N., "Adaptive Control Laws for Flexible Semi-Span Wind Tunnel Model of High-Aspect Ratio Flying Wing," *Proceedings of the AIAA Guidance, Navigation, and Control Conference and Exhibit*, Hilton Head, SC, August 2007, AIAA-2007-6525.

[64] Banerjee, J. R., "Flutter Characteristics of High Aspect Ratio Tailless Aircraft," *Journal of Aircraft*, Vol. 21, No. 9, Sep. 1984, pp. 733 – 736.

[65] Banerjee, J. R., "Flutter Modes of High Aspect Ratio Tailless Aircraft," *Journal of Aircraft*, Vol. 25, No. 5, May 1988, pp. 473 – 476.

[66] Banerjee, J. R. and Cal, A. A., "A Unified Approach to Stability Characteristics of Tailless Aircraft," *In Proceedings of the 29th Structures, Structural Dynamics and Materials Conference*, Williamsburg, VA, Apr. 1988, AIAA-1988-2212.

[67] Zerweckh, S. H., von Flotow, A. H., and Murray, J. E., "Flight Testing a Highly Flexible Aircraft: Case Study on the MIT Light Eagle," *Journal of Aircraft*, Vol. 27, No. 4, Apr. 1990, pp. 342 – 349.

[68] van Schoor, M. C. and von Flotow, A. H., "Aeroelastic Characteristics of a Highly Flexible Aircraft," *Journal of Aircraft*, Vol. 27, No. 10, Oct. 1990, pp. 901 – 908.

[69] Patil, M. J., Hodges, D. H., and Cesnik, C. E. S., "Nonlinear Aeroelasticity and Flight Dynamics of High-Altitude Long-Endurance Aircraft," *Journal of Aircraft*, Vol. 38, No. 1, Jan. – Feb. 2001, pp. 88 – 94.

[70] Patil, M. J., Hodges, D. H., and Cesnik, C. E. S., "Limit Cycle Oscillations of a Complete Aircraft," *Proceedings of the 41th AIAA/ASME/ASCE/AHS/ASC Structures, Structural Dynamics, and Materials Conference*, Atlanta, GA, April 2000, AIAA-2000-1395.

[71] Su, W. and Cesnik, C. E. S., "Dynamic Response of Highly Flexible Flying Wings," *Proceedings of the 47th AIAA/ASME/ASCE/AHS/ASC Structures, Structural Dynamics, and Materials Conference*, Newport, RI, May 2006, AIAA-2006-1636.

[72] Chang, C.-S., Hodges, D. H., and Patil, M. J., "Aeroelastic Characteristics of a Highly Flexible Aircraft," *Journal of Aircraft*, Vol. 45, No. 2, Mar. - Apr. 2008, pp. 538 – 545.

[73] Shearer, C. M. and Cesnik, C. E. S., "Nonlinear Flight Dynamics of Very Flexible Aircraft," *Journal of Aircraft*, Vol. 44, No. 5, Sep. – Oct. 2007, pp. 1528 – 1545.

[74] Shearer, C. M. and Cesnik, C. E. S., "Trajectory Control for Very Flexible Aircraft," *Journal of Guidance, Control and Dynamics*, Vol. 31, No. 2, Mar. – Apr. 2008, pp. 340 – 357.

[75] Love, M. H., Zink, P. S., Wieselmann, P. A., and Youngren, H., "Body Freedom Flutter of High Aspect Ratio Flying Wings," *Proceedings of the 46th*

AIAA/ASME/ASCE/AHS/ASC Structures, Structural Dynamics, and Materials Conference, Austin, TX, April 2005, AIAA-2005-1947.

[76] Tuzcu, I., Marzocca, P., Cestino, E., Romeo, G., and Frulla, G., "Stability and Control of a High-Altitude, Long-Endurance UAV," *Journal of Guidance, Control, and Dynamics*, Vol. 30, No. 3, May – June 2007, pp. 713 – 721.

[77] Hodges, D. H., "A Mixed Variational Formulation Based on Exact Intrinsic Eequations for Dynamics of Moving Beams," *Int. Journal of Solids and Structures*, Vol. 26, No. 11, Nov. 1990, pp. 1253 – 1273.

[78] Hodges, D. H., "Geometrically Exact, Intrinsic Theory for Dynamics of Curved and Twisted Anisotropic Beams," *AIAA Journal*, Vol. 41, No. 6, June 2003, pp. 1131 – 1137.

[79] Peters, D. A. and Johnson, M. J., "Finite-State Airloads for Deformable Airfoils on Fixed and Rotating Wings," *Proceedings of the Winter Annual Meeting, Symposium on Aeroelasiticity and Fluid/Structure Interaction*, Fairfield, NJ, 1994, American Socity of Mechanical Engineers.

[80] Peters, D. A., Karunamoorthy, S., and Cao, W.-M., "Finite State Induced Flow Models, Part I: Two-Dimensional Thin Airfoil," *Journal of Aircraft*, Vol. 32, No. 2, Mar. – Apr. 1995, pp. 313 – 322.

[81] Meirovitch, L., *Fundamentals of Vibrations*, McGraw Hill, 2001, p. 385.

[82] Wolowicz, C. H., Bowman Jr., J. S., and Gilbert, W. P., "Similitude Requirements and Scaling Relationships as Applied to Model Testing," Tech. Rep. Technical Paper 1435, NASA, 1979.

[83] Park, S., Deyst, J., and How, J. P., "Performance and Lyapunov Stability of a Nonlinear Path-Following Guidance Method," *Journal of Guidance, Control and Dynamics*, Vol. 30, No. 6, Nov. – Dec. 2007, pp. 1718 – 1728.

[84] Bugajski, D. J. and Enns, D. F., "Nonlinear Control Law with Application to High Angle-of-Attack Flight," *Journal of Guidance, Control and Dynamics*, Vol. 15, No. 3, May – Jun. 1992, pp. 761 – 767.

[85] Snell, S. A., Enns, D. F., and Garrard Jr., W. L., "Nonlinear Inversion Flight Control for a Supermaneuverable Aircraft," *Journal of Guidance, Control and Dynamics*, Vol. 15, No. 4, July – Aug. 1992, pp. 976 – 984.

[86] Enns, D. F., Bugajski, D. J., Hendrick, R., and Stein, G., "Dynamic inversion: an evolving methodology for flight control design," *International Journal of Control*, Vol. 59, No. 1, Jan 1994, pp. 71 – 91.

[87] Stevens, B. L. and Lewis, F. L., *Aircraft Control and Simulation*, John Wiley & Sons, New Jersey, 2nd ed., 2003.

[88] Ito, D., Georgie, J., Valasek, J., and Ward, D. T., "Reentry Vehicle Flight Controls Design Guidelines: Dynamic Inversion," NASA TP 2002-210771, Texas A&M University, 2002.

[89] Cotting, M. C. and Cox, T. M., "A Generic Guidance and Control Structure for Six-Degree-of-Freedom Conceptual Aircraft Design," *Proceedings of the 43rd AIAA Aerospace Sciences Meeting and Exhibit*, Reno, NV, January 2005, AIAA-2005-0032.

[90] Goland, M., "The Flutter of a Uniform Cantilever Wing," *Journal of Applied Mechanics*, Vol. 12, No. 4, 1945, pp. A197–A208.

[91] Goland, M. and Luke, Y., "The Flutter of a Uniform Cantilever Wing with Tip Weights," *Journal of Applied Mechanics*, Vol. 15, No. 1, 1948, pp. 13–20.

[92] Anderson Jr., J. D., *Aircraft Performance and Design*, McGraw Hill, 1999, p. 265.